

Improvements for IceCube Event Reconstruction through Geometry Calibration and Photon Timing Distributions

Matti Jansson



Improvements for IceCube Event Reconstruction through Geometry Calibration and Photon Timing Distributions

Matti Jansson

Academic dissertation for the Degree of Doctor of Philosophy in Physics at Stockholm University to be publicly defended on Wednesday 27 March 2024 at 13.00 in Sal FB55, AlbaNova universitetscentrum, Roslagstullsbacken 21.

Abstract

The origin of high-energy cosmic rays is an unsolved mystery because cosmic rays do not travel in a straight line but are bent by magnetic fields due to their electric charge. High energy neutrinos are predicted to be created close to these origins, and are an unambiguous probe, while gamma rays could be obscured or created by other processes. The IceCube Neutrino Observatory at the South Pole has instrumented one cubic kilometre of ice to a depth of 2.4 km by deploying digital optical modules (DOMs) in 86 drill holes. As neutrinos interact in the ice, they create secondary particles which generate Cherenkov light. The light is detected by DOMs and given the timing and the location of the DOMs the event can be reconstructed and the direction of the neutrino's origin can be determined.

So far, IceCube has used the original location of the drill towers for the positions of DOMs in the horizontal plane. Previous attempts to determine the x-y coordinates of the DOMs, relying on data from the drill head or in-situ calibration, could not improve on these generic position estimates or reduce their estimated uncertainty below a few metres. This thesis presents a new method for calibrating the positions of the DOMs. A large sample of muon tracks is used as a calibration light source throughout the detector volume, and a maximum likelihood-based approach is used to determine the positions of DOMs. The method has been applied to 18 central strings, and found statistically significant shifts of the order of 1-2 m from nominal positions for four strings. The results led to, and have been corroborated by, a new study using LED flashers, which has also found deviations in other parts of the detector. There are also indications that calibration of individual DOM positions are possible.

Modelling how light propagates in the ice is of fundamental importance and over the last decade the knowledge of the ice has progressed and in particular the knowledge on how the birefringent properties of ice impact scattering of light. So in an effort to both improve sensitivity of the geometry calibration above and improve event reconstruction, this thesis also presents work done to better incorporate current knowledge of the glacial ice optical properties when reconstructing muon tracks. There is some evidence that this has resulted in a better description of the light distribution in the detector.

Keywords: *Large detector systems for particle and astroparticle physics, Neutrino detectors, Splines, Maximum likelihood.*

Stockholm 2024
<http://urn.kb.se/resolve?urn=urn:nbn:se:su:diva-226450>

ISBN 978-91-8014-673-9
ISBN 978-91-8014-674-6



Stockholm
University

Department of Physics

Stockholm University, 106 91 Stockholm

IMPROVEMENTS FOR ICECUBE EVENT RECONSTRUCTION
THROUGH GEOMETRY CALIBRATION AND PHOTON TIMING
DISTRIBUTIONS

Matti Jansson

Improvements for IceCube Event Reconstruction through Geometry Calibration and Photon Timing Distributions

Matti Jansson

©Matti Jansson, Stockholm University 2024

ISBN print 978-91-8014-673-9

ISBN PDF 978-91-8014-674-6

Printed in Sweden by Universitetsservice US-AB, Stockholm 2024

This thesis is dedicated
to my wife Linda Tissue,
for her never ending
support.

Abstract

The origin of high-energy cosmic rays is an unsolved mystery because cosmic rays do not travel in a straight line but are bent by magnetic fields due to their electric charge. High energy neutrinos are predicted to be created close to these origins, and are an unambiguous probe, while gamma rays could be obscured or created by other processes. The IceCube Neutrino Observatory at the South Pole has instrumented one cubic kilometre of ice to a depth of 2.4 km by deploying digital optical modules (DOMs) in 86 drill holes. As neutrinos interact in the ice, they create secondary particles which generate Cherenkov light. The light is detected by DOMs and given the timing and the location of the DOMs the event can be reconstructed and the direction of the neutrino's origin can be determined.

So far, IceCube has used the original location of the drill towers for the positions of DOMs in the horizontal plane. Previous attempts to determine the x-y coordinates of the DOMs, relying on data from the drill head or in-situ calibration, could not improve on these generic position estimates or reduce their estimated uncertainty below a few metres. This thesis presents a new method for calibrating the positions of the DOMs. A large sample of muon tracks is used as a calibration light source throughout the detector volume, and a maximum likelihood-based approach is used to determine the positions of DOMs. The method has been applied to 18 central strings, and found statistically significant shifts of the order of 1 – 2 m from nominal positions for four strings. The results led to, and have been corroborated by, a new study using LED flashers, which has also found deviations in other parts of the detector. There are also indications that calibration of individual DOM positions are possible.

Modelling how light propagates in the ice is of fundamental importance and over the last decade the knowledge of the ice has progressed and in particular the knowledge on how the birefringent properties of ice impact scattering of light. So in an effort to both improve sensitivity of the geometry calibration above and improve event reconstruction, this thesis also presents work done to better incorporate current knowledge of the glacial ice optical properties when reconstructing muon tracks. There is some evidence that this has resulted in a better description of the light distribution in the detector.

Sammanfattning

Ursprunget till den kosmiska strålningen med hög energi är ett olöst mysterium inom fysiken eftersom kosmiska strålar inte färdas rakt utan blir böjda i magnetfält på grund av sin elektriska laddning. Men om en del av de kosmiska strålarna har en interaktion nära sin källa så kommer neutriner skapas, vilka färdas rakt och har liten sannolikhet att bli påverkade i rymden, vilket gör att deras ursprung kan identifieras. The IceCube Neutrino Observatory är en neutrinodetektor där en kubikkilometer is har instrumenterats på sydpolen. I 86 borrhål har man sänkt ner 5160 ljuskänsliga moduler till ett djup av 1500 till 2500 meter. Dessa moduler ser ljus från sekundärpartiklar som skapas när neutrinerna krockar med atomkärnor i isen.

I mitt arbete som doktorand har mitt fokus legat på att förbättra IceCube långsiktigt genom att minska eller bättra uppskatta systematiska fel. Först undersökte jag möjligheten att kalibrera den horisontella geometrin, som tills nu har använt borrhålets positioner. Idén är att använda vår rekonstruktion baklänges och utifrån muonspår hitta den mest troliga positionen av moduler givet fördelningen av ljus som vi ser. I simulerad data ger det en precision på 0.2 meter. Metoden verkar pålitlig i de centrala delarna av detektorn och har nu bekräftats av en ny metod.

Efter det övergick arbetet till att förbättra beskrivningen av ljusfördelningen från muonspår. Ljusfördelningen uppskattas med hjälp av B-splines, som har anpassats till simuleringar. En viktig anledning till att nya interpoleringstabeller behövs är att modelleringen av isen nu innehåller dubbelbrytning vilket orsakar att ljusspridningen skiljer sig åt i olika riktningar. Detta är den största förändringen av hur ljusspridningen beskrivs på över tio år.

Author's contribution

This thesis describes my work as a graduate student at the Stockholm University Department of Physics (Fysikum). It includes work which was presented in my licentiate thesis, where I developed a method of geometry calibration using muon tracks and the expected distribution of photons to make a maximum likelihood estimate of module locations. These methods and results are presented together with the corroborating results from Martin Rongen, and a possible future calibration method from Saskia Philippen in ICRC2023 proceeding POS 988 [1]. In this thesis Part I and II are mostly from the licentiate with small corrections, edits, and updates. Chapters 7, 8, 9 and sections 10.1, 10.2, 10.3, 13.1, 13.3 and 13.4 are also from the licentiate with minor edits.

Following the work on my licentiate I have worked to introduce recent understanding of ice properties into reconstruction of muon tracks. This work included updating the simulation to create photon distribution tables for different azimuths, running simulation, fitting spline coefficients, implementing a new spline interpolation method for spherical coordinates, coordinate transformations for more efficient interpolation, and evaluations.

In addition to my thesis work on improving calibration and event reconstruction, during my time as a PhD student I also contributed to IceCube in other ways. I am code responsible for the photomultiplier tube (PMT) simulation. I did not do the original implementation, but I have restructured and made it work for the IceCube Upgrade. I have also been code reviewer for when more details of the PMTs in the IceCube Upgrade are added. The IceCube Upgrade is a project where seven new strings are installed in the centre of IceCube with new kinds of modules.

I am also code responsible for DOM launcher. DOM launcher is a part of the simulation chain. This module together with the PMT simulator simulates most internal processes of the DOM. These include distribution of charge from capturing a photon, PMT jitter, late and early pulses, noise, time uncertainty, whether the analogue transient waveform digitizer ATWD is busy, discriminator, communication with nearby DOMs and more.

I have done three monitoring shifts. Each consists of a week of monitoring the data taken in IceCube. This is to make sure data having technical problems do not enter analysis, and gives students an understanding of the raw data and the operations of the detector.

Contents

Abstract	i
Sammanfattning	iii
Author's contribution	v
Abbreviations	xi
Acknowledgements	xiii
1 Overview	15
I Cosmic Rays, Neutrinos, and Neutrino Telescopes	17
2 Cosmic Rays	19
2.1 Known Properties of Cosmic Rays	19
2.2 Origins of Cosmic Rays	19
3 Neutrino Telescopes and IceCube	23
3.1 The Neutrino and the Standard Model of Particle Physics . . .	23
3.2 Neutrino astrophysics	24
3.2.1 Signature	25
3.2.2 Background	25
3.3 The IceCube Neutrino Observatory	26
3.4 Notable Science Results in IceCube	27
II IceCube	29
4 Instrumentation and Data Acquisition	31
4.1 Digital Optical Modules	31
4.1.1 Coordinate System	32

4.1.2	Mainboard	32
4.1.3	ATWD	33
4.1.4	fADC	33
4.1.5	LED	33
4.1.6	Electronic Pulser	33
4.2	Coincidences and Triggers	33
4.3	Filters	35
5	Calibration	37
5.1	Ice Modelling	37
5.2	DOMCal	38
5.3	Waveform Calibration	39
5.4	RAPCal	41
5.5	DOM Optical Efficiency	42
6	Angular Reconstruction	43
6.1	Linefit Reconstruction	43
6.2	Pandel function	44
6.3	SPE Reconstruction	45
6.4	MPE Reconstruction	45
6.5	Ice Model and Spline Tables	45
III	Geometry Calibration	47
7	Motivation and Previous Work	49
7.1	Drill Data	49
7.2	Reconstruction Sensitivity	53
7.3	Previous Work	54
7.3.1	z calibration	54
7.3.2	x and y calibration using flasher data	54
7.3.3	x , y and z calibration using Muons in AMANDA . . .	54
8	Method	57
8.1	Using Likelihood to Determine Positions	57
8.1.1	Individual strings	57
8.2	Single Event Examples	58
8.3	Sum of Many Log Likelihoods	58
8.4	Error Estimation	58

9	Simulation Studies	65
9.1	Simulation in IceCube	65
9.2	Weighting	66
9.3	Selection	66
9.3.1	Downsampling	66
9.4	Estimating x and y	67
9.4.1	Performance in different parts of the detector	70
9.5	Estimating z	72
10	Results	75
10.1	Estimating z	75
10.2	Estimating x and y	78
10.3	Stability of solution	78
10.4	Comparison with drill data	81
10.5	Method for Geometry Calibration using LED Flashers	85
10.6	Comparison of Flasher and Muon Geometry Calibration Results	85
IV	Anisotropy Modelling	95
11	Photon Propagation in Ice: Anisotropy and Birefringence	97
11.1	Birefringence	97
11.2	Anisotropy in IceCube	97
11.3	Birefringence in IceCube	98
11.4	Modelling of Birefringence	99
12	Splines in IceCube	103
12.1	B-splines	103
12.2	B-splines in IceCube	104
12.3	Bivariate Splines and D1RC splines	105
12.4	Mathematical Definition of D1RC Splines	107
12.4.1	Barycentric Coordinates	107
12.4.2	Simplex Spline	107
12.4.3	D1RC Splines	108
12.5	Coordinate System	108
12.6	Building the D1RC Spline	109
12.7	Results and Comparison	110
13	Summary and Future Work	115
13.1	Systematic Errors in Position Calibration	115
13.2	Statistics	116
13.3	Regularization	116

13.4	Dust Layer Effects	116
13.5	Individual DOM calibration	117
13.6	Optimizing time knots	117
13.7	Integration of new splines	117
13.8	Study the impact	117
13.9	Beyond Splines	117
A More plots on comparison between geometry calibration methods		119
References		cxxvii

Abbreviations

ATWD	Analog Transient Waveform Digitizer
BSM	Beyond the Standard Model
D1RC	Directed One Ring Cycle
DOM	Digital Optical Module
DOR	DOM Readout
fADC	Fast Analog Digital Converter
HESE	High Energy Starting Events
HLC	Hard Local Coincident
LED	Light Emitting Diode
MPE	Multi Photo Electron
PE	Photo Electron
PMT	Photo Multiplier Tube
RAPCal	Reciprocal Active Pulsing Calibration
SLC	Soft Local Coincident
SLOP	Slow Particle Trigger
SMT	Simple Multiplicity Trigger
SPE	Single Photo Electron

Acknowledgements

First, I would like to acknowledge the IceCube Collaboration. The physical experiment as well as the amazing people who work on and around it. Without which my work would not have been possible. I thank you for the welcoming atmosphere and enabling a great five years. I also want to thank the IT people in Madison, where I have used 600000 hours of CPU time and was given priority on the cluster towards the end of my thesis.

I would like to thank my supervisors Klas Hultqvist and Chad Finley, who have shown great patience listening to my wild ideas and guided me on this journey.

Furthermore, I would like to acknowledge Tian Lu and Martin Rongen, whom I have worked close with and have done similar parallel work which I have learned and taken inspirations from.

I would also like to thank the IceCube group in Uppsala, whom I have enjoyed greatly. Olga and Allan for drilling me during meetings, Erin for excellent moderating on zoom, Nils for chess challenges, Torsten for his support and Jakob for the dream of karaoke.

Most of all I want to thank my colleagues at my department for enriching my last five years and in particular Kunal for our shared adventure in IceCube, Filip and Yosse for exciting chess games, Tom and Ludwig for indulging me in physics discussions, Christophe and Alexandro for our RPG adventures, and Alessandro for just being a really enjoyable person.

1. Overview

The origin of high energy cosmic rays is an unresolved problem in physics [2] as cosmic rays are charged and do not point back at their sources. If cosmic rays have interactions close to the source they are likely to produce high energy neutrinos which do not get bent in magnetic fields and are not likely to have interactions in the intergalactic medium [3]. The IceCube Neutrino Observatory is a neutrino detector instrumenting a cubic kilometre of ice at the South Pole [4]. It contains 5160 DOMs (Digital Optical Modules) in 86 drill holes at depth of 1500m to 2500m [4]. While the z positions of the DOMs have been calibrated to 0.2m precision, the x and y positions have been more difficult to determine. Until now, the horizontal positions have simply been assumed to be the same as the surface locations of the drill towers. [4] [5]. Data from drilling indicates that it is possible for some drill holes to drift up to 5m from the vertical [6]. With the speed of light in ice being 0.25 m/ns, that could introduce an error of up to 20ns for muon tracks in some directions. Studies have shown that if the drill data is correct, our errors are larger than estimated in simulation, which would hurt our sensitivity [7].

In this work, a maximum likelihood method, using the best reconstruction of tracks and hit timings, is applied to 18 central strings. We use data from the Sun and the Moon filter [8] to get a large selection of tracks. These are all down-going, which introduces a bias when fitting the z position and may explain in part why this method has a systematic error when fitting z . In simulated data we find that we recover the DOM position to within 0.2m in the xy -plane while there is a systematic shift of 0.5m in z . In real data we find that although we likely have a larger systematic error in z , we nevertheless fit consistently the known DOM to DOM distances. A data simulation agreement is always of interest as it gives us hints on how we can improve our simulation. In an effort to improve data simulation disagreement, new tables for reconstruction of muon tracks are created, which if successful will improve the sensitivity of this method as well as many other analyses done by IceCube.

Part I gives background without entering IceCube specifics. Chapter two gives a short overview of cosmic rays. Chapter three introduces neutrino astronomy and the IceCube Neutrino Observatory.

Part II gives details of the electronics, calibration, and reconstruction in IceCube. Chapter four describes the DOM. Chapter five describes the current

calibration of the DOM. Chapter six describes the reconstruction of tracks.

Part III contains the work I did during the licentiate. Chapter seven contains the original motivation and an overview of previous attempts. Chapter eight presents the method used. Chapter nine shows results from simulation studies. Chapter ten contains the final results from the licentiate, new results from the continuation of this work and a comparison with a new geometry study conducted by a colleague.

Part IV is a deeper dive into the anisotropy of the ice and how it is modelled. Chapter eleven describes how birefringence is responsible for the anisotropy and how it is modelled in IceCube simulation. Chapter 12 contains a study into a variant of bivariate splines, called D1RC splines, that had some promise to better model the anisotropy. The chapter also presents the results of the new B-splines that are built from simulation in the birefringent ice. Finally, chapter 13 hosts discussions and possible future improvements.

Part I

Cosmic Rays, Neutrinos, and Neutrino Telescopes

2. Cosmic Rays

Following the discovery of radioactivity and radioactive materials in soil and stone, it was expected that radiation should fall off at higher altitudes. To test this theory, in 1912 Victor Hess ascended in a balloon to measure ionising radiation at different altitudes. He found that radiation increased at altitudes above 1.5 km [9]. This was the first evidence of cosmic rays. It was later realized that these particles came with energies that far exceeded any previously known processes [10]. Since then, numerous experiments have been conducted to study the high energy universe [11] [12]. Our sky has been studied using both observatories and satellites [13][14], which study cosmic rays [15] [16], x-rays [17] [18] and gamma rays [19] [20]. Lately, neutrino observatories have entered the picture [21]. Understanding the origin and mechanisms behind high energy cosmic rays is one of the main reasons to do neutrino astronomy [22].

2.1 Known Properties of Cosmic Rays

While cosmic rays span many orders of magnitude in energy (see figure 2.1 and 2.2), it is believed that the lowest energy ones originate mostly from the sun [25]. Going up in energy, one arrives at a span of energy that is expected to originate in our galaxy from supernova remnants [26]. Further up in energy, protons have so much energy that they can escape the magnetic field of galaxies and most cosmic rays of such energies are expected to be extra-galactic [27]. At energies above $5 \cdot 10^{19}$ eV protons will produce pions when colliding with the cosmic microwave background(CMB) [28] [29], causing the highest energy cosmic rays to have a relatively short range. This causes the drop-off of cosmic rays at these energies, which can also be seen in figure 2.1.

2.2 Origins of Cosmic Rays

The suggested mechanisms for acceleration of cosmic rays are first and second order Fermi acceleration. Second order Fermi acceleration was first suggested in a paper by Fermi [31] where the main idea is that a charged particle colliding with a moving magnetic field will on average gain energy. A similar mechanism can happen in astrophysical shock waves, which is called first

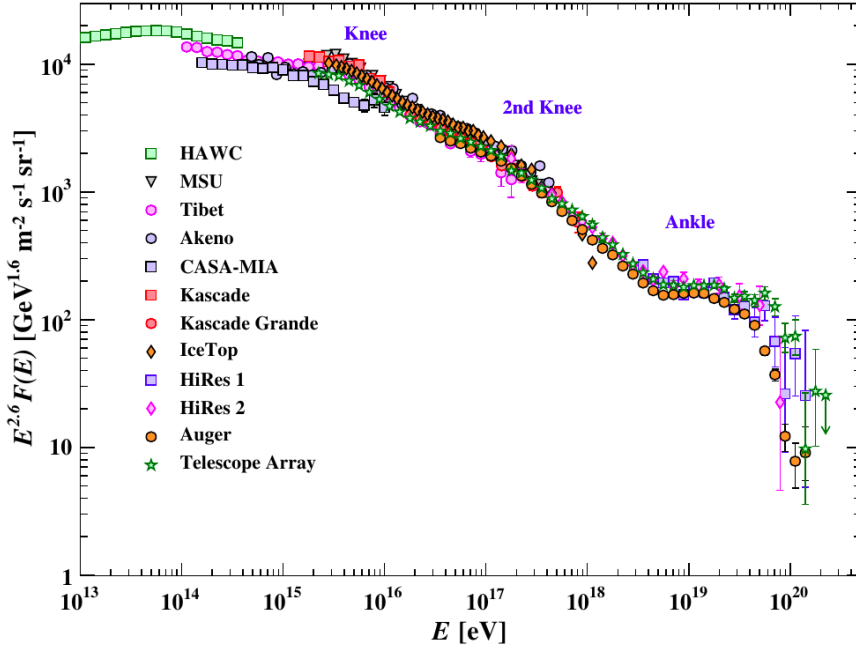


Figure 2.1: Cosmic Ray spectrum as measured by various experiments with one sigma error bars. Taken from [23]. Energy on the x axis and flux times the energy to the power of 2.6 on the y axis. The knees and ankle mark energies where the spectral index changes.

order Fermi acceleration. Particles can increase their energy until they have enough energy to escape the magnetic field that contains them. This gives a maximal energy that can be reached in different sources. In figure 2.3 we have a so-called Hillas plot, and we can see that there are many possible sources for ultra-high energy cosmic rays.

Since the cosmic rays get bent in magnetic fields, the directions they arrive from are almost isotropic [32] [33]. This makes it unfeasible to find the source by studying the cosmic rays themselves. Conversely, neutrinos will travel straight in magnetic fields and are expected to be formed in the same sources which produce cosmic rays. Therefore, if we could find a source of high energy neutrinos, that source would also be producing high energy ions.

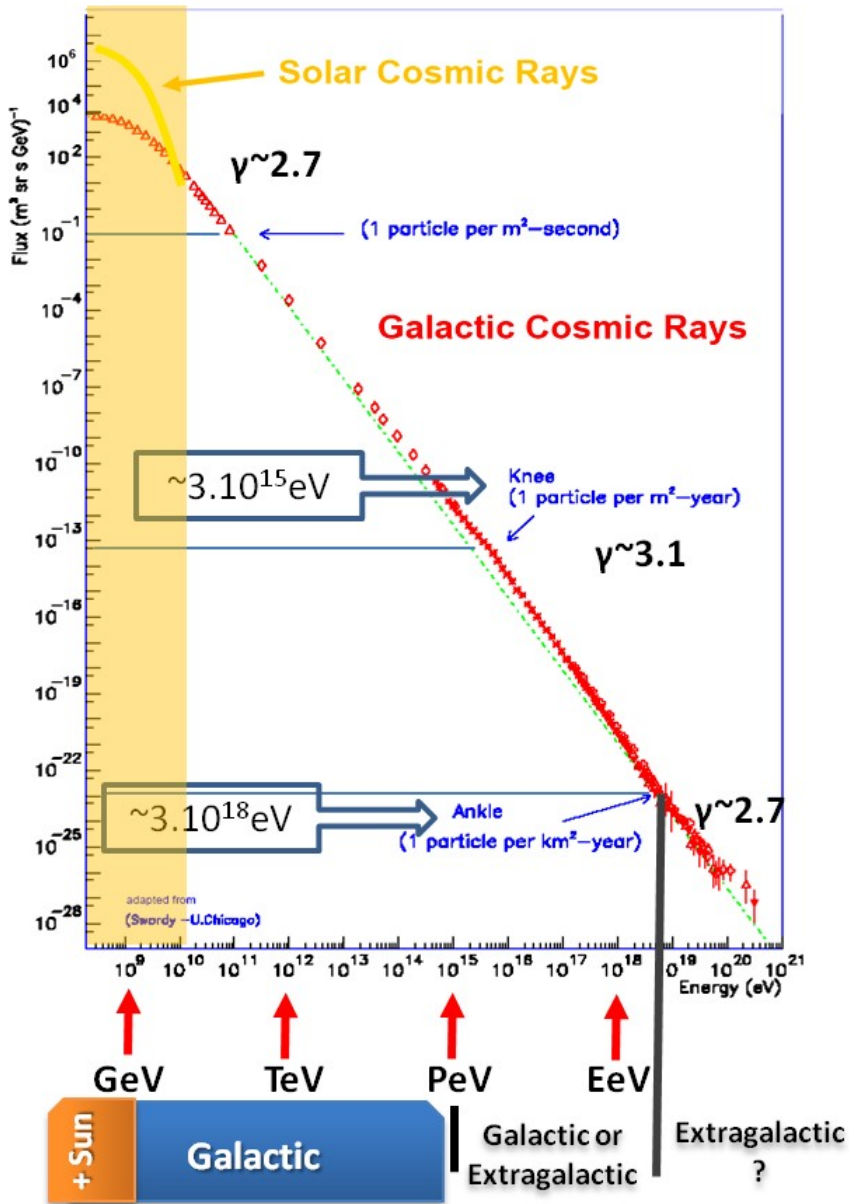


Figure 2.2: The origins of cosmic rays in different energy ranges. Energy on the x -axis and flux on the y -axis. Plot taken from [24]

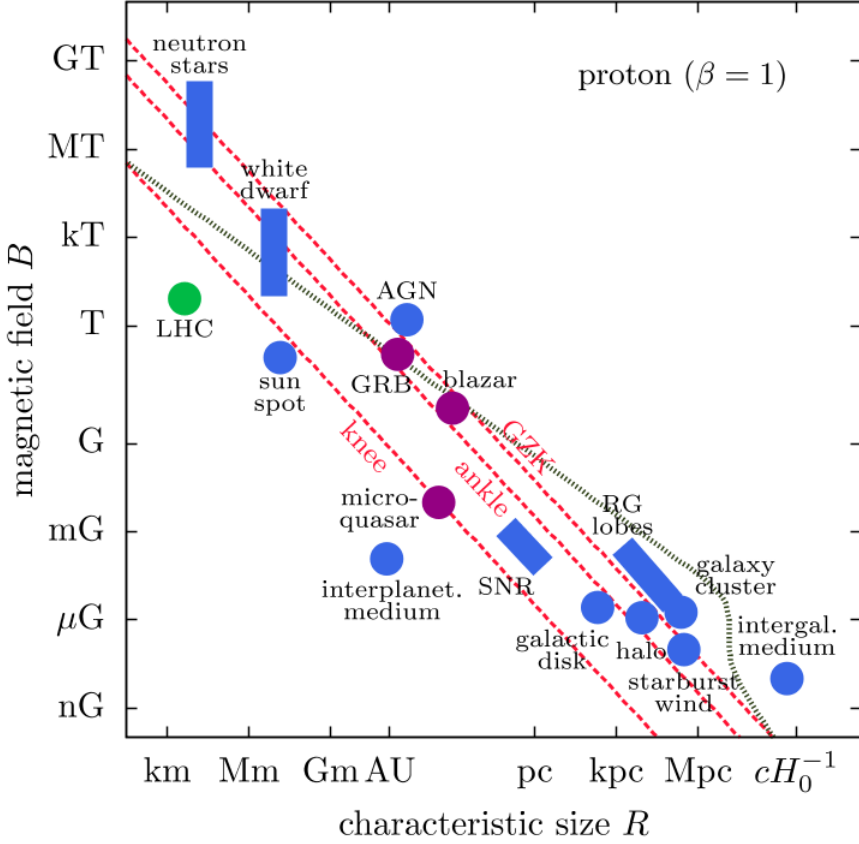


Figure 2.3: Sizes and magnetic field strength of different astrophysical objects. The red dashed lines shows the size and magnetic field strength needed to achieve the energy of different features in the cosmic ray spectrum for protons. The plot is taken from [30].

3. Neutrino Telescopes and IceCube

To study the origin of cosmic rays has been a major driver of development of neutrino observatories for the last 40 years. Among these, IceCube is currently the most sensitive [34]. It is situated at the South Pole, where the clear ice gives excellent conditions to observe Cherenkov radiation [35]. Cherenkov radiation comes from relativistic electrically charged particles travelling faster than light in a medium. This could either be muons from cosmic rays or particles created from a neutrino interacting in the ice.

3.1 The Neutrino and the Standard Model of Particle Physics

Quantum field theory describes particles as excitations of fields. The Standard Model is a quantum field theory containing all known particles and all known interactions, except for gravity [36]. The theory contains three types of fields, fermion fields, gauge fields and one single scalar field. Fermions make up matter because only one particle can occupy a state, so particles in fermion fields take up space. Gauge fields are vector fields that appear with interactions to the fermion when certain invariance requirements are added (gauge symmetries). The scalar field is known as the Higgs field and is needed in the model to allow massive gauge bosons while keeping the gauge symmetry [37] [38]. The Higgs boson was found in 2012 [39] [40].

In the standard model, neutrinos are described by the Lagrangian density \mathcal{L} [23]

$$\mathcal{L} = \bar{\nu} \not{\partial} \nu - \frac{e}{\cos(\theta_W) \sin(\theta_W)} \bar{\nu} \gamma^\mu Z_\mu \frac{1 - \gamma^5}{2} \nu - \frac{e}{\sqrt{2} \sin^2(\theta_W)} \bar{\nu} \gamma^\mu W_\mu^+ \frac{1 - \gamma^5}{2} l - \frac{e}{\sqrt{2} \sin^2(\theta_W)} \bar{l} \gamma^\mu W_\mu^- \frac{1 - \gamma^5}{2} \nu \quad (3.1)$$

where e is the electromagnetic coupling, θ_W is the Weinberg angle, ν is the neutrino field, l is the charged lepton field, Z_μ and W_μ are vector fields. The first term just governs the propagation of neutrinos, the second term governs

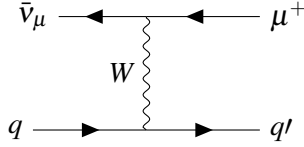


Figure 3.1: Feynman diagram of a charged current interaction giving a track in the detector.

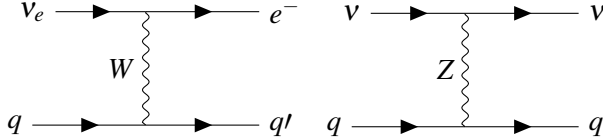


Figure 3.2: Feynman diagrams of a charged current (left) and neutral current (right) interactions giving cascades.

neutral current interactions, and the last two terms govern charged current interactions.

3.2 Neutrino astrophysics

Having a very small mass and no electric charge, neutrinos only interact with the weak force and gravity. Neutrinos are produced mainly in hadronic interactions[41], which produce pions. When charged pions decay, three neutrinos are created. For example, one is produced when a pion decays to a muon, muon antineutrino pair and two more are produced when the muon decays. Pion productions are expected to occur at any source of high energy cosmic rays. This makes the neutrino an interesting probe of the regions of our universe containing the most energetic physics known. While high energy protons and electrons get deflected by magnetic fields and photons have a large chance to get absorbed in interstellar material and radiation fields, the neutrino will travel straight and has a low probability of interacting with interstellar materials. Using the cross-section of $0.7 \cdot 10^{-38} \frac{E}{\text{GeV}} \text{cm}^2$ [23], for a neutrino with energy E , and an average baryon density of $2 \cdot 10^{-7} \text{cm}^{-3}$ [42] we arrive at a mean free path $\lambda \approx 10^{43} \frac{\text{GeV}}{E} \text{m}$. That is 10^8 times the radius of the observable universe. For the energy range of neutrinos observed in IceCube [43] this gives $\lambda \leq 10^{42} \text{m}$.

While the idea of using the deep ocean for a neutrino detector has been around since 1958 [44] it was not until 2013 that an astrophysical flux of neutrinos was first observed, when IceCube reported 28 so-called High Energy Starting Events(HESE)[45][46]. There are currently four detectors for detect-

ing very high energy neutrinos: Astroparticle Research with Cosmics in the Abyss (ARCA) and Oscillation Research with Cosmics in the Abyss (ORCA) in the Mediterranean [47], IceCube in Antarctica [4] and Baikal Gigaton Volume Detector (Baikal-GVD) in Lake Baikal [48]. ARCA, ORCA and Baikal-GVD are still under construction as is the Pacific Ocean Neutrino Experiment (P-ONE) [49] which are about to deploy their first line of modules in 2024 or 2025 [50].

3.2.1 Signature

The signatures of a neutrino will depend on the neutrino type and the interaction it has. The general rule is that muons will travel far losing energy while they are travelling, creating a track in the detector while other particle will lose energy very fast creating many secondaries, called a cascade, giving an almost isotropic ball of light on the scale of detectors that are built for studying astrophysical neutrinos. A neutral current interaction, see figure 3.2, will result in a hadronic cascade and the neutrino will carry some energy away. In a charged current interaction there is a cascade, but in addition the neutrino will turn into a charged lepton with a signature depending on the type. An electron will become part of the cascade, see figure 3.2. A muon, see figure 3.1, will travel a large distance leaving a track of Cherenkov radiation, and a tau will decay soon after creation causing a new cascade that may be hard to distinguish from the first cascade. Muon track directions can have a resolution down to fractions of a degree, while cascades have a directional resolution of several degrees.

3.2.2 Background

The two main backgrounds for observing extraterrestrial neutrinos are neutrinos and muons coming from cosmic rays hitting the atmosphere [51]. Muons from the atmosphere can travel several kilometres through the earth and are best avoided using a coincidence veto with a cosmic ray detector, removing muons originating outside the detector, or observing the sky on the other side of Earth since the atmospheric muons will then be absorbed in the earth. Neutrinos can also be created in the atmosphere by cosmic rays. These are called atmospheric neutrinos. Atmospheric neutrinos come mostly from pion or kaon decay [52], but at higher energy the pions are more likely to have an interaction before they can decay, so atmospheric neutrinos get suppressed at high energies [53].

3.3 The IceCube Neutrino Observatory

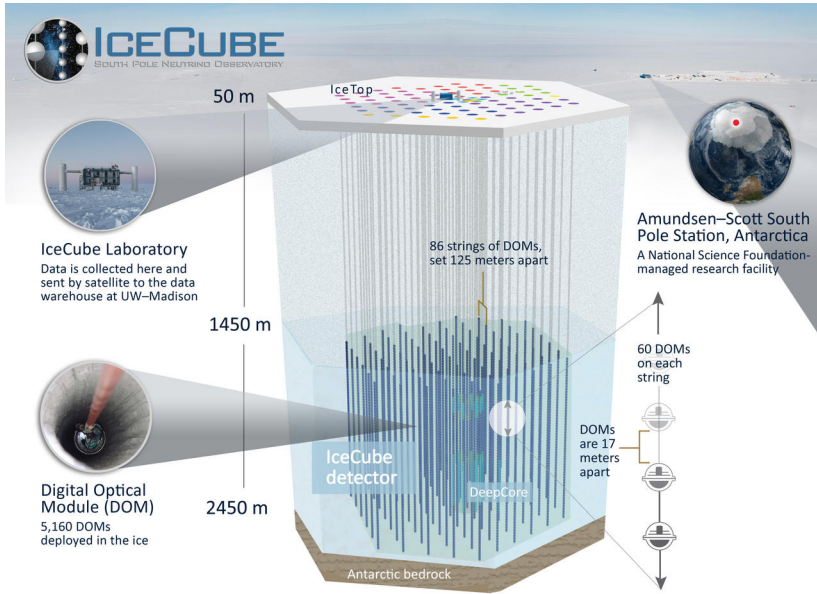


Figure 3.3: The IceCube Neutrino Observatory. Figure taken from reference [54].

The IceCube Neutrino Observatory (see figure 3.3) is a neutrino detector located on the South Pole. The two main components of the detector are IceTop [55] and the in-ice array[4].

The in-ice part spans a volume of 1 cubic kilometre of ice. The volume is instrumented by 86 strings, each carrying 60 DOMs (digital optical module). The ice cap is 2.8 km thick and the instrumented volume is between depths of 1450 m and 2450 m. On strings 1 to 80 the DOMs are evenly spaced, while on strings 81 to 86 the DOMs are more densely spaced in a volume of clearer ice which is located in the bottom third of the range.

IceTop covers an area of one square kilometre on the surface, consisting of 162 water tanks containing two digital optical modules each. The tanks are positioned in pairs above strings 1 to 81.

No previous method has been developed that has been able to calibrate any deviation from the vertical of the drill holes. This thesis aims to investigate the possibility to use the reconstruction of down going-muons to calibrate the deviation of modules from nominal position and in an effort to do that new updated reconstruction tables that model the ice better are created. Both these will ultimately lead to better angular reconstruction and higher sensitivity to

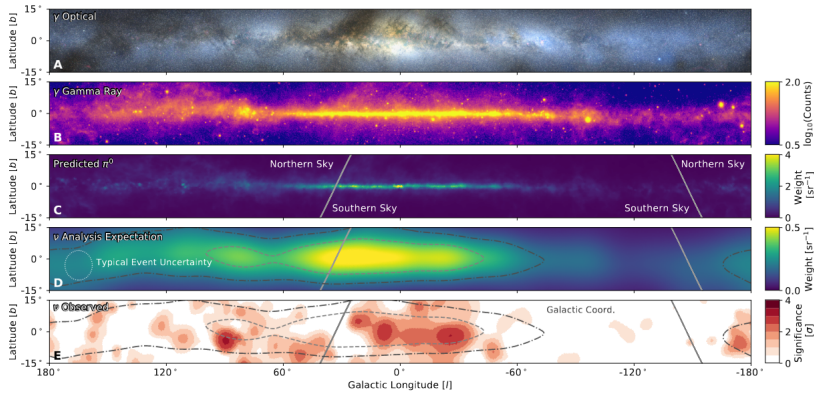


Figure 3.4: The galactic plane in optical(A), gamma ray(B), predicted pion decays from the π^0 model(C), IceCube expectations given π^0 and uncertainty of cascade reconstruction(D) and the local significance of the IceCube analyses. Figure from [56]

neutrino sources. One of the primary research goals of IceCube is to find sources of high energy neutrinos, which in turn should identify the origins of cosmic rays. Therefore, the directional reconstruction is very important.

3.4 Notable Science Results in IceCube

IceCube is the largest neutrino observatory and over the last few years has found evidence for three sources. The first source is the blazar TXS 0506+056 where IceCube saw a high energy neutrino while the blazar was in a flaring state in 2017[57]. An archival search found a flare of neutrinos between September 2014 and March 2015 from the direction of this blazar [58].

In 2022, IceCube found evidence for a steady source of neutrinos in the direction of the active galaxy NGC 1068 [59]. This galaxy has consistently appeared as a hotspot in IceCube’s neutrino sky maps and has now reached a significance of 4.2 sigma. One interesting property is the measured spectral index of 3.2, which is much softer than the measured diffuse astrophysical spectral index of 2.5 [34]. If our directional uncertainty of higher energy events is underestimated, they would contribute less in point source search, which would result in a softer spectral index fit for point sources. As higher energy tracks have smaller uncertainties, any impact by an unknown systematic would impact them more.

In 2023 IceCube reported evidence for diffuse neutrino emission from the galactic plane at 4.5 sigma significance level[56], as shown in Figure 3.4. This

was long considered a guaranteed source of neutrinos, as diffuse gamma-ray emissions are mostly modelled as pion decays produced from cosmic ray interactions in the galactic interstellar medium. Therefore, a neutrino flux from the decay of charged pions was expected in correspondence with the observed gamma ray flux from the decay of neutral pions. While the source is not a surprise, what is unexpected is that IceCube was able to observe it. This was only possible because of improvements in event reconstruction of cascade-type events thanks to great progress in deep learning.

Part II

IceCube

4. Instrumentation and Data Acquisition

There are many types of instruments in IceCube, the digital optical module (DOM), the Sweden Camera, inclinometers, scintillators to name a few. The Sweden camera was used to record the descent of the string and freezing of the ice. Two kinds of inclinometers track any shear in the ice. The DOM looks for light from relativistic particles. Scintillators are used for observing cosmic rays. I will focus on the DOMs here which are related to my work and then describe data acquisition.

4.1 Digital Optical Modules

The most important instrument in IceCube is the digital optical module as the hits recorded by the DOM are the basis for most science done in the collaboration.

A DOM consists of a photomultiplier tube (PMT) and electronics, see figure 4.1, placed in a spherical glass shell. It is connected to the surface through a cable. There are 5160 DOMs in the ice and 320 more in tanks in IceTop. The main functionality of the shell is to protect from the massive pressure of 2.5km of ice, as well as a temporary pressure of up to 700 bar during freezing [4]. The glass shell is made of borosilicate and is transparent to wavelengths longer than 350nm[60].

A PMT is a device for capturing single photons, and release numerous electrons for each such capture event. This is achieved by the photon hitting the cathode releasing an electron through the photoelectric effect. This electron is then accelerated by an electric field and hits a dynode, where the electron causes several electrons to be released, effectively multiplying the charge. This process is then repeated for each dynode, which gives a large multiplication effect. While all electrons released by a photon hitting the cathode are photoelectrons, we also refer to the expected charge from one photon captured by the PMT as one photoelectron (PE).

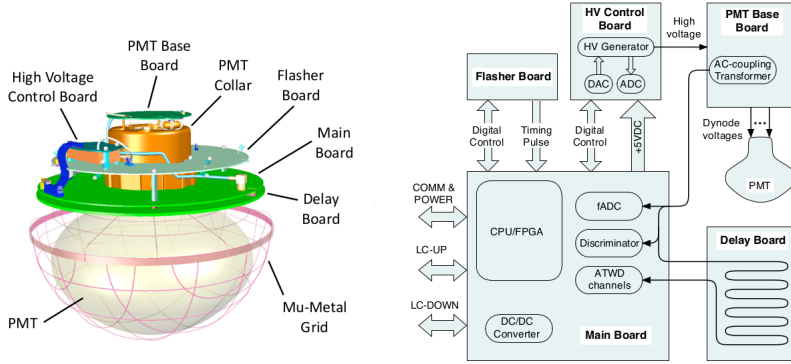


Figure 4.1: Components of the DOM, showing mechanical layout (left) and functional connections (right) (see text for details of the components). Figure taken from [4].

4.1.1 Coordinate System

IceCube has a coordinate system defined internally [61] which we use to describe the geometry of the detector. The axes are defined as follows:

- The y axis is aligned with the Prime Meridian, pointing towards Greenwich, UK.
- The x axis is pointing 90 degrees clock-wise from the y -axis.
- The z axis is normal to the Earth's surface, pointing up, completing a right-handed coordinate system.

The origin is defined such that it is close to the geometric centre of the in-ice array. The origin for z was set to be at the elevation of 2900 ft (0.88 km)[62], which is about at a depth of 2 km. It is fixed to the IceCube array and is moving with the ice at about 10m/year [63].

4.1.2 Mainboard

The mainboard, see figure 4.2, handles power supply, communication and most of the logic needed for the DOM. Here, I describe the parts that are of relevance to the calibration procedure. A more detailed technical description can be found in reference [64].

4.1.3 ATWD

The Analogue Transient Waveform Digitizer (ATWD) is a dedicated circuit to record the waveform from the PMT. The DOM contains two ATWDs to enable it to be active while a waveform from a previous event is being read. Each ATWD has four channels with different amplification. Three channels are used in operation with amplifications of 16, 2 and 0.25. The amplifications have been chosen to cover the dynamic range of the PMT. The fourth channel is used in calibration of the DOM[4]. Each channel has 128 bins and is able to record 427 ns of PMT output, achieving a temporal resolution of 3.33 ns.

4.1.4 fADC

While 427 ns is enough to capture most light that arrives at the PMT from a nearby source, some light from far away or that has scattered can arrive later. To cover a longer time period, a second digitizer is added. The Fast Analogue Digital Converter (fADC) is continuously sampled at a speed of 40 MHz. While the mainboard is able to record arbitrarily long waveforms from it, it is configured to record $6.4\mu\text{s}$ from when a photon is detected.

4.1.5 LED

The mainboard of the DOM is equipped with an LED. The main purpose of this LED is to generate a weak signal such that a single photon is detected by the PMT, which is then used to calibrate the PMT response. The DOM also contains a separate board called flasher board with 12 LEDs that are used for sending light signals to nearby DOMs for calibration.

4.1.6 Electronic Pulser

The mainboard has a circuit that can produce waveforms similar to a PMT pulse. It can produce a pulse up to 40 PE in size in steps of 0.04 PE. It is used to calibrate the size of waveforms. It has been shown that the pulses produced are slightly wider than real PMT pulses.

4.2 Coincidences and Triggers

A Coincidence is when two neighbouring or next to neighbouring DOMs have detected a photon in a short timespan. A trigger is a decision to read and store data. A more complete description can be found in reference [4].

When an in-ice DOM detects a photon, it will send a signal to neighbouring and next to neighbouring DOMs. If any nearby DOM is also hit, the hit is

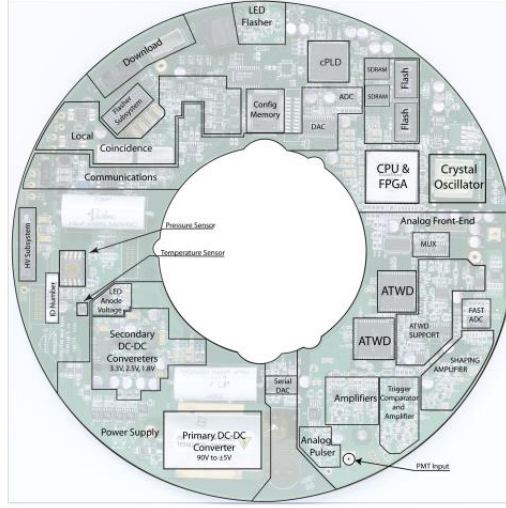


Figure 4.2: Layout of the DOM mainboard. Figure taken from [4].

marked as a local coincidence (HLC), otherwise the hit is marked as soft local coincidence (SLC). The hit is then sent to the DOMHub and stored on disk through an interface called Hitspool. For HLC hits, the entire waveform is sent to the surface from both the fADC and ATWD, while for SLC hits only a peak sample from the fADC is transmitted. Then the hits are checked against the trigger conditions, which initiate recording of data for events. Here I will describe the seven main triggers used through 2023 [65]. Although IceCube is constantly observing data, only a small subset of the data is recorded unless a trigger is passed.

Three of the triggers are Simple Multiplicity Triggers (SMT). SMT is configured to trigger on 8 HLC hits during $5 \mu s$ in in-ice, 3 HLC hits during $2.5 \mu s$ in DeepCore or 6 HLC hits during $5 \mu s$ in IceTop.

There are two Volume Triggers that trigger on 4 HLC hits within a certain volume in both in-ice and IceTop. These require 4 HLC hits in a volume shaped as a cylinder (in-ice $r=175m$, $h=75m$, IceTop $r=60m$, $h=10m$).

Finally, there is the String Trigger that requires five out of seven consecutive DOMs on the same string having a hit, and the Slow Particle trigger (SLOP) which looks for tracks with a speed below $0.5c$. The SLOP trigger is mostly used to search for physics beyond the standard model (BSM) such as

magnetic monopoles.

4.3 Filters

Filters are a set of conditions that are running on the IceCube computer cluster and give a first selection of events to be used in analyses. Here I will describe the filtering in use during 2023.

The triggering records about 1 TB of data a day which is an order of magnitude higher than our available satellite bandwidth of about 100 GB a day. So a first level of event selection is run on the pole by a set of filters. Once a year the collaboration decides on which filters to run in the coming year. As of 2023 there are 32 active filters.

These filters reduce the number of events by 85%, this in itself does not affect data size significantly as events with small amounts of data gets filtered out. The waveforms are also compressed to 9% the size of the original waveforms. The compression introduces an error of 1.1ns in time and 0.04 PE in collected charge[4]. After filtering and compression, 90 GB of data is transferred over satellite each day.

Of particular interest to my analysis is the shadow filter. The shadow filter captures muon tracks in all azimuth and in a moving zenith band tracking a celestial object, turning off if the zenith band goes below the horizon. There are two shadow filters running, one following the sun and one following the moon. The reason for observing the moon is that it blocks the path of cosmic rays, causing a shadow in the cosmic ray sky. From this sink in our data, we can confirm our pointing and measure our angular reconstruction errors [66] The sun is more complicated than the moon, as it has a strong magnetic field bending the path of cosmic rays. But since it has the same angular size as the moon, we can study the solar magnetic field's effect on cosmic rays [67]. It is also used to study the background of searches for BSM physics in the sun. [8] Most muons are not saved on the level that is needed for my analysis, and the shadow filters are the filters that save the most muon tracks, which is why I use them for the geometry calibration.

5. Calibration

Calibration is needed to take any measurements and interpret them as a physical quantity. Just as a ruler needs to have a scale that tells the user the distance between the notches, IceCube needs to extract energy, timing and position from the waveform and internal times recorded in the DOMs. The calibration goal in IceCube is that photon hits can be recorded with a precision of 1ns, and detector positions to be known to 1m.

The following is a summary from the calibration procedures in the IceCube Instrumentation and Online Systems paper [4], unless otherwise stated.

5.1 Ice Modelling

The ice at the detector is a major source of systematic errors. Properties like photon absorption length, photon scattering length, and anisotropy vary across the ice and when the ice refroze in the drill holes a small column of bubbles was created in the middle of the drill hole. This bubble column could be on any side of a DOM dependent on which side of the drill hole the DOM is leaning. Ice is also a birefringent material, which causes light to propagate differently in different directions [68]. A deeper treatment of this anisotropy can be found in chapter 11.

When IceCube was built, it was assumed that the photon propagation in the ice could be described by absorption and scattering, where scattering was introduced by impurities in the ice. The scattering coefficient and absorptivity properties could change with depth, as different years could have different amounts of impurities. Measured scattering and absorption properties can be seen in figure 5.1. The effective scattering length is defined as

$$\lambda_e = \frac{\lambda_s}{1 - \langle \cos \theta \rangle} \quad (5.1)$$

where λ_s is the true scattering length in the ice and θ is the scattering angle [69].

For simulation and indirectly reconstruction, the ice properties are tabulated in 10 metre layers, which are estimated by fitting to flasher data. While

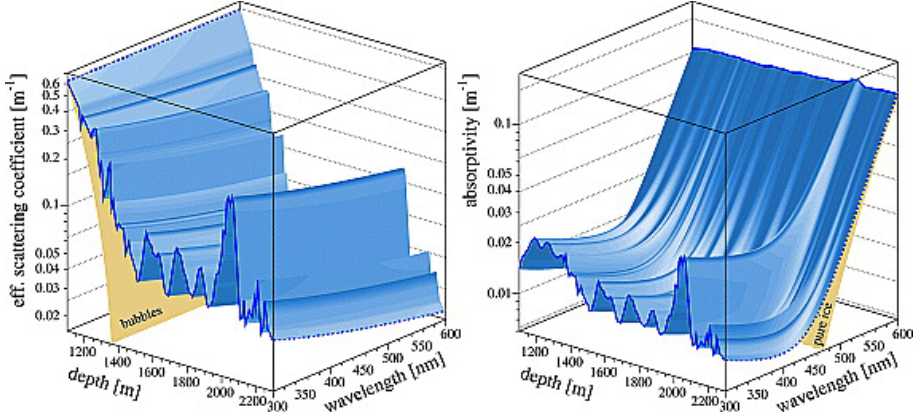


Figure 5.1: Absorption and scattering dependence on depth and wavelength in the deep polar ice. For long wavelengths we can see that the absorption length is limited by the intrinsic properties of ice and for shallow ice the scattering length becomes very small because of air bubbles. A noticeable feature is the dust layer at about 2000 m depth that has significantly higher absorption and scattering than the rest of the deep ice. [69]

it assumed that the ice is created by layers of precipitation and are homogeneous, the layers get bent, so a correction to the flat ice layers are included describing tilt for each of the ice layers. The tilt is not used in reconstruction as it would introduce two more dimensions when estimating the time PDFs of photon distribution. More details on this are given in chapters 6 and 12.

The wavelength dependence is weighted with the Cherenkov spectrum and module acceptance to get values used in reconstruction and simulation.

5.2 DOMCal

DOMCal is a calibration procedure performed within each DOM. This calibration is only done once a year for the in-ice DOMs, as the environment is so stable, while for the IceTop DOMs this calibration is done once a month as temperature changes on the surface need to be accounted for [4].

Using a precision electronic pulser giving known charges, a reference DC bias voltage, an oscillator, and single photoelectrons, the calibration procedure is as follows [64]. The discriminator gets a first calibration using the charge from the electronic pulser [4]. Next, the ATWD voltage is calibrated by recording the waveform for a range of the DC bias voltage. This linear relationship is calibrated for each time sample and gain channel. After that, the gain of the highest gain ATWD channel of both ATWDs are calibrated using the electronic pulser. Using that, a relative calibration is done for the other gains by

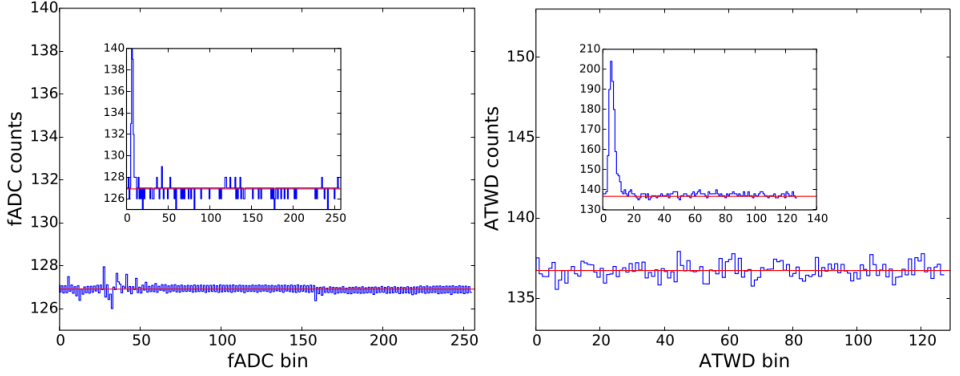


Figure 5.2: The average of about 1000 waveforms for a typical DOM for each of the bins in the fADC and ATWD. The inset figures are for a typical SPE. The pattern in the right plot is the pedestal pattern that is calibrated away. Figure taken from [4].

recording from multiple channels at once. Next, the sampling speed of the ATWD is calibrated using the oscillator and recording the number of cycles for different speed settings. Once the ATWD sampling speed is set the timing difference between ATWD and fADC is measured.

Now, the PMT and delay board transit time is measured using the LED. Using a low yield LED or background photons, the gain on the PMT is tuned to 10^7 . Finally, the calibration of the discriminator can be refined using the calibrated PMT. Once the calibration is done, the DOM will serialize the result to XML and send it to the surface [4].

5.3 Waveform Calibration

The baseline in the waveform digitizers are not stable over the timescale of a year and are calibrated once for each data run, typically lasting 8 hours. The baseline is the mean of the 128 bins in the ATWD and for each bin the deviation from the baseline is measured. This is called the pedestal pattern and is subtracted in the DOM before sending waveforms to the DOMhub, see figure 5.2. The measurement is done by sampling the ATWD 200 times and taking averages. There is a check for light contamination that will redo the procedure if any waveform contains 15 PE or more.

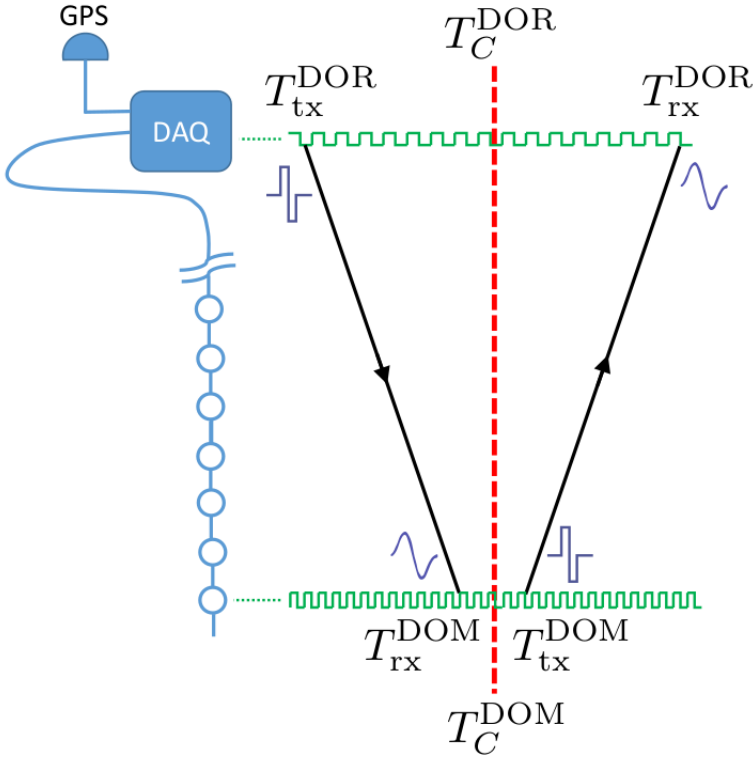


Figure 5.3: Schematics of RAPcal. Two signals transmitted at T_{tx} and recieved at T_{rx} , both in local time. Figure taken from [4].

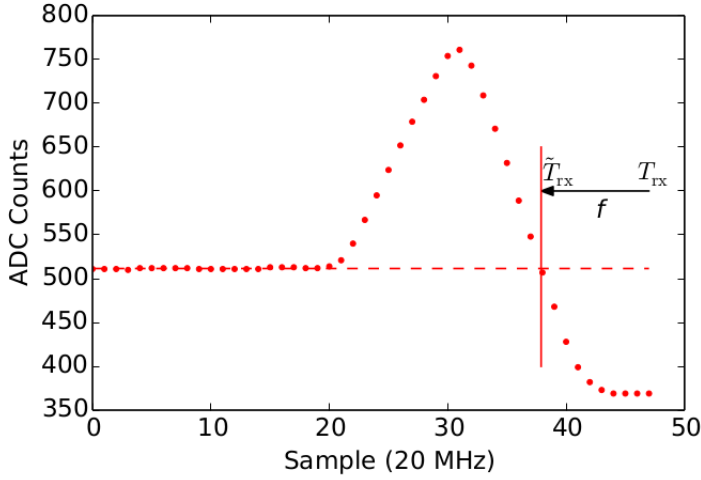


Figure 5.4: Readout of the received signal. The interpolated crossing time is marked with a vertical red line. Figure taken from [4]

5.4 RAPCal

While the calibration of DOMCal changes only once a year, the clock on the DOM can drift a clock cycle in a few minutes. Therefore, a constant recalibration of the clock is required to ensure the accurate conversion from internal DOM time to Coordinated Universal Time (UTC). This recalibration is achieved through Reciprocal Active Pulsing (RAPCal).

RAPCal works by sending a bipolar pulse from the DOM Readout (DOR) Card, which is then returned. The measured received and transmitted times are used to calculate the time offset between the DOR and DOM clocks (see Figure 5.3). Given the symmetry of the system, the mean of the two times in the DOR and DOM will correspond to the same time. To achieve precision below the sampling speed, the time when the signal crosses zero is calculated using interpolation (see Figure 5.4). The clocks internal to the DOMs drift compared to UTC. The median magnitude of this deviation is $\frac{\Delta t}{t} 1.34 \times 10^{-6}$. But this drift is very stable, and running RAPCal every few minutes would be enough to keep the unhandled deviation under 1 ns. But there are also stochastic fluctuations[64], which is why RAPCal runs every second. Confirmations with flashers has shown the time uncertainty to be 1.2 ns.

5.5 DOM Optical Efficiency

The DOM Optical Efficiency is how likely a photon hitting the DOM is to generate a signal in the PMT. While DOMCal and RAPCal are calibrated to a level that it does not impact analyses, DOM efficiency is a significant source of uncertainty for several analyses as it directly impacts energy estimates.

DOM efficiency has been measured in several ways. For 13 [4] or 16 [70] PMTs the absolute efficiency was measured. DOM efficiency has also been measured using Monte Carlo simulations of minimum-ionizing single muons and comparing to data [71]. The measured DOM efficiencies is strongly correlated to ice modelling and need to be recalibrated for each ice model. The optical efficiency measured this way is slightly higher than what was measured in the lab, but the difference is below the systematic error of 15%.

6. Angular Reconstruction

In IceCube we reconstruct flavours, direction of travel, and energies of neutrinos, or muons that are detected. Reconstructions also need to handle noise and coincident events. Here I will focus on angular reconstruction of muon tracks, partly because I use these reconstructions for my analysis, partly because they would be the main consumer of improved geometry calibration and also because they would be impacted by new spline tables. There are also specialized reconstructions for low energy and for cascade events. Lately, there have been developments into reconstruction using neural nets.

When IceCube searches for astrophysical sources of neutrinos, most analyses use an algorithm called splineMPE. As it is very expensive to scan the likelihood space for this algorithm and the minimizer can easily miss the global optimum and be trapped in a local minimum, a hierarchy of reconstructions is used where each step is an improvement on the previous and used as input to the next reconstruction. In my work, I have used the setup also running in IceCube online systems. It starts with a linefit, which seeds a single photo electron (SPE) fit using the Pandel function, see section 6.2, which seeds a second SPE using the Pandel function, which seeds a multi photo electron (MPE) using the Pandel function, which seeds a MPE using spline tables.

6.1 Linefit Reconstruction

Linefit is a least-square linear fit [72], fitting a location \mathbf{r} and a velocity \mathbf{v} to minimize

$$\sum_{i=1}^{N_{hit}} (\mathbf{r}_i - \mathbf{r} - \mathbf{v} \cdot t_i)^2 \quad (6.1)$$

given N_{hit} hits at locations \mathbf{r}_i at times t_i .

To handle noise, coincident events, and late hits, three improvements to the algorithm have been implemented [73]. First, any hits which are 778 ns after any hit within 156 m are considered late hits and not included in the fit. Next a clustering algorithm is run where two hits are considered in the same cluster if $\sqrt{\delta x^2 + \delta y^2 + \delta z^2 + (c\delta t)^2} \leq 450$ m. Then, if clusters produce close lines, they are merged. Lastly, the least square is replaced with a Huber fit [74]. That is, if $|\mathbf{r}_i - \mathbf{r} - \mathbf{v} \cdot t_i| < k$ the loss function is replaced by $2|\mathbf{r}_i - \mathbf{r} - \mathbf{v} \cdot t_i|k - k^2$.

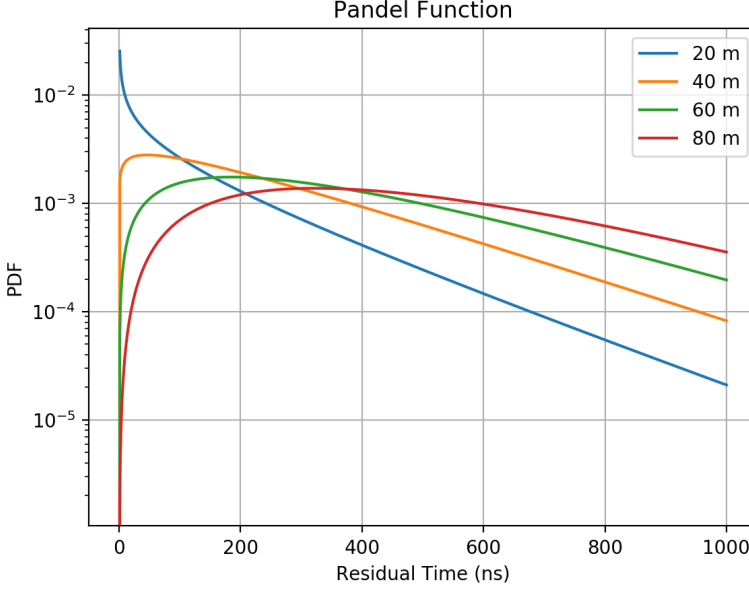


Figure 6.1: Examples of time PDFs from the Pandel function at different distances.

k has been fitted to the value which gives best results in simulation, which is 153m. The Huber fit gives slightly more weight to points that are well-fitted.

6.2 Pandel function

A more advanced algorithm is to create a probability density function (PDF) for photon hits for each DOM given a track hypothesis, and then search for the track hypothesis that gives the maximum likelihood. The first of these probability density functions is the Pandel function. The Pandel function was developed after an analysis of laser light signal in the BAIKAL experiment [72]. It is given by

$$p(t) = \frac{1}{\left(\frac{1}{\tau} + \frac{c_{ice}}{\lambda_a}\right)^{-d/\lambda} \Gamma(d/\lambda)} t^{\frac{d}{\lambda}-1} e^{-t\left(\frac{1}{\tau} + \frac{c_{ice}}{\lambda_a}\right)} \quad (6.2)$$

This is a gamma distribution with shape parameter $k = \frac{d}{\lambda}$ and scale parameter $\theta = \frac{1}{\tau} + \frac{c_{ice}}{\lambda_a}$. λ_a is the absorption length and c_{ice} the speed of light in the ice. τ and λ are free parameters which are fitted to fit data. Examples of PDF shapes for the Antarctic ice can be seen in figure 6.1. The function gives the

probability p for a photon to hit at time t , defined such that $t = 0$ is the earliest possible moment given the speed of light in the ice at a distance d from the track. When evaluating the Pandel function, the absorption from the ice layer around the receiving DOM is used.

6.3 SPE Reconstruction

The Single Photo Electron (SPE) reconstruction make a maximum likelihood estimate of the track using Pandel function for the likelihood. A setting decides whether to use all photons or a subset of photons. For the reconstructions used here, only the first PE hitting a DOM is used.

6.4 MPE Reconstruction

The Multiple Photo Electron (MPE) reconstruction is also a maximum likelihood reconstruction, but uses the PDF of the first arriving photon given a certain number of PEs. If all PE have the same PDF p , the first arrival time of N PE has a PDF p_1 given by

$$p_1(t) = Np(t) \left(\int_t^\infty p(\tau) d\tau \right)^{N-1} \quad (6.3)$$

This tells us that the more light that hits a DOM the more likely the first light has not been scattered. Unscattered photons should constrain the distance to the track better, giving a sharp likelihood and good angular resolution.

6.5 Ice Model and Spline Tables

For a good reconstruction, we need to model the arrival times of photons. More detailed understanding of scattering and absorption are needed for higher quality reconstruction. These properties change with depth. A second order effect is ice layer "tilt" (the variation of the depth of the ice layers across the detector). Our ice model has absorption length and scattering length along the direction of the glacial movement (flow axis) and perpendicular to it in different layers of the ice. The layers also have tilts that are fitted. We fit this model to the timing profile of LED light between different DOMs. For the Pandel function we use the ice properties of the layer with the receiving DOM ignoring the properties of ice the photon has to travel past.

For a more accurate PDF of a photon arrival time at a DOM given a track hypothesis, spline tables are created from simulation. These PDFs together with the MPE reconstruction, are used in most analyses using track data. Chapter 12 contains the work to include anisotropy into the splines.

Part III

Geometry Calibration

7. Motivation and Previous Work

The IceCube time resolution after calibration is approximately 1 ns which corresponds to about 0.25m for light in ice. While it is unclear what our precision on DOM locations are, there are reasons to believe that positions could be off by up to a few metres for some of the DOMs. This could give an effect on our reconstruction quality and this would decrease our sensitivity to point sources in two ways: we are worse at reconstructing the direction, and we underestimate our errors.

7.1 Drill Data

During the deployment of IceCube the drill head recorded the deviation from the vertical below the drill tower. Sadly, the data for half of the strings are missing for various reasons. Also, the accuracy of these measurements has been difficult to verify and the data were never used for calibrating positions. The drill measures the angle of the drill using Earth's magnetic field and the depth using a pressure sensor. Using this, the drill path is reconstructed assuming the drill is travelling straight forward. In the data, there are large differences in measured deviation between different drill holes, with up to 5m deviation for some holes (figure 7.1) while some stay within 0.5m (figure 7.2). In the figures, the path of the drill in the xy -plane is shown. Offsets are defined as the measured position minus the position of the drill tower (nominal position).

The assumption when reconstructing the hole from drill data is that the ice is melted straight in front of the drill head during descent. It is plausible that the ice melts in a slightly different direction than where the drill is pointing. By comparing the position estimates from the drill going down with the estimates from the drill going up we can make an estimate of the absolute error in the drill estimate. Looking at figure 7.3 we can see that at the depth of the detector (2.5km) the estimates deviate 0.8m on average.

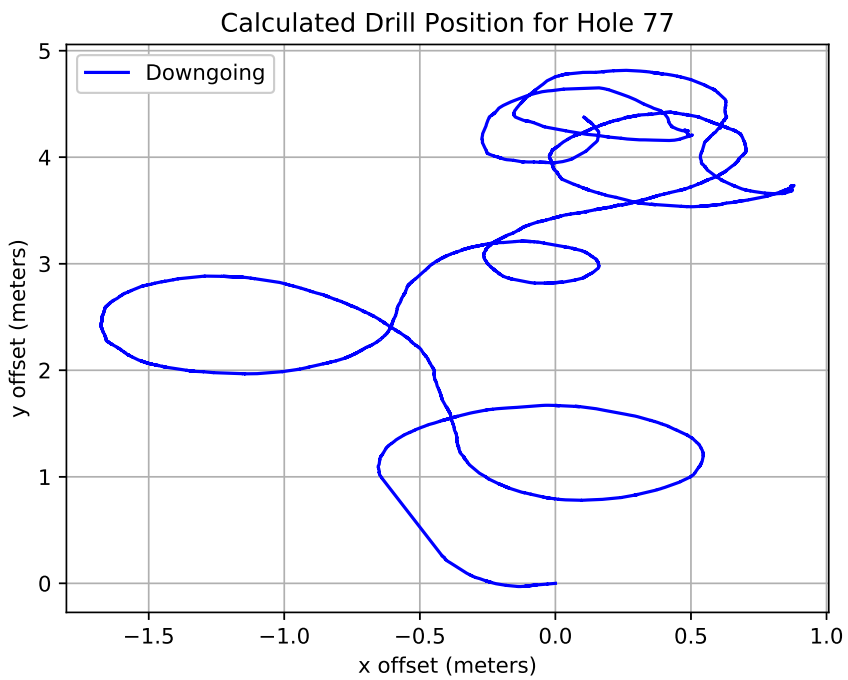


Figure 7.1: The reconstructed path of the drill in the xy -plane. (0m, 0m) is the location of the drill tower.

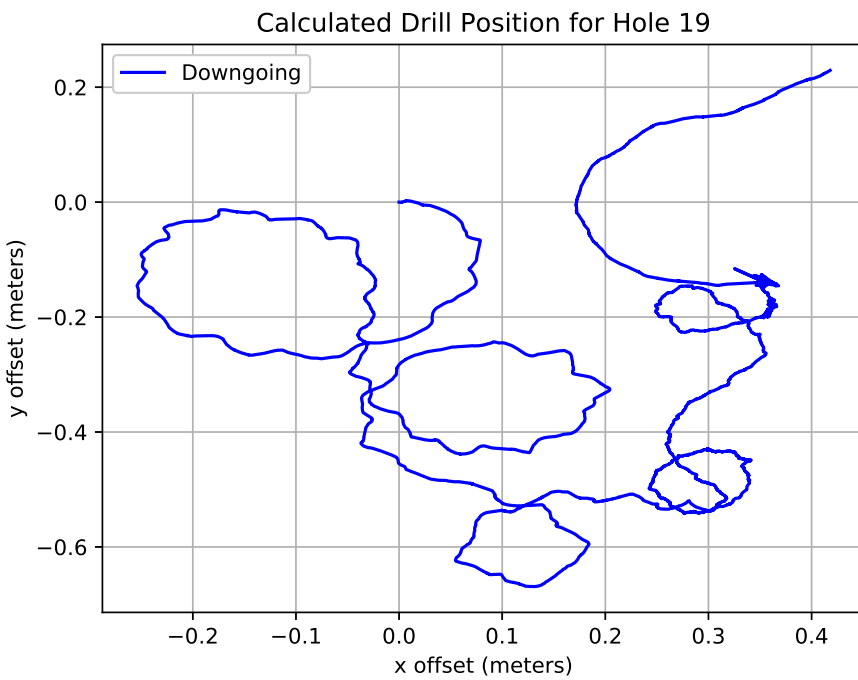


Figure 7.2: The reconstructed path of the drill in the xy -plane. (0m, 0m) is the location of the drill tower.

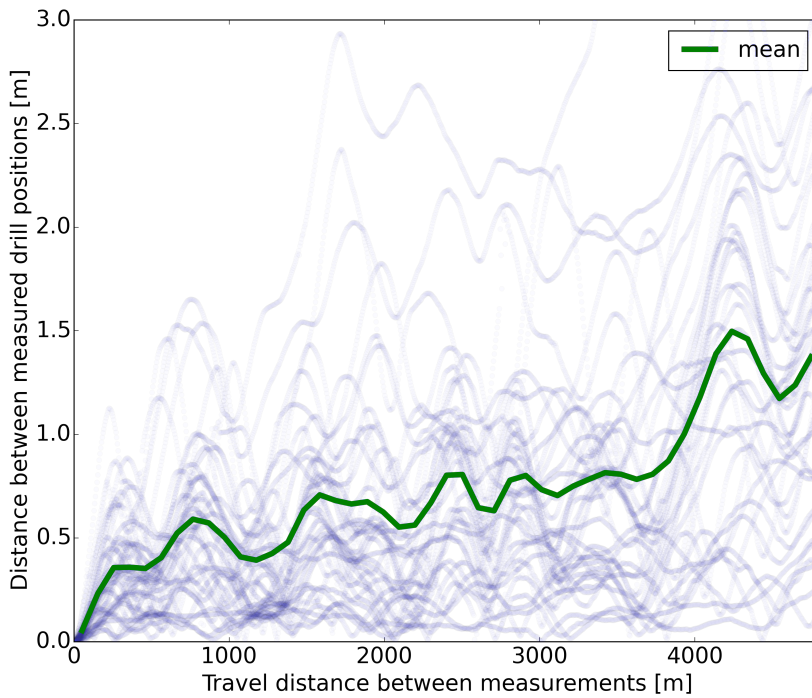


Figure 7.3: The distance between positions measured on the way down to the position measured on the way up. This gives an estimate of reliability of drill position measurement. Figure taken from [75].

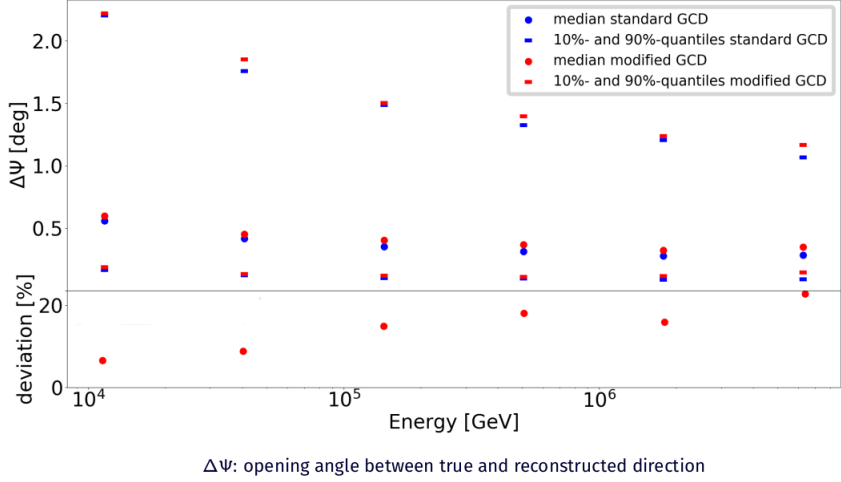


Figure 7.4: The median error with 10% and 90% quantiles of reconstruction errors at different energies. Blue is simulated using nominal positions. Red is simulated using drill data to move around DOMs. Below is a comparison showing how much the error grows. GCD is the format we use to store geometry, calibration, and detector status. Figure taken from [7].

7.2 Reconstruction Sensitivity

In 2019 Lilly Peters did a study [7] investigating how much errors in DOM positions impact reconstruction. In figure 7.4 we see her results assuming the drill data are representative of DOM deviations from nominal. We can see that the errors increase with energy and above 100 TeV where the background is suppressed [76] the angular uncertainty is 15% larger.

7.3 Previous Work

To first order, the DOM positions are directly below the drill tower at a depth given by the pressure sensor at the bottom of the string [4]. There have been several attempts to improve on this measurement, three of which are described here. Currently, only the calibration of the z coordinate is accepted as the confidence in the other results has been too low.

7.3.1 z calibration

z positions have been calibrated [4] using the flasher LEDs that are on all DOMs. As seen in figure 7.5, the distance between two DOMs, $d = \sqrt{D^2 + (z - z_0)^2}$, is a function of the horizontal distance D and the vertical distance $z - z_0$, where z is the coordinate of the receiving DOM and z_0 the emitting DOM. $z - z_0$ can be rewritten as $z' - \Delta z$ where z' is the nominal distance and Δz is the unknown deviation. As DOMs are 17m apart on the string, we have many pairs of DOMs with the nominal distance z' and Δz is constant for a pair of strings. We now have 60 DOM pairs with an offset of 0m, 59 pairs with an offset of 17m and so on, giving us a reasonable statistical strength. By measuring the travel time of photons, we can derive a distance. The distance is not the physical distance, because of delays due to scattering of photons. It was found that adding a free parameter L made $\sqrt{D^2 + (z' - \Delta z)^2} + L$ a good fit to data. As the measured offsets between different pairs of strings are consistent, we have good reason to believe in the z measurements.

7.3.2 x and y calibration using flasher data

In an internal presentation [78] Chris Sheremata and Darren Grant presented a method where they used trilateration with flasher data to try to determine the x and y coordinates. Their method used timing from flashers at 15 DOMs on three nearby strings to determine the x and y positions for a DOM. For each pair of DOM on different strings, there are two intersection in the plane of interest, see figure 7.6. One will be far away from the nominal position and discarded. Then the average of the 75 positions was used as the estimate of the DOM position. An attempt to improve the position estimates by shifting them to align with drill data was also undertaken. This method was applied to 3 deep core strings.

7.3.3 x , y and z calibration using Muons in AMANDA

In AMANDA, Dmitry Chirkin also tried to calibrate the positions of the DOMs using down going muons, see internal presentation [79]. Instead of using tim-

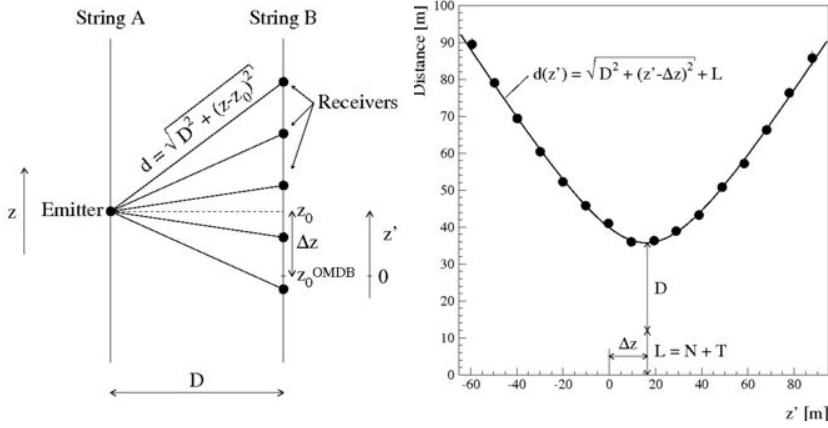


Figure 7.5: The method for extracting relative depth from flasher data. On the left is an overview of a single DOM flashing, and for DOMs on nearby strings the time delay will give a measured distance d . By doing this to all DOMs on a pair of strings, we get the plot on the right where each dot is the measurements of all distances with the nominal vertical distance of z' . The parameters D , Δz and L are fitted for and Δz is the calibrated vertical offset between the two strings. Figure is taken from the internal wiki [77] and N and T are not defined.

ing of the photons (as will be considered in this thesis), only the number of hits was used and this was taken as a measurement of distance to the muon track. This approach was unable to find any significant deviations as it had large systematic errors. [80].

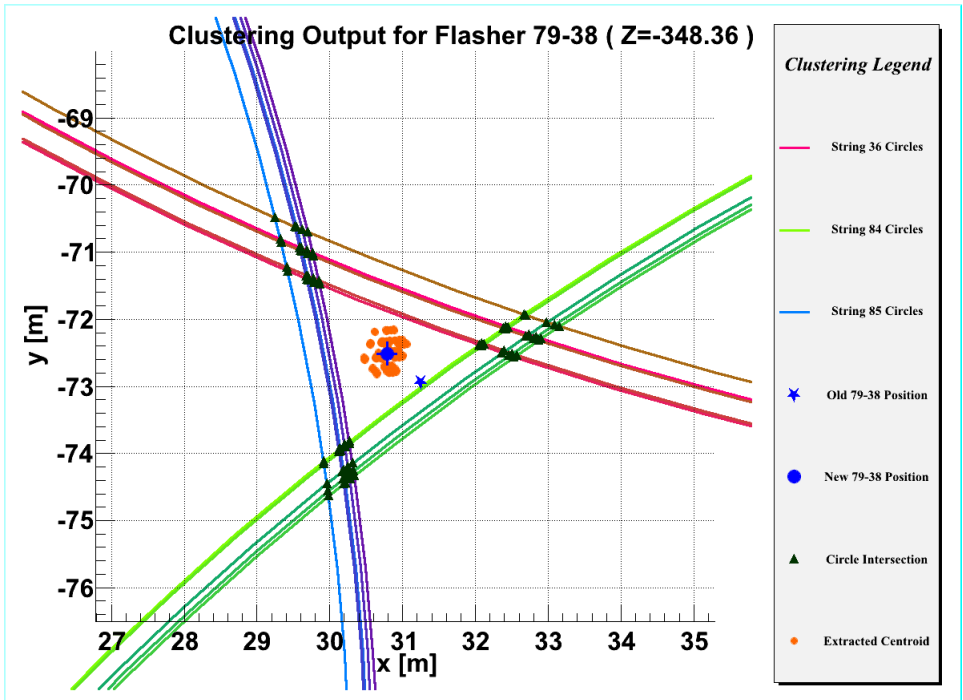


Figure 7.6: The distances measured by flashers for each DOM and the intersection points of measurements from DOMs on different strings. Figure taken from [78].

8. Method

While the x and y positions of the DOMs have not been calibrated in the ice, there have been many improvements of the reconstruction of events and ice modelling. The aim of the work presented here is to find positions of DOMs such that reconstructions and ice models better model our data.

8.1 Using Likelihood to Determine Positions

The overarching idea of this method is to find the DOM position that gives the highest probability for the observed data. In other words, we use maximum likelihood [81] to determine positions. For the spline table time PDF p , see section 6.5, track \bar{t} , photon time t , DOM position (x, y, z) and noise level n we get the following expression for the log likelihood.

$$\log \left(\prod_{\bar{t}} \prod_t (p(t|\bar{t}, x, y, z) + n) \right) \quad (8.1)$$

We can now search the space (x, y, z) for the maximum, which gives us the measurement of the DOM position. For this analysis, the noise level is set to 10^{-7} per ns. It is slightly lower than the measured rate, but this analysis is not very sensitive to the exact value.

8.1.1 Individual strings

If we try to fit x , y and z for all DOMs simultaneously we end up with over 15000 parameters to fit and finding an optimum would be very computationally expensive. We can remove z from the fit as it is already known to 0.2m between string and cm between DOMs in the same string. Also, we can fit one string at a time. We expect DOMs on the same string to have similar horizontal deviations, but as different tracks will use hits from different strings during reconstruction and the deviations between strings are not correlated this systematic should cancel out to a large degree. We remove hits from the string in question before reconstructing the track. This makes the evaluation of likelihoods independent of hits on other DOMs on the same string, which would have been a problem as we expect any shifts for DOMs in the same string to

be correlated. This allows us to reconstruct the tracks once for each string, and once that is done we can run 60 parallel jobs to make individual DOM position estimates.

8.2 Single Event Examples

As light travels out in a cone following the track, the likelihood is almost radially symmetric around the track (it would be if not for ice properties). Depending on the timing of the hits, we get two kinds of characteristic likelihoods. If the DOM is far away or the hit is late, we get a large area where it is plausible for a photon from a track to hit the DOM, see figure 8.1, while if the hit is early and the DOM is close to the track we get a very sharp likelihood, see figure 8.2. As the likelihood cannot go below the likelihood of noise, any position that would require the photon to travel faster than the speed of light has the same likelihood, which is the likelihood of noise.

8.3 Sum of Many Log Likelihoods

By summation of many log likelihoods, we get a relatively smooth function of DOM position. See figure 8.4 for a graph of the likelihood space. Next, we use a minimizer to find the maximum of the function, which gives us the estimate of the DOM position.

8.4 Error Estimation

For error estimation, we use bootstrap resampling [82]. When an estimator is not given as an analytical expression, it can be difficult to estimate its variance or other distributional properties. Bootstrapping is a method that is always able to give an approximate distribution of the estimator. The idea is to approximate the true distribution with the sample. So by making new samples by picking randomly from the original sample (with some events picked more than once, and some not getting picked at all) you get a distribution of estimates. Our error estimate is the standard deviation of this distribution. For an example of how it can look in this work see figure 8.5.

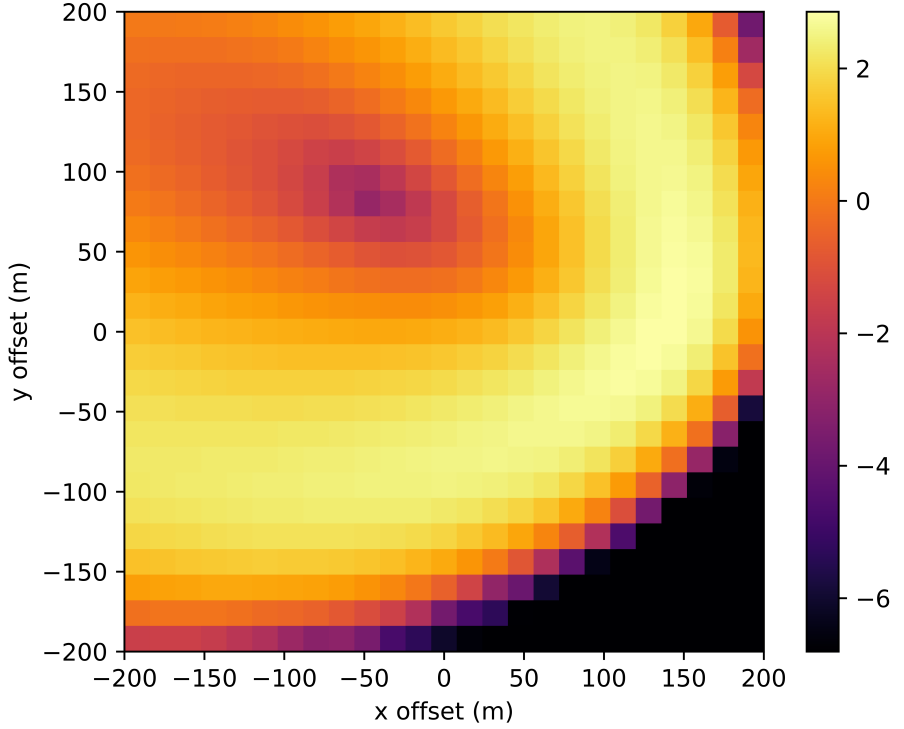


Figure 8.1: The log likelihood of the pixel centre minus the log likelihood at the centre of the top left pixel. Offset is defined as the DOM coordinate evaluated minus true DOM coordinate. Here the photon has arrived in the tail of the distribution, and we can see that the Cherenkov cone has passed the DOM at (0,0). As light travels further scattering causes the light cone to diffuse.

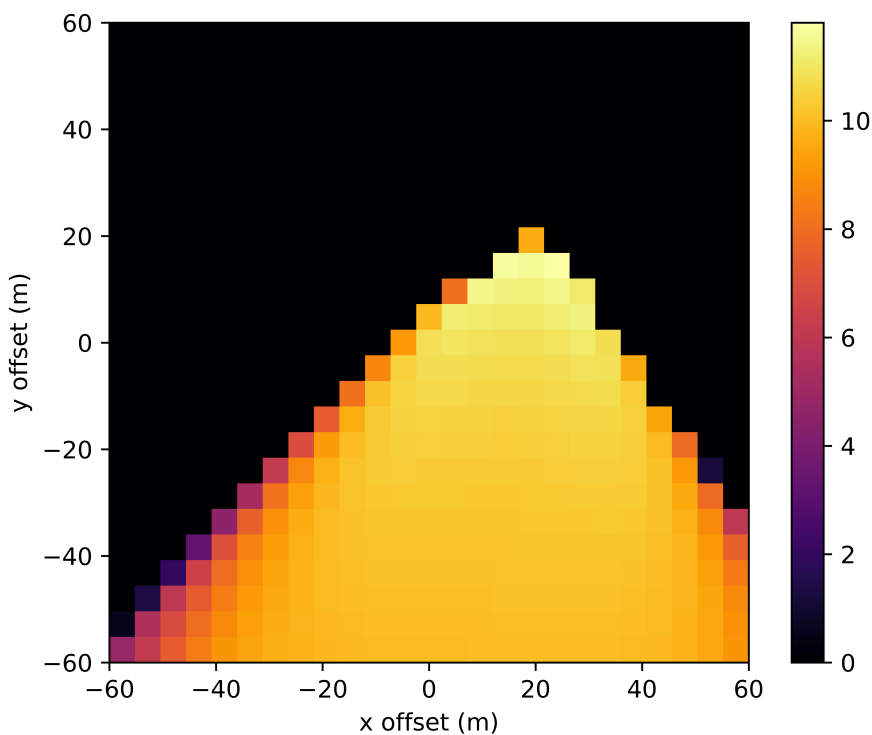


Figure 8.2: Values are defined the same as in figure 8.1. Here the photon has arrived on the Cherenkov cone. This causes most of the plane to get a likelihood based in the noise rate. Also noticeable is that when the Cherenkov cone lies in the plane the likelihood is almost flat. In figure 8.3 we have a schematic image of this phenomena.

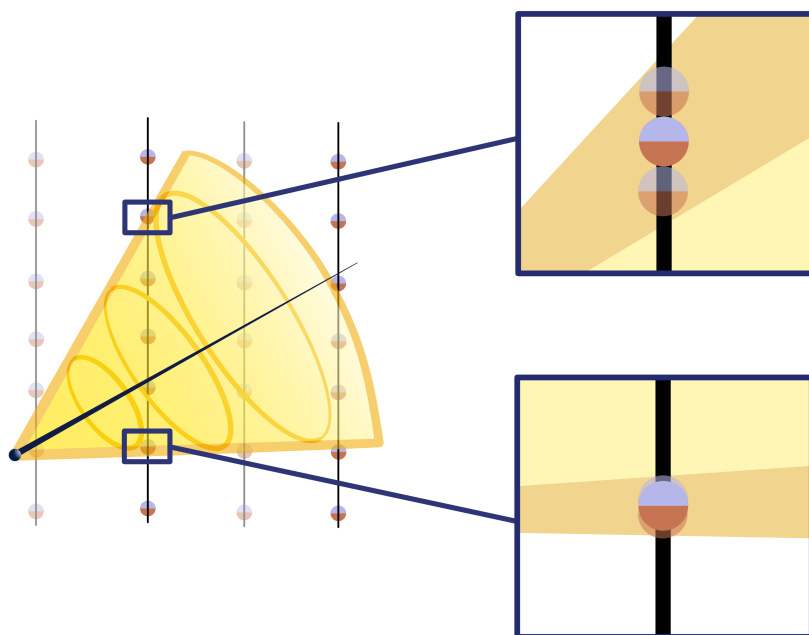


Figure 8.3: Artist depiction of the Cherenkov cone. As the Cherenkov cone passes a DOM it can be used to get good localisation in one dimension, the one perpendicular to the surface of the cone, while it gives an almost flat likelihood in the two dimensions in the surface of the cone. For example in the bottom box light hitting the DOM would give good vertical localization while not localizing it in the horizontal plane, similar to the event shown in figure 8.2. In the upper box the DOM the surface of the cone cuts the plane resulting in something like the event shown in 8.1

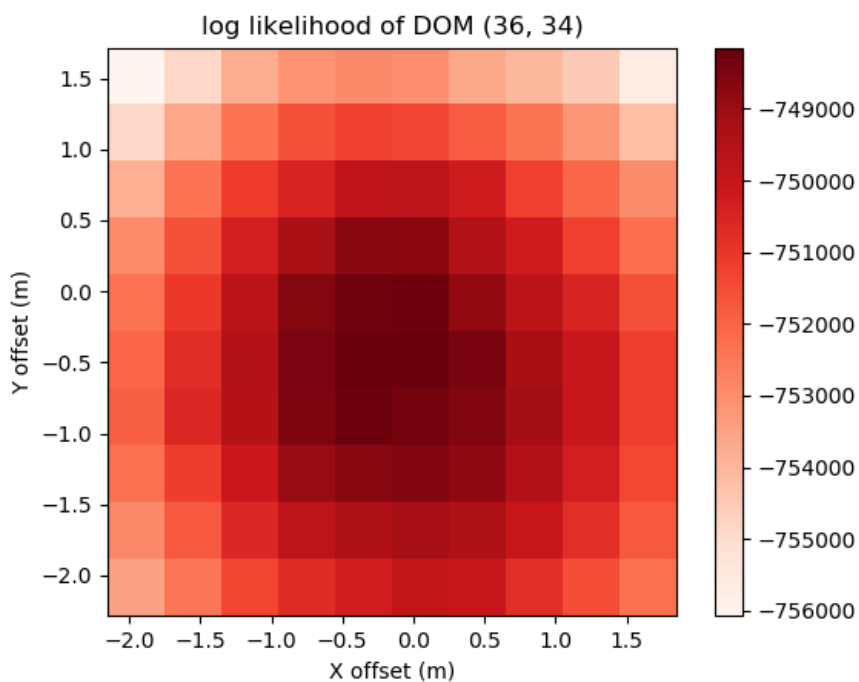


Figure 8.4: The log likelihood sum of 37377 simulated events. This is a relatively small sample, giving a result 0.5m off the true position.

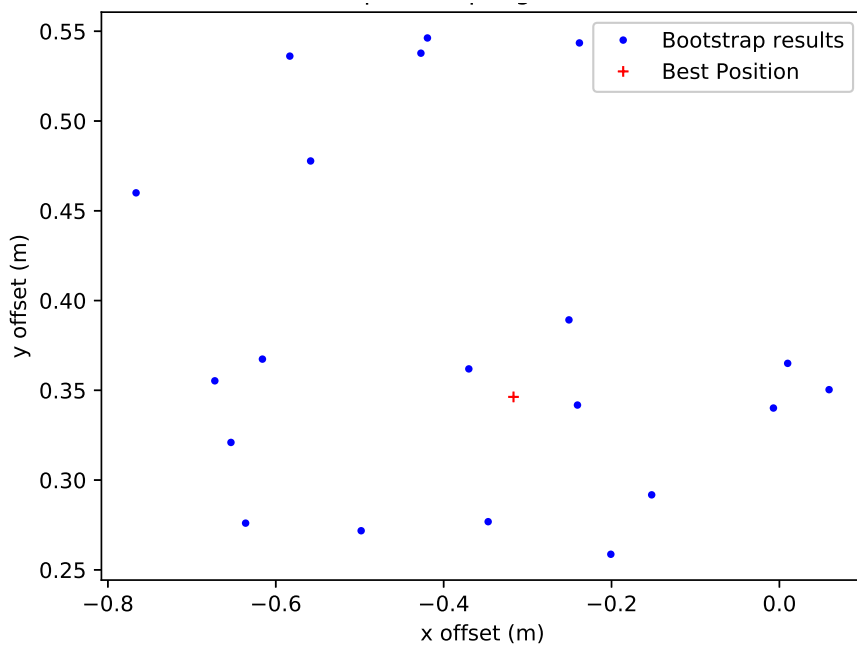


Figure 8.5: Example of best-fit DOM positions from bootstrap resampling. The best-fit position of the original sample is shown as a red cross.

9. Simulation Studies

Before applying the method in the previous chapter to real data, we want to apply it to simulated data. This will show whether, and how well, it works in an ideal setting where we know the true positions of the DOMs. The observed performance then sets our expectations for what may be achievable in the real detector. Studies on simulation give information about precision, robustness, how much data are needed, and what cuts can be applied that lead to an event selection that improves the performance of the method.

9.1 Simulation in IceCube

Most of the simulations done in IceCube are of cosmic rays air showers using CORSIKA [83]. While CORSIKA simulates all kinds of particles, only muons will be able to penetrate 1.5 km of ice to reach the in-ice part of the detector. Therefore, the IceCube collaboration has developed specialized simulations for propagating muons in ice. This has been expanded upon to also propagate electrons and taus, which can be created by neutrinos in charged current interactions in the detector. This code simulates any possible interactions as well as creates photons from Cherenkov radiation.

IceCube has also developed code for propagating photons in the ice. The optical properties of ice are very important and vary significantly between layers in the ice. Such properties are absorption length, scattering length and anisotropy. Current development tries to derive the anisotropy from grain size in the ice crystals, see reference [68]. As the photon propagation is very computationally heavy, many datasets are generated using a factor fewer photons while making the optical modules a factor bigger which gives a close approximation and can save a significant amount of computing time.

After the photon simulation, the detector response is simulated. It starts with determining if a photon hitting a DOM will trigger a PMT response, using the angular acceptance of the DOM and the quantum efficiency of the PMT. Next, the PMT response is simulated. Once the output from the PMT is generated, the electronics in the DOM are simulated and finally the communication between DOMs is simulated. The event will now go through the same triggers, filters, and reconstructions as a real event.

9.2 Weighting

The true energy distribution of cosmic rays follows a steeply falling power law, approximately $E^{-2.7}$. If the simulation used the physical spectrum of cosmic rays, large amounts of low energy events would be simulated and there would be very low statistics for higher energy events. So events are simulated with a different spectrum than the physical spectrum to generate more statistics for higher energy events. To restore the physical spectrum, events are given weights. When using weights, any histogram would have the same distribution as a histogram using real data, to the degree that the simulation simulates reality. The normalization of the weights is arbitrary. Raising or lowering all the weights make each simulation event represent more or fewer real events. This can also be thought of as changing the amount of real data-taking time that the simulation corresponds to. The default weights in IceCube are scaled such that one data file corresponds to 1 second of data.

9.3 Selection

In my analysis I have used data set 20904 which is the result of 76951200000 simulated events. Many of these will not be helpful to my analysis, so I look to make a selection. What I need is muon tracks that can be well reconstructed and hit many strings. First I want close to horizontal tracks as removing one string will still allow them to be reconstructed, for this reason I decided to use events that pass either the sun or the moon filter, as explained in section 4.3. Next, I want a minimum level of quality of the reconstruction. I achieve this by requiring 30 DOMs to be hit, not counting Deep Core strings.

9.3.1 Downsampling

I now have a selection of events, but they have the non-physical spectrum they were simulated with, and in my method I am unable to use the weights. This is because the likelihood of many low weight events will be very different from the likelihood of one event. I now generate values between 0 and 2.38 for each event. If the random number is less than the weight of the event, it is included in the sample. This results in an unweighted sample of events which has the same distribution in energy as the weighted simulation sample.

The value 2.38 was taken as the highest weight event surviving my cuts had that weight. That value also represents the inverse of the time in seconds one simulation file represents. So our simulation represents about 323000 s of data, or about 3.7 days. To confirm that the simulation represents data well some summary statistics are looked at. One such verification can be seen in

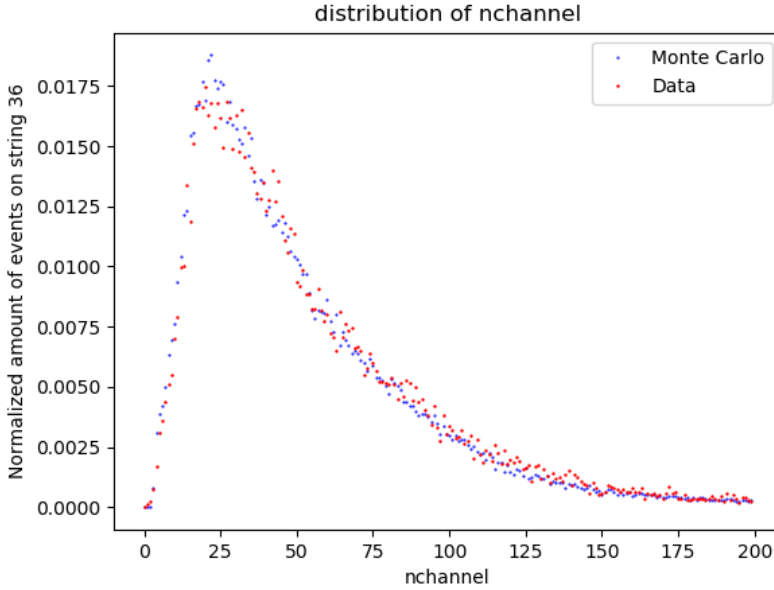


Figure 9.1: Histogram of number of DOMs hit per event, for events passing the moon or sun filters hitting at least one DOM on string 36. On the x-axis we have nchannel, which is number of DOMs recording data from an event. On the y-axis we have the fraction of the events for each nchannel. We do not expect perfect agreement as the simulation is randomly distributed around the year while the data is four successive days.

figure 9.1, where the distribution of number of DOMSs hit per event for four days of data is compared to four days of simulation.

9.4 Estimating x and y

In figure 9.2 we have our results for string 35 and 36. These strings are in the centre of the detector, see figure 9.3. All the plots are colour coded so that DOMs have the same colour in all plots. DOMs in IceCube are labelled such that DOM 1 is at the top of the string and DOM 60 at the bottom.

In the top left plots, we see, for each DOM the number of events giving a signal. The features we see in the plots are related to the ice properties and how they change with depth. More muons will reach the top of the detector, while the absorption length is greater at the bottom. At the very top there are fewer hits as muons hitting these DOMs going at an angle would not travel very far in the detector, lowering the chance of them passing our cuts. The

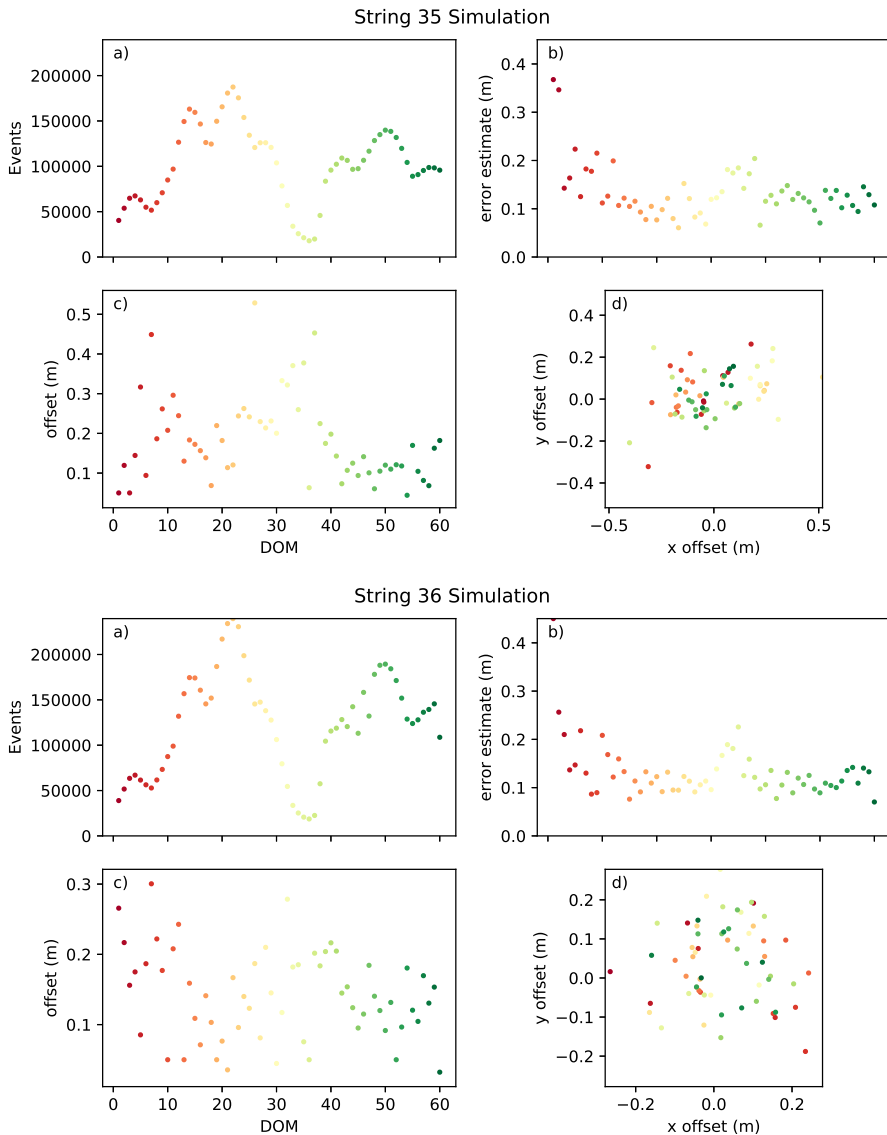


Figure 9.2: The top left shows the number of events for each DOM in the string. The top right gives error estimates from bootstrap. The bottom left gives the true error. The bottom right shows a scatter plot with DOM positions, where colour encodes DOM number in the same way as in other plots.

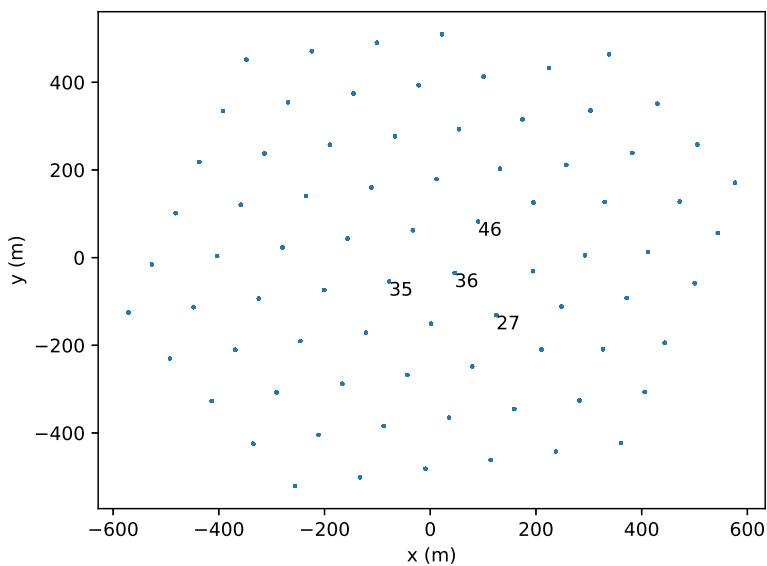


Figure 9.3: The nominal positions of the IceCube strings. For the simulation study, we will focus on 35 and 36, while when looking at data 27 and 46 are also included.

same is less true at the very bottom, where the DOMs are more likely to see far away muons, because of the clearer ice. In a range around DOM 35 we have a distinct feature called the dust layer. The ice here contains a lot of dust, obscuring the vision.

In the bottom right, we have the fitted positions for the DOMs obtained from the analysis. $(0,0)$ is the nominal position, which is also the true position in simulation. For these strings, there is no clear bias. We have most DOMs in a 0.2m spread around the true position.

In the bottom left, we have the distance to the nominal position. This information already exists in the bottom right plot, but any depth dependent features are easier to see in this format.

In the top right, we have error estimates from bootstrap. We can see that DOMs at the top of the detector and in the dust layer have higher error estimates. These are the parts where we have the least statistics. But the top error estimates tell us that there is also an effect from being on the edge of the detector. There is no clear correlation between error estimates for individual DOMs and the true error, but the scale of the error estimates gives us the scale of the true error. This has been true for previous runs with less data as well.

9.4.1 Performance in different parts of the detector

While we have seen the method work in the ideal scenario, we next check how it works in different parts of the detector. In figure 9.4 we can see the average shifts of DOMs on a string scaled up by a factor 60. Because of problems at the data centre only a tenth of the data was used, but the shifts for string 75 (top left corner) and string 4 (bottom edge) are above the statistical noise.

We can see that the edge and corner strings are pulled towards the centre. This implies that we have a systematic effect when our reconstructed tracks are not symmetrically distributed around the DOM. Here it might be possible to decrease this systematic shift by including tracks that do not hit a DOM and introduce the likelihood of seeing a track in the likelihood function. This would push out edge DOMs as the optimum is to be far away from tracks that were not seen in the DOM. But as the method gives very good results for internal strings, it was decided to try in data.

We see that we can determine the DOM positions for central strings to within 0.2m using data corresponding to 3.7 days of data taking. This is the same as the precision of existing z calibration and below the error introduced by our compression algorithm.

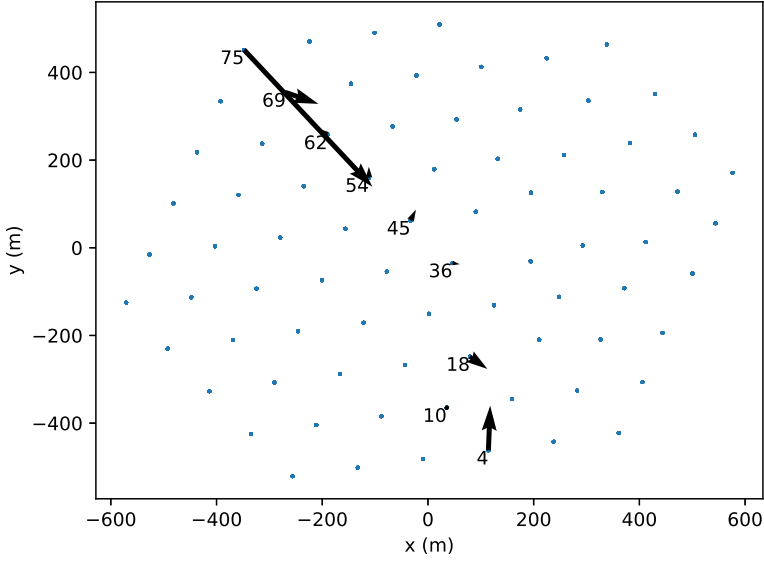


Figure 9.4: Arrows are the sum of the shifts for all 60 DOMs on the string. Strings included are 4, 10, 18, 36, 45, 54, 62, 69 and 75. It seems like we have systematic biases for strings 4, 69 and 75. The size of the bias shrinks with the number of nearby strings. 75 have the largest as it is on a corner, then string 4 which is on an edge, lastly string 69 which is next to a corner. On string 10, which is next to an edge, there is no measurable bias.

9.5 Estimating z

So the method works with simulated data, but once we run it on real data, how would we know if an apparent deviation from nominal is because of a modelling error or a correct measurement of DOM displacement?

To answer this, we can study how the algorithm performs fitting z positions in both simulation and data. As the z coordinates are known to 0.2m (see section 7.3.1), we can know how well we perform in data. Comparing performance in data to performance in simulation gives us a measure of the modelling error.

The only needed change is to let the minimizer fit the z coordinate instead of x and y . As our detectors have the PMT looking downwards, we expect a larger systematic error, as the detector response will be different for tracks above than for tracks below. For the x and y case our detector is symmetric up to the positioning of the bubble column.

In figure 9.5 we see the results for fitting the z coordinates on string 36. The top panels are the same as in figure 9.2, the bottom left panel shows the fitted z shifts from nominal with error bars. We can see that most DOMs have been moved 0.5m up with DOMs in the dust layer being moved further up and that DOMs at the top of the detector have larger errors. In the bottom right plot, we plot the difference between the obtained inter-DOM distance and 17m, the known separation of DOMs along the cable.

There are a few trends worth commenting on here. First, there is a systematic offset of 0.5 metre. Second, there is lower precision in the dust layer. Third, there is a 17-metre spacing, which is important as it is precisely known in data, since the cable was constructed with 17-metre spacing.

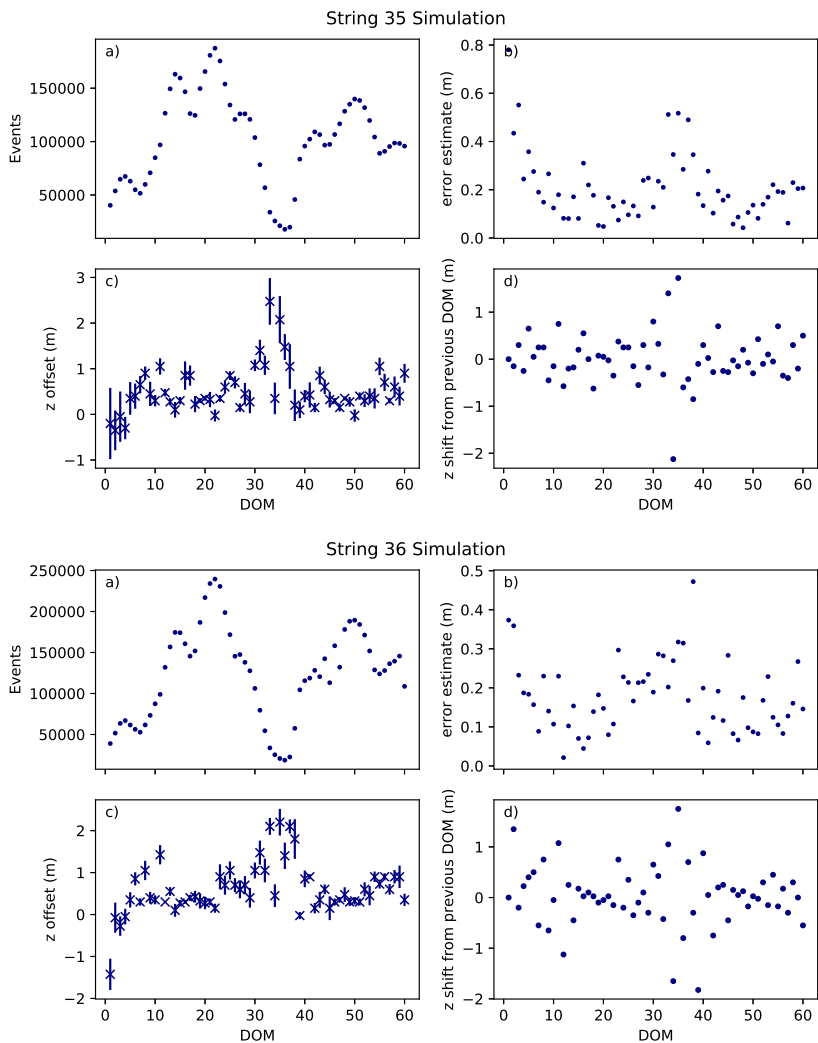


Figure 9.5: z calibration results a) The number of events per DOM. b) The error estimate given by bootstrap. c) The offset from previously calibrated positions. d) The DOM to DOM offset from nominal distance.

10. Results

We are now ready to look at the results in real data. We have seen in simulation a bias towards the centre of the detector. This bias seems to go away in less peripheral parts of the detector, resulting in down to 0.2 m precision in the xy -plane and 0.5 m in the z direction, see chapter 9. This can be achieved with eight days of data. In section 10.1 through section 10.4 I have used four days of data when the sun and moon are high on the sky, the filtering is the same as in section 9.3, and since the number of events falls rapidly with the zenith angle this gives us four times as much data compared to four average days. In the remaining section, the data has been expanded to 12 days.

10.1 Estimating z

Estimating z was never the goal of the analysis, as z had been determined to a precision of 0.2m. It was instead conducted to have something known to compare results with. It is expected that the results in z have more systematic errors as there are no symmetries to cancel any error out.

As we can see in figure 10.1 and 10.2 we have a large systematic error causing the z estimate to position the DOMs a few metres above the known position for all strings. There are strong edge effects, but we have previously seen in the simulation that the asymmetries introduced at the boundaries are not handled by the method. We can see that the algorithm does correctly reproduces the distance between DOMs which can be an estimate of the statistical error.

That the algorithm wants to move all DOMs up has to be to a large part because of the different likelihoods used by reconstruction and in my algorithm. We can also see that there is a feature probably related to the dust layer but shifted downwards.

We now have a more direct measure of the uncertainty as a second geometry calibration method has been developed, see section 10.6, but these results still included for completeness.

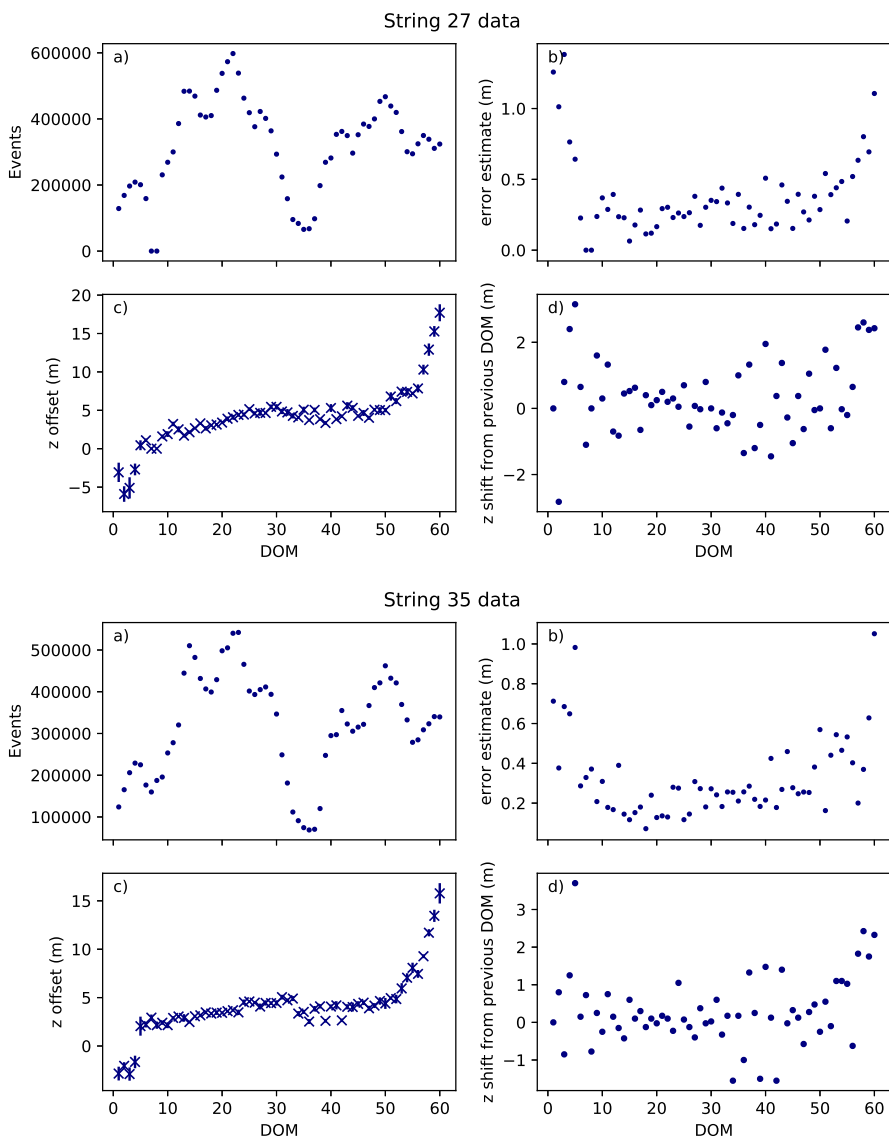


Figure 10.1: z calibration results a) The number of events per DOM. b) The error estimate given by bootstrap. c) The deviation from previously calibrated positions. d) The DOM to DOM deviation from nominal distance.

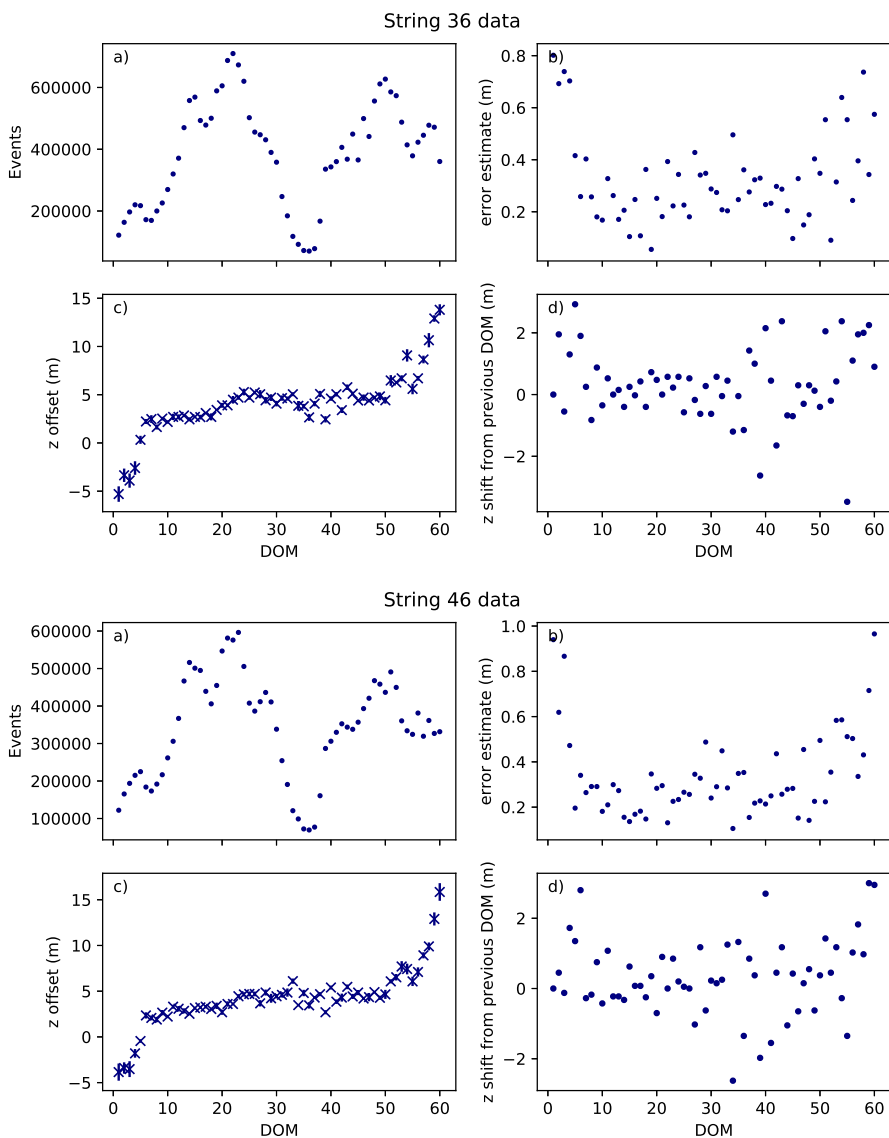


Figure 10.2: z calibration results a) The number of events per DOM. b) The error estimate given by bootstrap. c) The offset from previously calibrated positions. d) The DOM to DOM offset from nominal distance.

10.2 Estimating x and y

While the z result showed a 5-metre systematic shift, we expect any systematic to be much smaller when estimating x and y in the middle of the detector, as the problem is much more symmetric. My results for x and y are shown in figures 10.3 and 10.4 and compared to drill data in the next section.

For string 35 there are several DOMs that do not have any results. This is because of problems at the data centre in Wisconsin when I was processing the data.

The first feature that we notice is that the offset from nominal and error estimate are larger for the top five DOMs. While we did not see this for the top DOMs in simulation, we have seen edge effects in z and on edge strings. That the error estimate from bootstrap is larger than for the rest of the string tells us that we need more statistics at the top of the detector. There is also a similar effect at the bottom of the detector but less pronounced. The clearer ice at the bottom allows the bottom DOMs to see more events which probably alleviated the problem to some degree.

A second interesting result is that in the dust layer we have fewer events than at the top but the error estimate and nominal offset does not stand out compared to regions with ten times as many events. It is not known why that is, but some possibilities are that events seen in the dust layer are closer to the DOM, brighter or that the dust layer is better described by our ice model.

Our third observation is that, out of the 4 strings studied here, string 36 has the largest deviation from nominal. String 36 is the most central of all our strings so it would have the least contribution from any asymmetries which has dominated our systematics in Monte Carlo. If the large deviations for this string were a consequence of an incorrect ice model we should see an effect on nearby strings as ice properties are the same in almost horizontal layers. With string 36 located between string 27, 35 and 46 we can be reasonably certain that a large part of this result is due to an actual positioning error.

The fourth item we can read of these charts is that we have small DOM to DOM movement as we traverse the string. This implies that we are measuring either a systematic error or a physical displacement. It can only in part be explained with correlated statistical errors as bootstrap in that case would give error bars large enough that it would be reasonable that all DOMs have the same x and y position. This can be easier seen in the plots in the next section.

10.3 Stability of solution

When the tracks used for the geometry calibration were reconstructed, errors in the existing geometry database will have affected the results, and will therefore

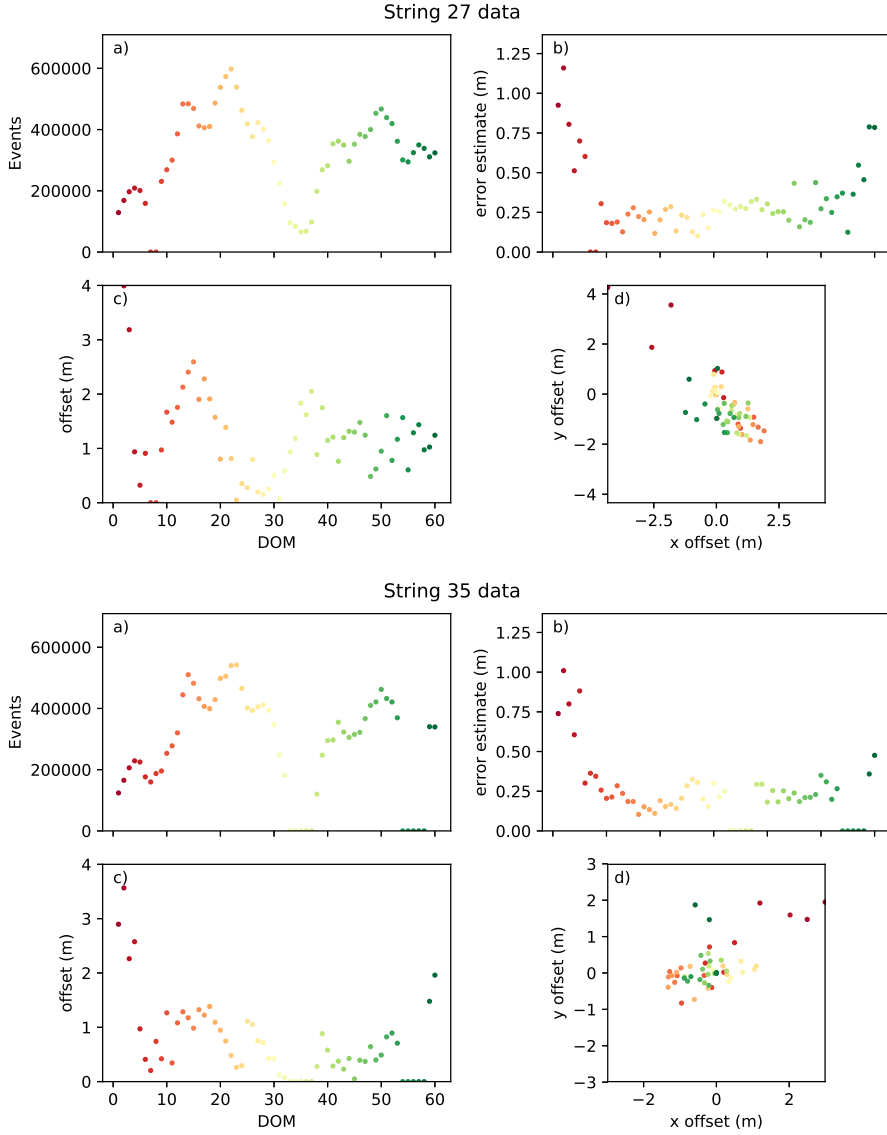


Figure 10.3: x and y results for string 27 and 35. The colour correspond to DOM number with red at the top of the detector and green at the bottom. a) number of events per DOM. b) error estimate given by bootstrap. c) offset from nominal positions. d) the reconstructed positions in the horizontal plane.

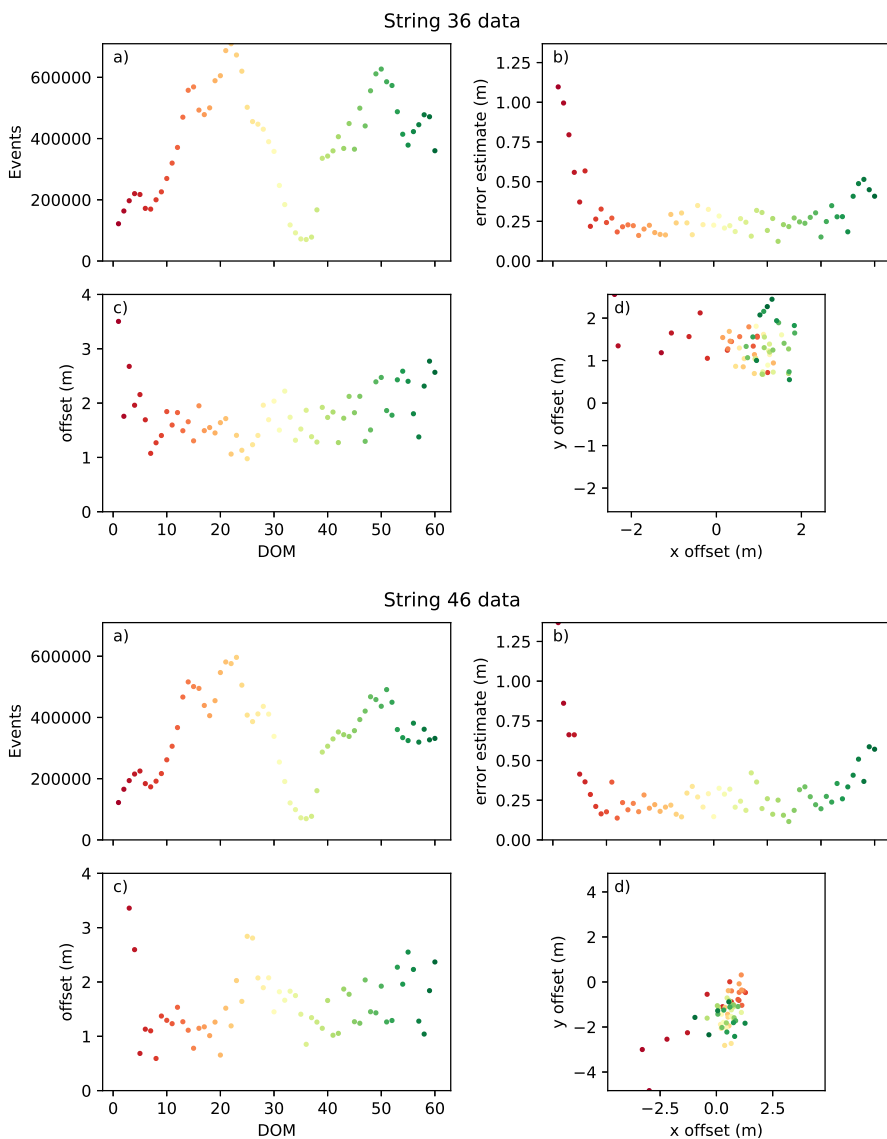


Figure 10.4: x and y results. The colour correspond to DOM number with red at the top of the detector and green at the bottom. a) number of events per DOM. b) error estimate given by bootstrap. c) offset from nominal positions. d) the reconstructed positions in the horizontal plane.

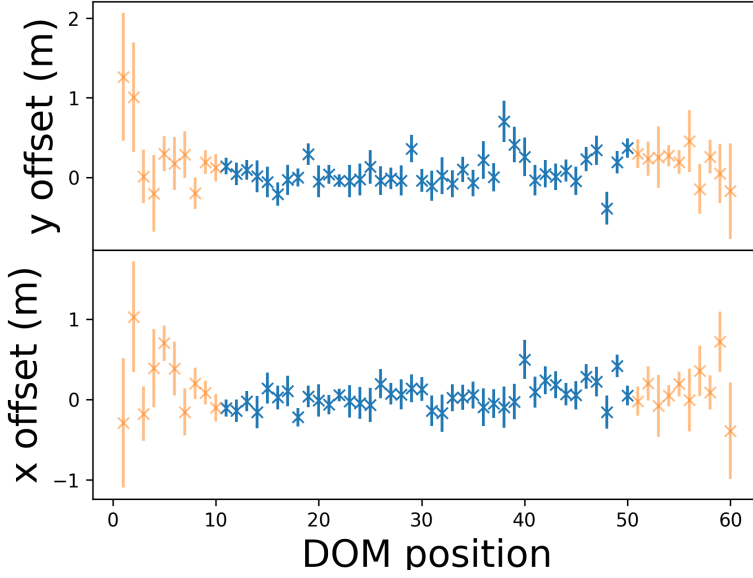


Figure 10.5: The movement of DOMs on string 46 compared to previous iteration of the algorithm. Offset here refers to the difference between result and the geometry used for the algorithm. i.e. the results shown in section 10.2. The x denotes best fit result with the vertical bar denoting uncertainty. Data has been increase to twelve days including the four days used previously. We can see that the result is stable with fluctuations resulting from adding more events. In blue we have marked the 40 middle DOMs which will be used to calculate string means. As our uncertainty and systematic errors grow towards the edges 10 DOMs on each side will still be fitted but not included when calculating string means.

also have some limited impact on the new geometry calibration. To check for the stability of our solution, the alignment procedure was re-run with tracks reconstructed using the new geometry. This was done for strings close to string 36 as the large shift of that string would affect track reconstruction. In figure 10.5 we see the results for string 46, when using the updated geometry and expanding the data to 12 days of data. We find that the position is stable, with shifts that are expected from the change of data.

10.4 Comparison with drill data

During drilling, the depth was recorded in three indirect ways: pressure, hose payout, and cable payout. Together with the recorded tilt of the drill head, it is possible to reconstruct the drill hole. This can be done both on the way down

and on the way back up. But since the tilt of the drill head should shape the hole on the way down but not on the way up, the hole reconstructed from down going data is expected to be more reliable. Recorded drill data exist for about half of the drill holes.

The drill data have never been trusted and are not used in any analyses. But if this analysis confirmed the drill data, that would give us confidence in both methods. In figure 10.6 and 10.7 I compare my results with position data estimates using drill data recording both during descent and ascent of the drill.

Sadly, there is no significant correlation. But it may be possible that with more data, one could be able to make out the oscillations we see in drill data. This should be doable with Fourier analyses to find the most significant frequencies and see if we have the same frequencies in the oscillations my method measures. These oscillations are related to the drill head rotating, which would make it drill in a corkscrew pattern.

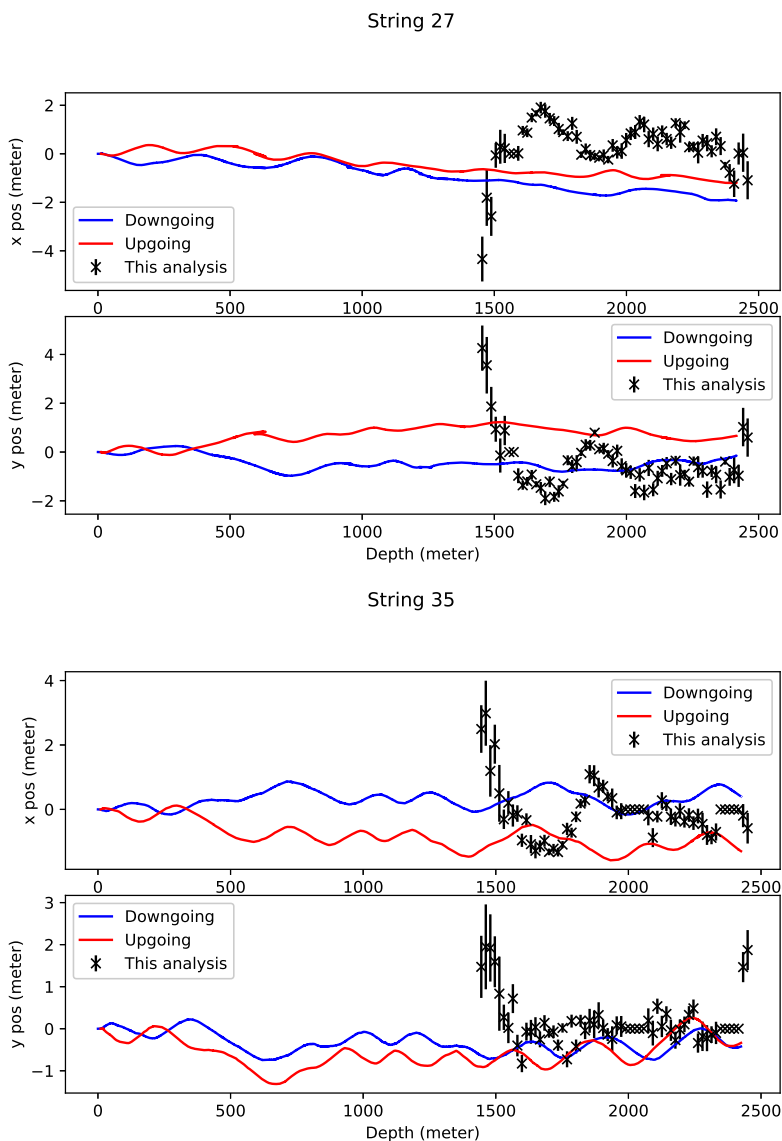
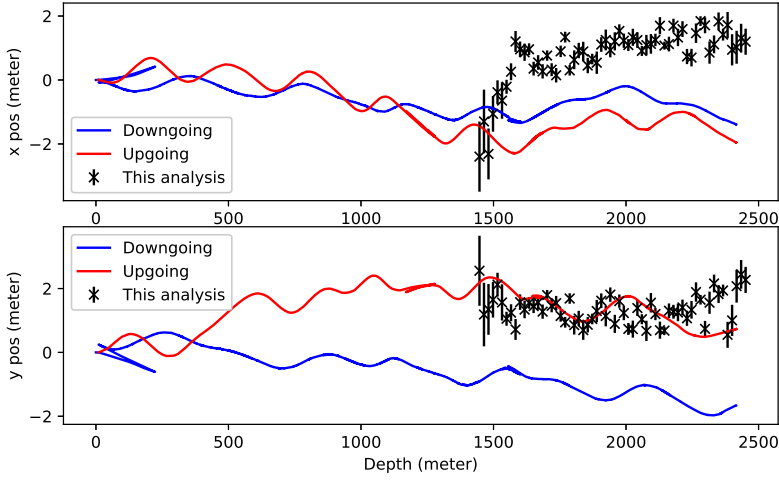


Figure 10.6: Blue is the drill location reconstructed from the recording during descent. Red is the drill location reconstructed from the recording during ascent. Result from this analysis with error bars are in black.

String 36



String 46

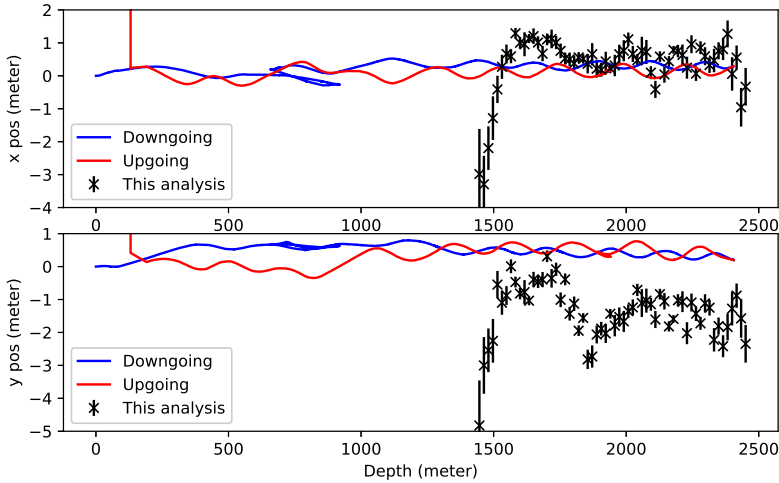


Figure 10.7: Blue is the drill location reconstructed from the recording during descent. Red is the drill location reconstructed from the recording during ascent. Result from this analysis with error bars are in black. Both these holes have the drill being retracted over a hundred metres during drilling. This could be because the drill got stuck or some other technical issue. The up going data for string 46 has the string move 100 metres suddenly. This part has been removed as the re-scaling removes all details.

10.5 Method for Geometry Calibration using LED Flashers

For flasher calibration, there is a standard method. Single DOMs light one or all LEDs, after which the waveforms recorded by nearby DOMs are saved. The waveforms are the PMT response sampled in 25ns intervals. The samples can be used to calculate a likelihood value [84] when comparing to simulation. To avoid saturation effects of the PMT which are not simulated, intervals behind the peak of the light distribution are used. Different values of the parameters are then used in simulation to find a set of best fit parameters. Usually the DOM positions are fixed while the ice properties are varied to calibrate the ice model. But if the ice properties are fixed and positions are varied, the method can be used to calibrate positions. The statistical uncertainty can then be calculated by doing resimulations and see the spread of likelihood values.

Recall from chapter 10.2 that string 36 was the only one of these four strings that was found with my geometry calibration to have a significant offset from the nominal geometry. In figure 10.8 we can see that the shift in string 36 has produced an improved fit to flasher data, while the other strings where DOMs were clustered around the nominal position show no net change. These results, based on LED flashers, strengthen the case that the offset seen for string 36 with my method is real. Moreover, if we plot the LLH values versus DOM number (figure 10.9) we see that the top DOMs give bad fits. Removing the top 10 DOMs gives an improvement on the description of flasher data on all strings. These results inspired Martin Rongen to attempt a new calibration of all string positions using flasher data.

10.6 Comparison of Flasher and Muon Geometry Calibration Results

In figure 10.10 we can see the results for both methods for the strings in central parts of the detector, where my method is expected to work. We can see that the two methods tend to agree when they fit larger shifts (greater than $\tilde{1}$ m). Where the results appear to disagree, the fitted shifts are small and close to the nominal geometry positions. As discussed below, this is within the expected range of fluctuations of the methods.

In figures 10.11 through 10.14 we look at the detailed results for some specific strings, for the other strings see appendix A. As the flasher method only fits one x and y for an entire string, the individual DOM positions fitted by the muon method are treated as statistical fluctuations from a straight string to make comparison easier. We can then use them to determine the mean

position and the statistical uncertainty of the mean.

In figures 10.11 and 10.12 we can see that the results for strings 34 and 35 are consistent with the nominal location. We can also see that the statistical uncertainty is much larger in the flasher method, where the uncertainty of the string mean position is comparable to the spread of individual DOM positions from the muon method. It should be noted that the flasher method is using a more up-to-date ice model, so the muon results are expected to have a greater systematic error. But on the other hand, the ice model has generally been the biggest source of systematic uncertainty in IceCube so to see that the two methods using different ice models agree gives good support for both methods.

The same conclusions hold when looking at strings where there are significant shifts detected. In figure 10.13 we find very good agreement with a shift of 1.5 m from the nominal position for string 36. Not only did the muon fitted position improve the flasher results, but when the flasher method is allowed to fit the string position, it converges to the same position as the muon method. That both models agree on string shifts even using different ice models, which is the largest systematic in IceCube, is the best evidence that we have measured a real effect.

A string that is also of interest is string 44, see figure 10.14. Given the large spread of individual DOM positions given by the muon method, it may be interesting to look in more detail. In figure 10.15 we can see that neighbouring DOMs are close to each other. The topmost DOMs are in the top left corner and the string continues down to the bottom right where it turns and ends up in the middle. The change of direction is an expected behaviour as the hose twists as it gets unrolled during drilling. This is some evidence that geometry calibration on a DOM level is possible.

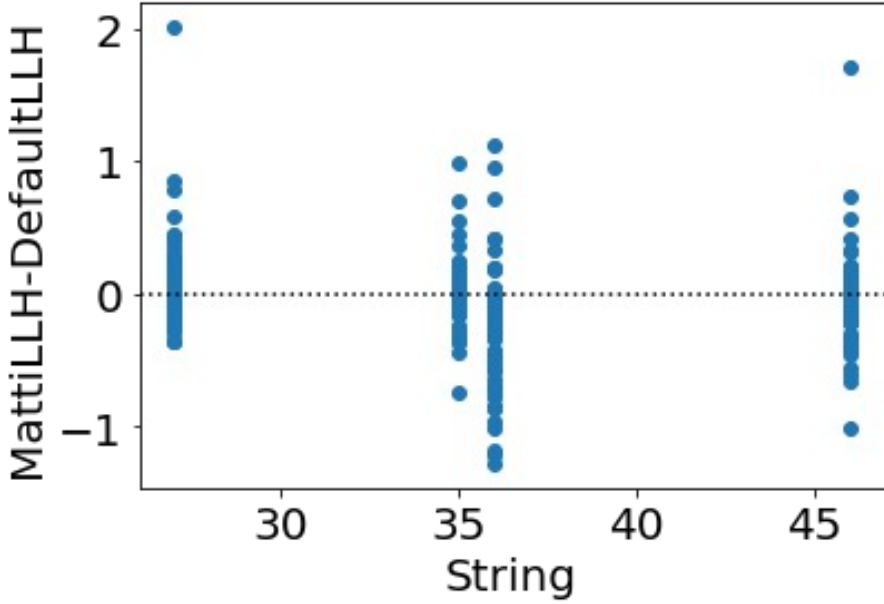


Figure 10.8: Difference in the log-likelihood value for flasher data between simulation using the new geometry compared to the nominal geometry. A negative value indicates an improvement. [85]

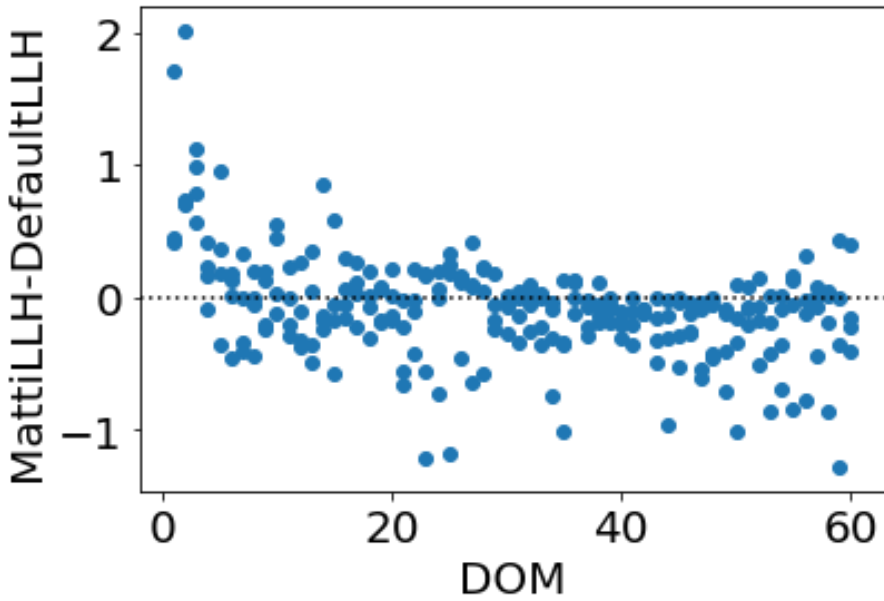


Figure 10.9: Changes to flasher LLH with the new geometry. Negative values show an improvement. [85]

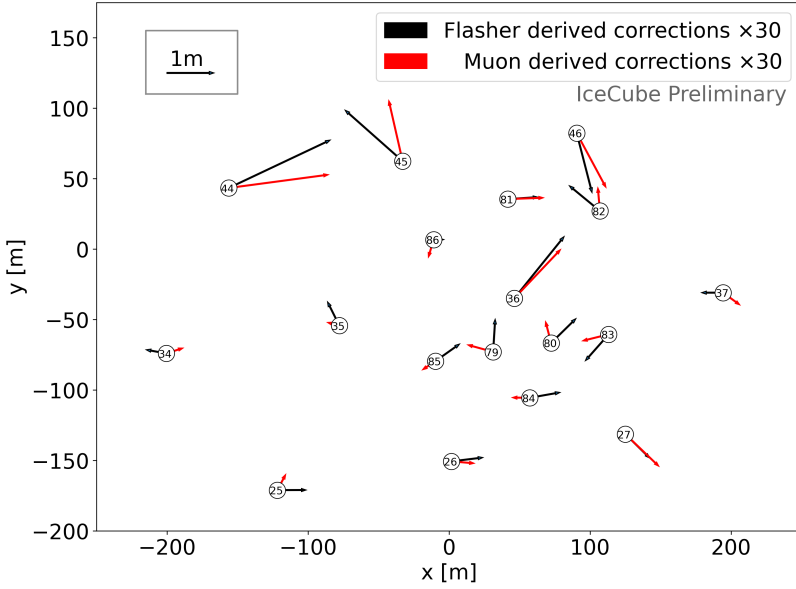


Figure 10.10: Fitted x and y coordinates of the central IceCube strings. The circles denote the nominal positions. The red arrows are the corrections found by the muon method. The black arrows are the corrections found by the flasher method. The corrections are scaled up by a factor of 30 for readability. The corrections agree better with each other than with the nominal position, unless the corrections are very small. [1]

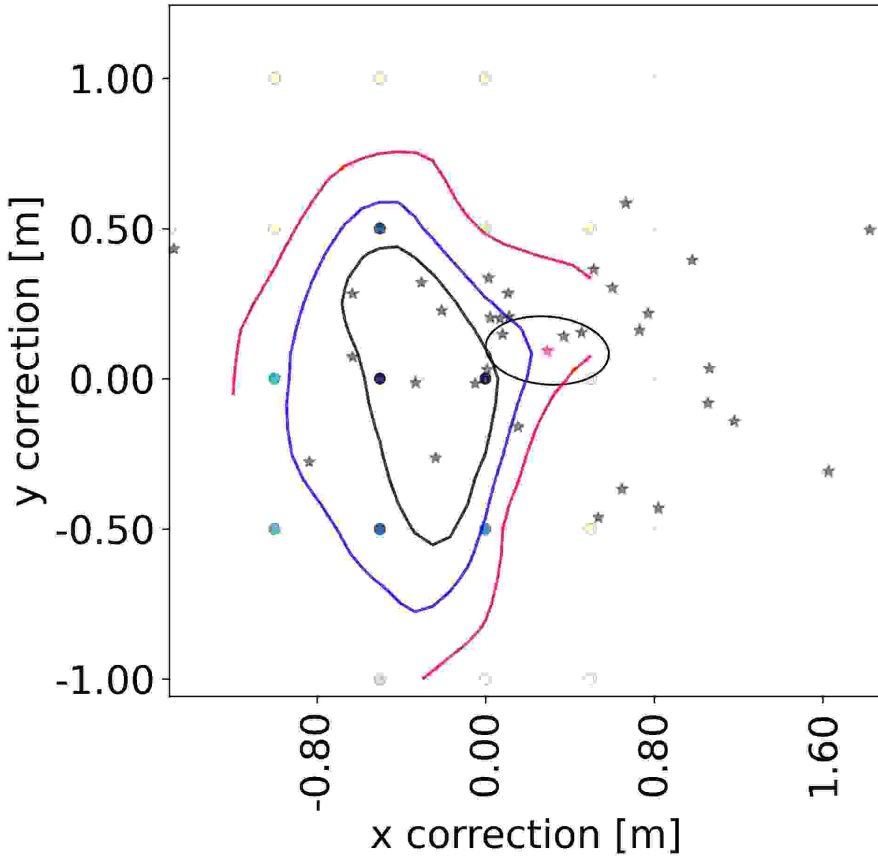


Figure 10.11: Flasher and muon method results on string 34. The grey stars are individual DOMs from the muon method. The red star is the mean of the DOM positions from the muon method. The ellipse gives the 68% confidence region of the statistical uncertainty. The coloured circles are the grid points for the flasher method grid search, and the colour gives the delta LLH value compared to the best value found. The contours give 68%, 95% and 99.7% confidence regions of the statistical uncertainty. We can see that both results are consistent with the nominal position $((0,0)$ i.e. no correction). [85]

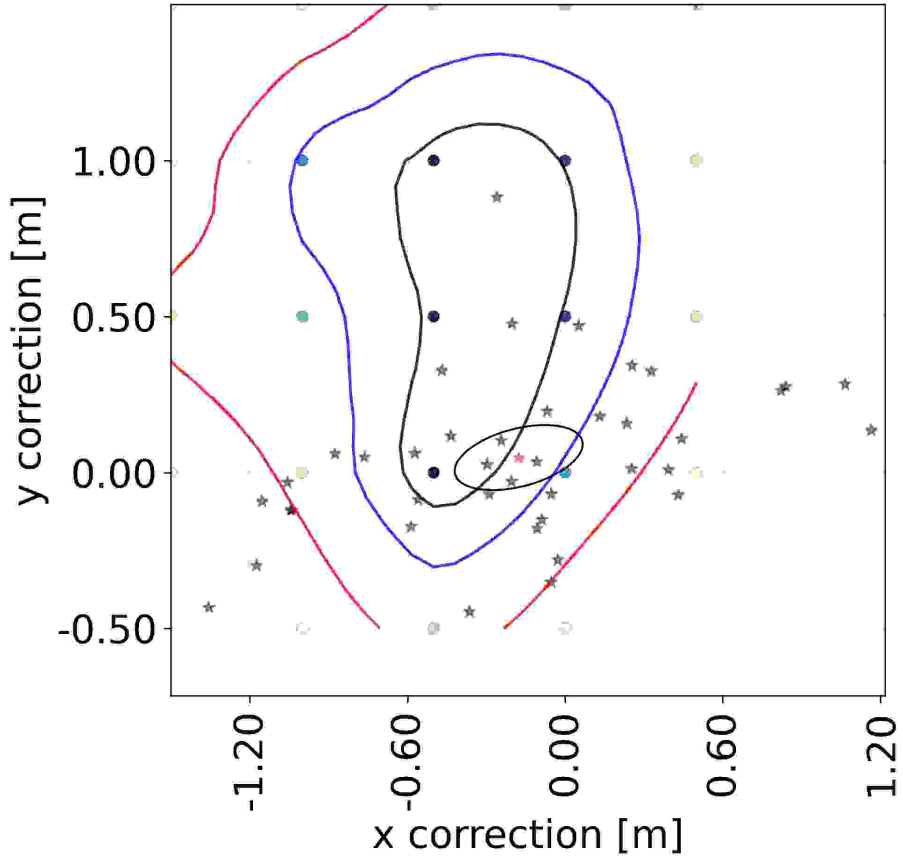


Figure 10.12: Flasher and muon method results on string 35. See figure 10.11 for a detailed description. Here we can also see that the results are consistent with nominal, as in figure 10.11. [85]

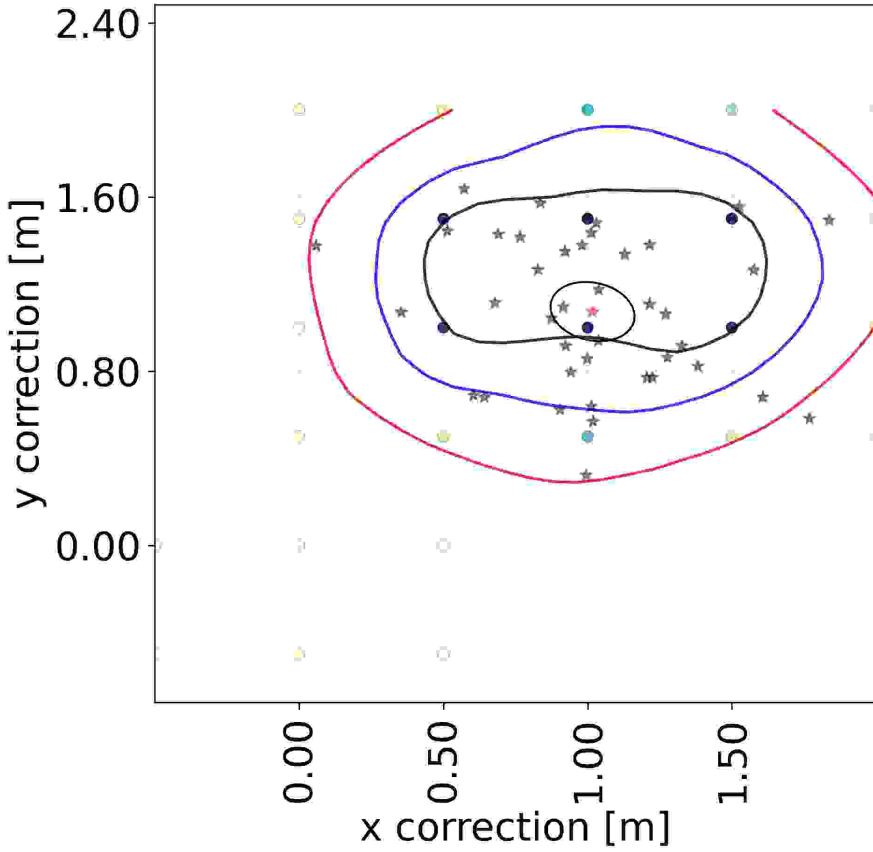


Figure 10.13: Flasher and muon method results on string 36. See figure 10.11 for a detailed description. The two methods agree on a shift of about 1.5 m from the nominal position assumed in standard IceCube geometry. [85]

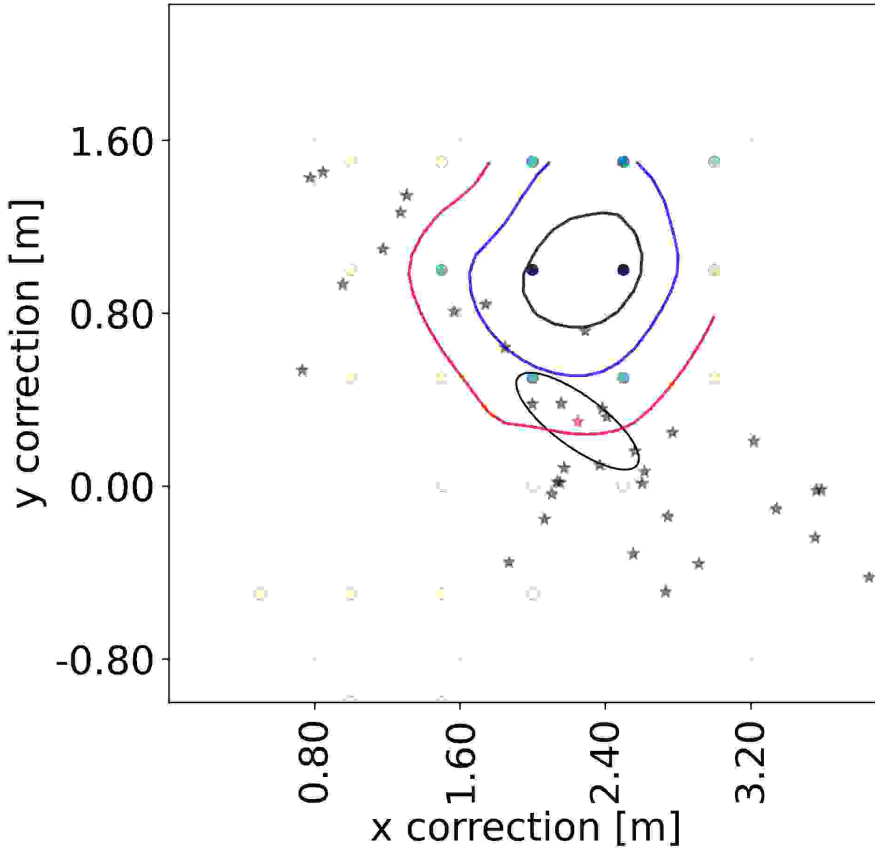


Figure 10.14: Flasher and muon method results on string 44. See figure 10.11 for a detailed description. Both methods arrive at a sizable shift of about 2.5 m. We can see that the muon methods finds a large spread in the individual DOM positions. This could be an indication that the string is not straight in the detector volume, see figure 10.15 for more details. [85]

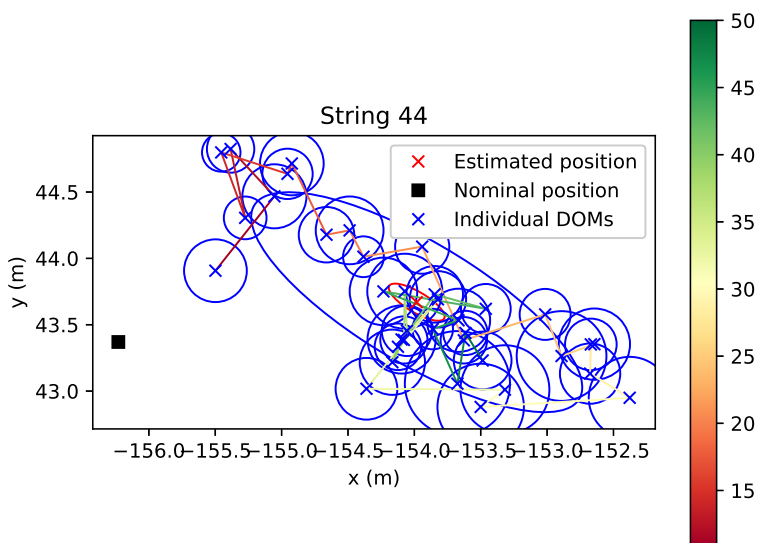


Figure 10.15: The DOM positions found for string 44 using the muon method. Circles are statistical uncertainty. The lines connects neighbouring DOMs starting at DOM 11 in red to DOM 50 in green.

Part IV

Anisotropy Modelling

11. Photon Propagation in Ice: Anisotropy and Birefringence

Ice modelling in IceCube was introduced in section 5.1. This chapter will discuss the recently understood anisotropy of light propagation. Most of the information in this chapter is based on [86] where more details are available.

11.1 Birefringence

A birefringent material is a material where the refractive index depends on the polarization and direction of light. These materials can have two or three refractive indexes. Ice has two refractive indices, see table 11.1. The index for extraordinary rays is for photons with polarization along the symmetry axis of the ice crystal, while the ordinary ray refractive index is for other polarizations. This causes light to split into two refracted and two reflected rays when crossing an ice grain boundary.

11.2 Anisotropy in IceCube

Originally, it was assumed that ice properties were uniform in horizontal directions (except for tilting of the ice layers). As data were collected, it was found that light did not propagate in the same way in every direction. In figure 11.1

wavelength (nm)	n_o	n_e
405	1.3185	1.3200
436	1.3161	1.3176
492	1.3128	1.3143
546	1.3105	1.3119
589	1.3091	1.3105
624	1.3082	1.3096
691	1.3067	1.3081

Table 11.1: The refractive indices in ice of ordinary and extraordinary rays. [87]

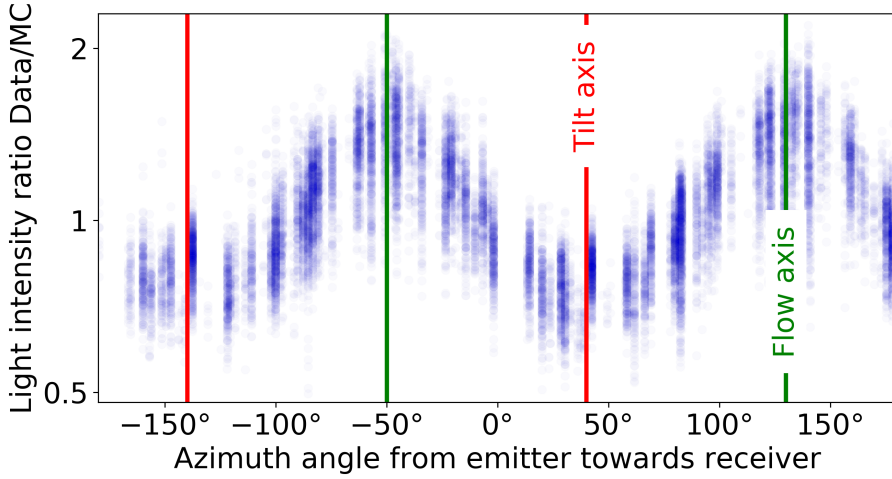


Figure 11.1: The ratio of received light in data and Monte Carlo simulation (before anisotropy effects are included) as a function of azimuth angle. Each point is a pair of light emitting and receiving DOMs at the indicated angle from each other at 125 m distance. In this simulation, there is no dependence on the azimuth angle. [86]

we can see that twice as much light is received by DOMs that are along the ice flow relative to the light emitter compared to DOMs perpendicular to it. The first effort to model this was to add a degree of freedom, allowing the scattering to depend on azimuth [88]. After fitting, it was possible to reproduce the azimuthal dependency of light intensity, but not the photon arrival time profile.

11.3 Birefringence in IceCube

Instead of modelling the ice properties as driven by impurities, the impact of the birefringent properties of ice has been investigated. As ice is exposed to stress it deforms, which in turn influences the ice crystal orientation [90] [91] [92]. This orientation is described by the crystal symmetry axis (c-axis). The distribution of c-axes is often described by Woodcock parameters [93]. These are a function of the ordered normalized eigenvalues S_1 , S_2 and S_3 of the orientation tensor. The orientation tensor is a way to parameterize and describe the distribution of symmetry axes directions. Figure 11.2 shows distributions of symmetry axes at different depths as measured by Voigt [89].

The effect of this alignment of the c-axes can be studied in simulation. Light was decomposed into two components, the ordinary ray and the extraordinary ray, thus leaving four possible photon paths for each surface crossing.

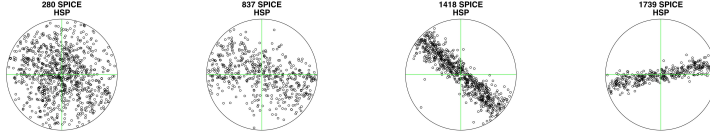


Figure 11.2: Distributions of symmetry axes of ice crystals at depths of 280, 837, 1418 and 1739 metres, measured from ice cores extracted at the South Pole [89]. Each point is the direction of the symmetry axis on a Schmidt equal-area projection. This projects half a sphere onto a disk. The middle of the disk is vertical and the edges are horizontal directions. In the leftmost plot we see a almost uniform distribution and at increasing depth, the symmetry axes become more aligned with a vertical plane. This is know as a girdle fabric. The azimuthal orientations of core samples are not known, but the girdle planes are assumed to be transverse to the flow [89].

This has been simulated for 1000 crossings to see what large scale behaviour can be derived from the microstructure. The results show that for initial light directions at an angle $0 < \theta < \frac{\pi}{2}$ to the flow axis, the distribution of directions after 1000 crossings becomes skewed towards the flow axis. An artist conception of the overall effect is illustrated in figure 11.3.

11.4 Modelling of Birefringence

It was found empirically that a 2-D Gaussian probability distribution provides an acceptable description of the final angles of photons after travelling some distance ΔL . Each original direction will have a unique Gaussian but the following parameterization in terms of η , the angle between the photon travel direction and the flow axis, was found to be a good fit. The deflection in the plane perpendicular to photon propagation (which here is called the xy plane), after a step ΔL is sampled from the bivariate Gaussian specified by

$$m_x = \alpha \cdot \arctan(\delta \cdot \sin \eta \cdot \cos \eta) e^{-\beta \sin \eta + \gamma \cos \eta} \quad (11.1)$$

$$\sigma_x = A_x e^{-B_x (\arctan(D_x \sin \eta))^{C_x}} \quad (11.2)$$

$$\sigma_y = A_y e^{-B_y (\arctan(D_y \sin \eta))^{C_y}} \quad (11.3)$$

where m_x is the mean deflection angle, $\sigma_{x,y}$ is the standard deviation. x is deflection in the direction towards or away from the flow axis, while y is the deflection in the perpendicular direction. The 12 free parameters are fitted to different realizations of birefringent ice properties. The birefringence properties of the ice are described by crystal size, elongation, and the two Woodcock parameters $\ln(\frac{S_1}{S_2})$ and $\ln(\frac{S_2}{S_3})$. The ice in the IceCube volume is a

so-called girdle fabric, ice crystals with c-axes distributed along a plane or in terms Woodcock parameters $\ln(\frac{S_1}{S_2}) \ll \ln(\frac{S_2}{S_3})$. The exact strength of the fabric cannot be constrained by the IceCube data, so the Woodcock parameters are set to $\ln(\frac{S_1}{S_2}) = 0.1$ and $\ln(\frac{S_2}{S_3}) = 4$ [93]. The Woodcock parameters at a depth of 1739 metre have been measured to $\ln(\frac{S_1}{S_2}) = 0.02$ and $\ln(\frac{S_2}{S_3}) = 3.7$ [89], but the measurements do not cover the entire detector depth. The crystal size and elongation are degenerate in IceCube data, and the elongation is set to 1.4, leaving only crystal size as a fit parameter.

Models that account for the birefringence effect described above have shown a large improvement in data/simulation agreement. It was found that the remaining disagreement could be further reduced by adding an azimuth dependent absorption parameter, but a physical explanation for this is not known. So in summary for each 10 metre layer of ice we fit crystal size, scattering coefficient, absorption coefficient and absorption anisotropy.

As discussed in chapter 6 many event reconstructions use spline tables, fitted to simulation, for likelihood evaluation. Originally, these simulations only modelled scattering and absorption, not anisotropy. For cascade events, spline tables have recently been created using a birefringent ice model in the simulation, but it has so far not been done for muon tracks. The next chapter will discuss the work to create new spline tables for muon tracks to predict photon arrival time distributions at each DOM.

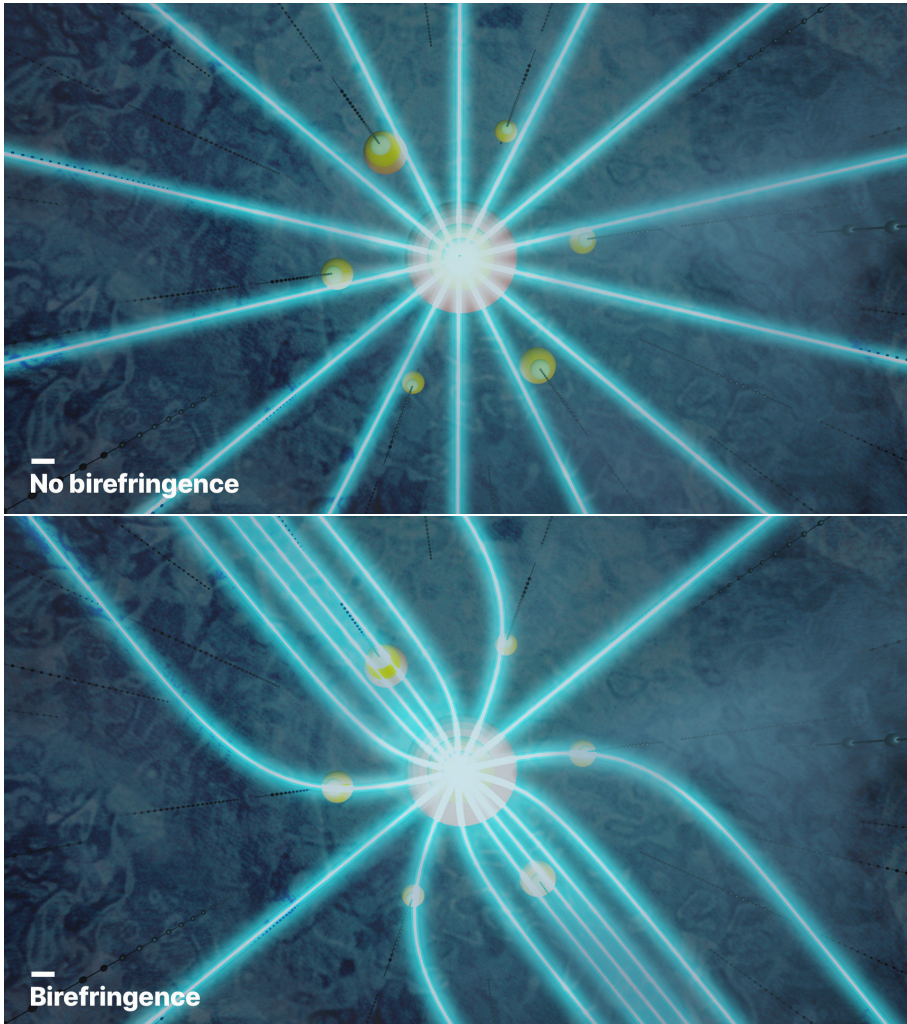


Figure 11.3: Artist depiction of the effect of birefringence, where light is slowly deflected towards the flow axis. As light travel outwards from the source in the birefringent ice, it becomes more likely to travel in the direction of the ice flow. [86]

12. Splines in IceCube

Spline functions, also called splines, are piecewise polynomials. They can be used for interpolation, approximation, and smoothing of functions. B-splines is short for basis splines. They are called such as they can be combined to construct any piecewise polynomial.

In our reconstruction, we approximate the light distribution using B-splines, that interpolate between points that have been simulated. At present, the splines we use for muon reconstruction are based on simulation without anisotropy. With the new understanding of anisotropy due to birefringence, it is time to update the splines to the latest ice model. This will require more complexity due to the additional dependence on the azimuthal direction, which was not included before.

In this chapter we will go over the mathematical formulation of B-splines, and bivariate splines which are a generalization of B-splines to arbitrary 2-dimensional geometries. They are investigated as directional dependence should be better modelled on a sphere instead of a rectangle.

12.1 B-splines

B-splines are defined on a set of intervals $[x_i, x_{i+1})$ as

$$B_{i,0}(x) = \begin{cases} 1 & x_i \leq x < x_{i+1} \\ 0 & \text{otherwise} \end{cases} \quad (12.1)$$

$$B_{i,n}(x) = \begin{cases} 0 & x_{i+n+1} = x_i \\ \frac{(x-x_i)}{x_{i+n}-x_i} B_{i,n-1}(x) + \frac{(x_{i+n+1}-x)}{x_{i+n+1}-x_{i+1}} B_{i+1,n-1}(x) & \text{otherwise} \end{cases} \quad (12.2)$$

$B_{i,n}$ is a base spline of order n . A spline function of order n on m intervals has full support on $m - 2n$ intervals. By adding extra intervals outside the region of interest, one can ensure full support. These extra intervals can be of 0 length. By giving each B-spline a suitable weight w_i , a function can be approximated by piecewise polynomials with $n-2$ continuous derivatives.

$$F(x) \approx \sum_i w_i B_{i,n}(x) \quad (12.3)$$

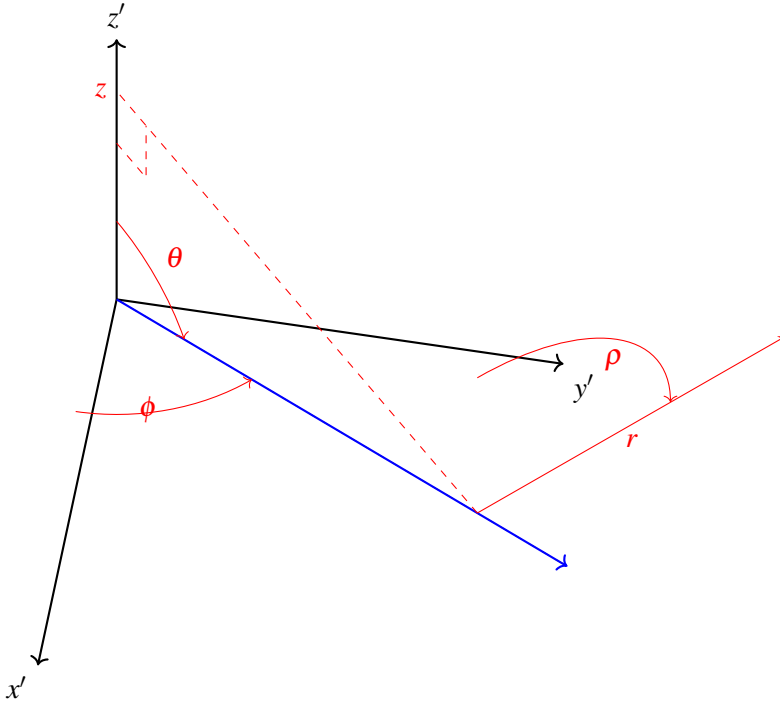


Figure 12.1: The coordinate system of IceCube track reconstruction splines. The thick blue line is the path of the muon track. Coordinates θ and ϕ give the direction of the muon, z gives the depth of the track at the point closest to the DOM, r gives the closest distance to the DOM and, ρ gives the angle to the DOM. The photon arrival time t is not shown. Until now, splines for muon track reconstruction have not included ϕ as no anisotropy was modelled.

It is quite straightforward to use tensor products of B-splines to expand the spline function into more dimensions

$$F(x, y) \approx \sum_i \sum_j w_{i,j} B_{i,n}(x) B_{j,n}(y) \quad (12.4)$$

12.2 B-splines in IceCube

Until now the splines tables used in IceCube muon reconstruction had 5 dimensions, see figure 12.1: depth z of the track at the point closest to the DOM, angle ρ from the track to the DOM, distance r of the track to the DOM, the zenith angle of the track θ and photon arrival time t ¹. There are 79 intervals in z , 28 intervals in ρ , 44 intervals in r , 35 intervals in t and 22 intervals in θ . To

¹Relative to the first possible arrival time

keep the problem feasible, weights are fitted for each z and θ independently. The weights for the splines are calculated by solving a system of least squares equations, minimizing the square of the discrepancy between simulated and predicted values,

$$F(\rho, r, t, z_m, \theta_n) - \sum_j \sum_k \sum_l w_{j,k,l,z_m,\theta_n} B_{j,2}(\rho) B_{k,2}(r) B_{l,3}(t) \quad (12.5)$$

where $F(\rho, r, t, z_m, \theta_n)$ is the photon arrival PDF, estimated from simulation. Note that second order splines are used for all dimensions except for t which uses a third order spline. θ_n are the set of zenith angles that are simulated. Each of these simulated tracks are propagated from $z = -900\text{m}$ to $z = 900\text{m}$ and the light distribution is binned in ρ , r , t and z .

Once these weights have been determined, splines are added to interpolate in z and θ creating a smooth function:

$$S(\rho, r, t, z, \theta) = \sum_j \sum_k \sum_l \sum_{z_m} \sum_{\theta_n} w_{j,k,l,z_m,\theta_n} B_{j,2}(\rho) B_{k,2}(r) B_{l,3}(t) B_{z_m,2}(z) B_{\theta_n,2}(\theta) \quad (12.6)$$

With the discovery of anisotropy in the ice, there has been a need to add azimuthal dependence to the model. A naive approach would be to add azimuth to the outer spline tables using a tensor product. This comes with several drawbacks. First, there would be oversampling at the poles which could waste computer resources (see figure 12.2). Second, a direction close to a pole would only use splines close in ϕ , even when splines far away in ϕ could have a small space angle difference. These problems motivate a different kind of spline which respects the geometry of the sphere.

12.3 Bivariate Splines and D1RC splines

An alternative interpolation scheme is bivariate splines, which is a generalization of B-splines to two dimensions. While there are several constructions of bivariate splines, the construction that was investigated was Directed One Ring Cycle (D1RC) splines. For a formal presentation, see [94]. D1RC splines can be defined on any triangulated surface. This allows evenly spaced knot locations (see figure 12.3) and also oversampled regions.

D1RC splines are defined in a triangulation in the plane. We will start off with how they are defined and then show how this can be generalized to a surface in three dimensions and finally how we create D1RC splines for light amplitude (expected number of photons) from muon tracks in IceCube. Amplitude splines have one less dimension, allowing faster fitting and evaluation when comparing to B-splines.

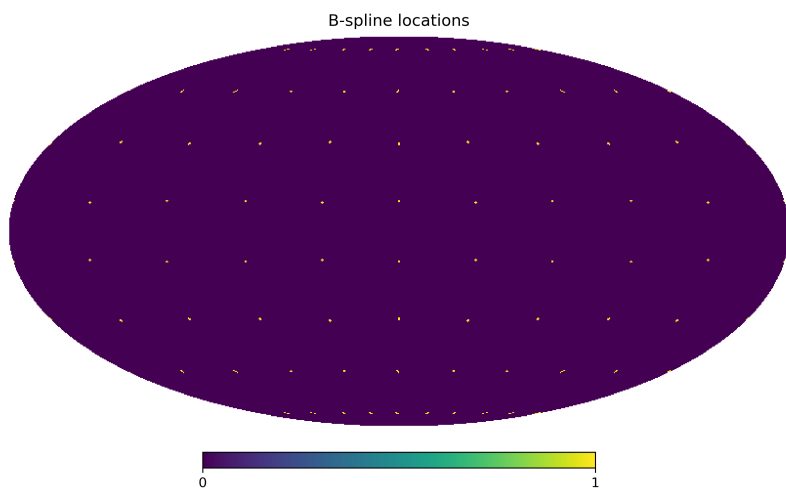


Figure 12.2: Example of spline locations for B-splines.

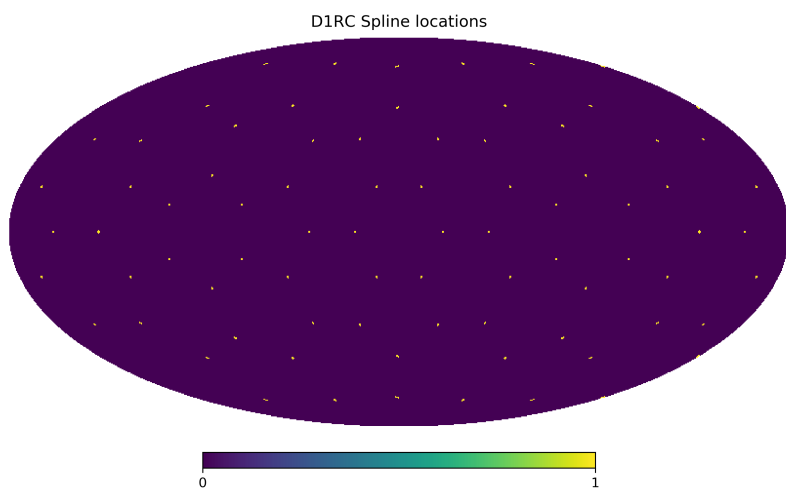


Figure 12.3: Example of spline locations for bivariate splines.

12.4 Mathematical Definition of D1RC Splines

12.4.1 Barycentric Coordinates

For two-dimensional variables v, w, u forming the triangle W , define

$$d(v, w, u) = \begin{vmatrix} 1 & 1 & 1 \\ v1 & w1 & u1 \\ v2 & w2 & u2 \end{vmatrix}$$

Then λ_i defined as

$$(\lambda_1(x|W), \lambda_2(x|W), \lambda_3(x|W)) = \frac{(d(x, w, u), d(v, x, u), d(v, w, x))}{d(v, w, u)}$$

are the barycentric coordinates of x in relation to the triangle v, w, u . These coordinates have properties such as $\lambda_1 + \lambda_2 + \lambda_3 = 1$, $v\lambda_1 + w\lambda_2 + u\lambda_3 = x$, $\lambda_i \geq 0$ if x is in the triangle W and are only 0 at the boundary of the triangle. The barycentric coordinate λ_i can be thought of the fractional height above the edge opposite to corner i , so that λ_i has value 1 on the corner and 0 on the opposite edge. This is analogous to the $\frac{x-x_i}{x_{i+n}-x_i}$ term when using B-splines.

12.4.2 Simplex Spline

Notice that simplex splines are not defined on triangulations, but on sets of control points in two dimensions. These are the building blocks of the Directed One Ring Cycle (D1RC) splines, which are defined on a triangulation and use the vertices as control points of the simplex splines.

A simplex spline of order 0, M_0 , is defined on a set U of three vertices forming a triangle W :

$$M_0(x|U) = \begin{cases} 1 & x \text{ in the triangle } W \\ 0 & \text{otherwise} \end{cases} \quad (12.7)$$

A simplex spline of order k M_k , is defined on a set of control points U of size $k+3$ as

$$M_k(x|U) = \sum_{j=1}^{j=3} \lambda_j(x|W) M_{k-1}(x|U \setminus \{t_{i_j}\})$$

choosing three random vertices $\{t_{i_1}, t_{i_2}, t_{i_3}\}$, forming a triangle W . The choice of vertices does not matter as long as they are not in a line.

12.4.3 D1RC Splines

From the simplex splines, we can define our bivariate splines. D1RC splines of order k need a set U of $k + 1$ control points and sorted set X_U of all neighbours. So given a triangulation, an order 0 set U would just be a vertex, an order 1 would be two vertexes connected by an edge and an order 2 would be three adjacent vertexes making a triangle. The set X_U would contain any vertex not in U , connected by an edge to a vertex in U . $X_U = \{v_1 \dots v_n\}$ is sorted, so that v_i is connected to v_{i+1} and v_1 is connected to v_n .

For a set of control points U of size $k + 1$ and n sorted neighbour vertices $X_U = \{v_1 \dots v_n\}$, we define the D1RC spline as

$$b_k(x|U) = \sum_{i=1}^n d(v_i, v_{i+1}, x) M_k(x|U \cup \{v_i, v_{i+1}\})$$

We will be using second order D1RC splines to have differentiable derivatives. This means that each spline will be defined on a triangle and all neighbouring vertices. We will call this set of vertices a vertex base U . Now given a triangulation we can create a set of vertex bases U_i and fit corresponding weights α_i to create our spline function

$$S(x) = \frac{\sum_i \alpha_i b_2(x|U_i)}{\sum_i b_2(x|U_i)}$$

By fitting the weights we can approximate any function F defined in the plane

$$F(x) \approx S(x) \tag{12.8}$$

12.5 Coordinate System

Our bivariate splines are defined on a triangulation of a plane. To lift this into a spherical configuration, we have a different coordinate system for each basis, which we will define to be the projection from the centre of a sphere to the plane defined by the triangle that is at the centre of a second order D1RC spline. This is an analytical transformation and does not impact the twice differentiable nature of the splines. We refer to the coordinates in this plane as x_i , where i enumerates the different bases.

There is one more problem that arises from the coordinate system that needs to be solved. As can be seen in figure 12.1 the direction of \mathbf{r} , the perpendicular displacement of the DOM from the track, changes as ϕ changes. Close to the poles a small change in direction can give a very different ϕ , so when one uses spline PDFs derived for a track direction $\hat{\mathbf{t}}_s$ in order to interpolate to

a track with direction close to $\hat{\mathbf{t}}_s$, the same ρ and r may correspond to very different \mathbf{r} -vectors, \mathbf{r}_s and \mathbf{r}_t , for the "spline track" at $\hat{\mathbf{t}}_s$ and the track interpolated to. This can be handled by modifying the values of ρ and z used for the spline track so as to make its \mathbf{r} -vector, \mathbf{r}_s as close as possible to the wanted vector \mathbf{r}_t , by choosing

$$\mathbf{r}_s = |\mathbf{r}_t| \frac{\mathbf{r}_t - \hat{\mathbf{t}}_s(\hat{\mathbf{t}}_s \cdot \mathbf{r}_t)}{|\mathbf{r}_t - \hat{\mathbf{t}}_s(\hat{\mathbf{t}}_s \cdot \mathbf{r}_t)|} \quad (12.9)$$

and calculating the corresponding ρ_s . The z -coordinate of the spline track can then be set so that the depth of the DOM is unchanged, by choosing

$$z_s = z + (\mathbf{r}_t \cdot \hat{\mathbf{z}} - \mathbf{r}_s \cdot \hat{\mathbf{z}}) \quad (12.10)$$

where z_s is the z -value for the track being interpolated to. During interpolation, each spline that contributes will have its own z_s and ρ_s values as defined as above. As for x_i , we will index these transforms as ρ_i and z_i , where i relates to the direction represented by the spline.

12.6 Building the D1RC Spline

Previously, we have fitted weights for each track direction θ and depth z independently. But as we are now working with the total light yield we do not have a time dimension so we can add z to the least square fit. For our triangulation of the sphere, with a set of triangles W_i , we simulate a track direction at the centre of gravity of each triangle and for each track we fit B-splines in three dimensions to the light yield $F_i(z, \rho, r)$ estimated by the simulation

$$S_i(z, \rho, r) = \sum_j \sum_k \sum_l \alpha_{i,j,k,l} B_{j,2}(z) B_{k,2}(\rho) B_{l,2}(r) \quad (12.11)$$

$$F_i(z, \rho, r) \approx S_i(z, \rho, r) \quad (12.12)$$

We can now add the neighbours to each triangle to get a set of vertex bases U_i and interpolate using D1RC splines

$$S(\theta, \phi, z, \rho, r) = \frac{\sum_i b_2(x_i(\theta, \phi)) |U_i| S_i(z_i(\theta, \phi, z, \rho, r), \rho_i(\theta, \phi, \rho, r), r)}{\sum_i b_2(x_i(\theta, \phi)) |U_i|} \quad (12.13)$$

12.7 Results and Comparison

Having constructed D1RC splines, they were fitted to simulation of light yield and compared to a validation simulation set. At the same time, a tensor product construction of B-splines was fitted as well. These two were compared on how well they described the validation data. A slice of this comparison can be seen in figure 12.4. As D1RC splines showed no improvement on tensor product B-splines, it was decided to go ahead and make new splines using the old method to keep complexity of the code base to grow for no gain.

Next the time distributions was fitted using the B-spline method which was able to fit the validation data much better than previous splines, see figure 12.5.

To look for an improvement in reconstruction, a first test using simulation was conducted¹. Here the true track and photon arrival time is used, but this simulation contains systematic uncertainties and all possible interaction, not only Cherenkov light. It was expected that the new splines would describe the light distribution better than the current splines, but to test this is not that straight forward, as the time PDF depends on many parameters. A way to compare two families of distributions is to look in the CDF dimension. Any distribution expects a Δt fraction of outcomes to be between the CDF values of t and $t + \Delta t$. That would equal 1 in a normalized histogram. By looking at values in CDF space, we can put evaluations from many distributions in the same plot.

In figure 12.6, we have a histogram of the cumulative time distribution function of photons hitting the detectors for currently used and new spline tables. We can see that the new splines are able to describe the early arriving photons better, as the histogram is closer to one. The current splines have overestimated the number early photons, as the histogram is lower than one.

This can also be seen in plot 12.7 which shows a histogram of the delta log likelihood values using both MPE and SPE likelihoods. As MPE relies more on early photons, it has improved more with the new splines.

¹For internal reference, dataset 22311 was used.

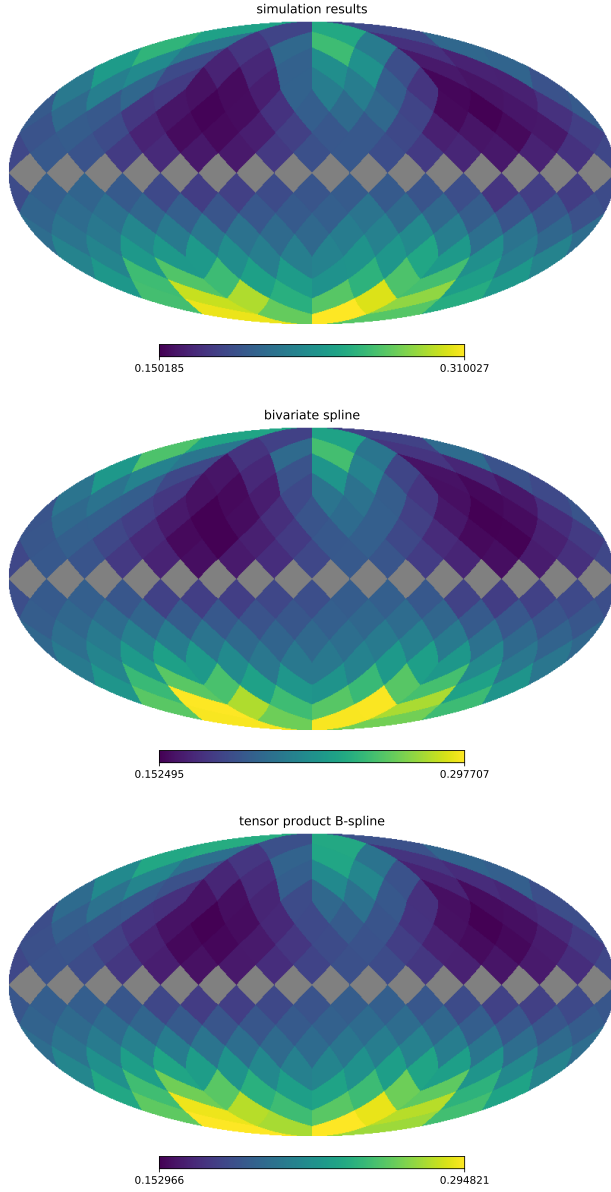


Figure 12.4: Healpix [95] plots of light yield for different track directions. Fixed parameters are $z = -290\text{m}$, $\rho = 23^\circ$ and $r = 73\text{m}$. Here, D1RC shows no advantage over tensor products of B-splines. The values are the expected number of photons given a muon with only Cherenkov radiation travelling at the speed of light.

Time PDF $z = -190.00$ $\rho = 1.66$ zenith = 131.81 azimuth = 202.50 $r = 95.1$

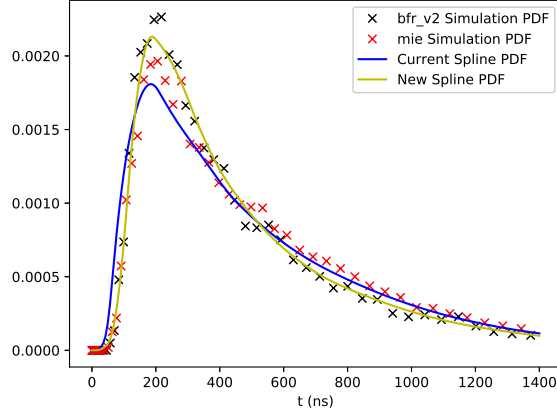


Figure 12.5: Validation of the time PDF and comparison with the current splines. The current splines are meant to predict the bfr_v2 simulation, which is the latest ice model not containing tilt. The current splines are meant to predict the mie simulation. One can see that the currently used splines expect photons to arrive earlier, while the new splines have a good description of the bfr_v2 simulation

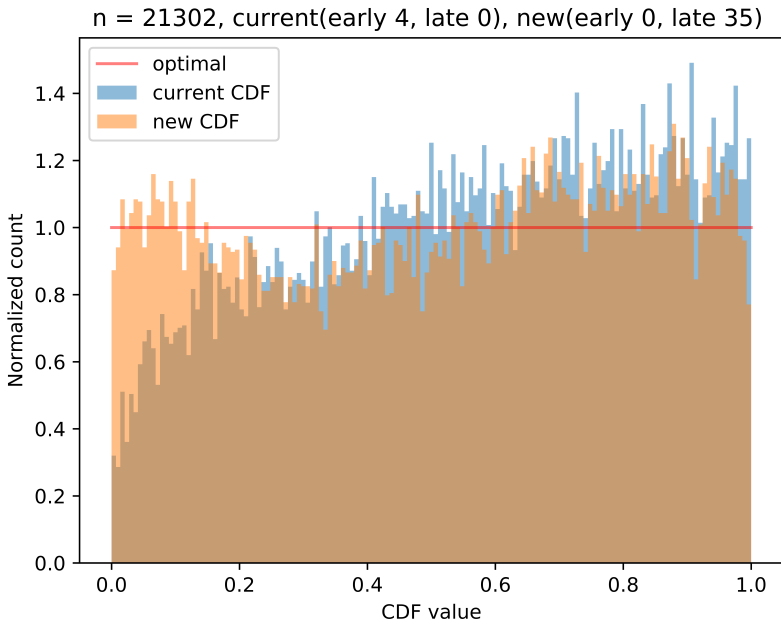


Figure 12.6: Normalized histogram of the CDF values for photon times from a simulation of realistic muons at a distance from 20 to 40 metres from the muon track. At the top the total number of photons (n) and the number that has been evaluated to having 0 likelihood is listed, either it happens before CDF rises (early) or after the CDF reaches 1 (late). Here 4 out of 21302 photons arrived earlier than the current splines predicted and 35 later than the new splines predicted.

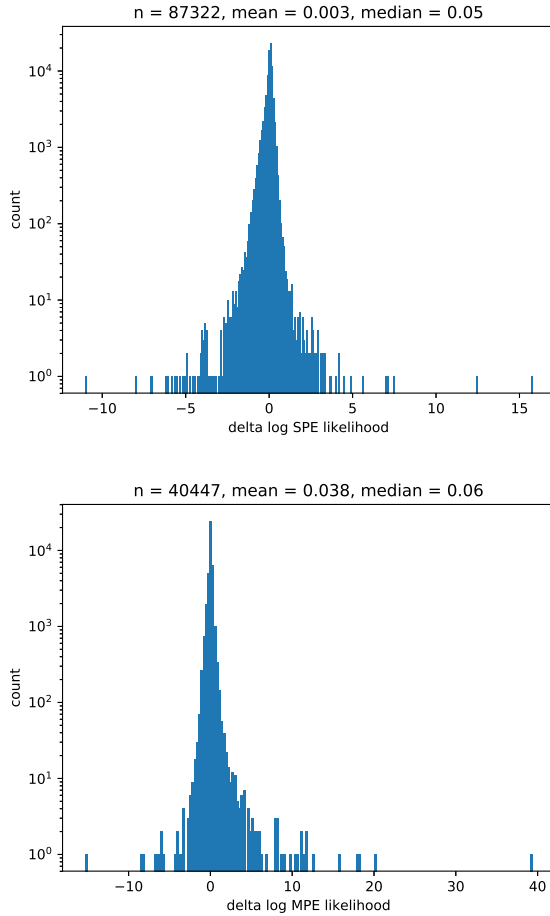


Figure 12.7: Histogram of the log likelihoods of the new splines minus the likelihood of the old splines. The top plot shows the delta log likelihood using the SPE likelihood and the bottom one using the MPE likelihood. n is the number of evaluations of the likelihoods, which for MPE is once per DOM and track, while for SPE it is once per photon. Both plots show an improvement with the new splines, but the MPE likelihood has the largest change with twelve times larger average improvement.

13. Summary and Future Work

In summary, I have created the first in-situ geometry calibration in IceCube with uncertainties smaller than measured deviations from nominal position. It currently works in the central parts of the detector. The results have been confirmed by a later method, which has larger statistical uncertainties and only works for string averages, but works throughout the entire detector. The understanding of the optical properties of the ice has improved recently, and given the significance of the time probability density functions (PDFs) in the reconstruction process, new PDFs have been developed. The updated splines model the effect of the anisotropy in the ice and give a slight improvement in describing light propagation in simulated data.

In this chapter, I discuss some of the interesting findings and possibilities for further improvement.

13.1 Systematic Errors in Position Calibration

We can see in figure 9.4, 10.1, and 10.2 that we have large effects at the edge of the detector. These can also be seen for edge DOMs in figure 10.3 and 10.4. These are unphysical shifts, as the drill hole should be close to vertical. Two possible causes for these are mismodelling and bias of the estimator. Could a less biased estimator be constructed? It is known that maximum likelihood estimators are consistent but often biased estimators, so it is possible that these effects will shrink with more data. But we can look for a likelihood that is more suitable for the edge of the detector, where the problem is less symmetric. One idea is to include the Poisson likelihood for the number of photons detected. This could for example give corner DOMs a push outwards because of tracks for which they detect no photons. But having to include tracks with 0 photon hits would entail a large computational cost, because it would require all tracks in the sample to be evaluated for every DOM position calibration.

Some mismodelling is addressed in chapters 11 and 12, but there is a second way we can reduce mismodelling. The geometry calibration is sensitive to the entire PDF as it uses the SPE likelihood and modelling the tail correctly can be very hard as modelling errors will accumulate the longer a photon propagates. Changing to MPE, which only uses the deposited charge and the first

photon arrival time (see section 6.4), would make it less reliant on the late part of the distribution which is harder to model. While the formulation of MPE contains an integral, it is fast to evaluate, as the splines are saved as the CDF.

13.2 Statistics

I have used 12 days of data in my analysis. The reason for this is that I wanted to complete any DOM position fit within two days, as limited by the IceCube cluster in Madison. This limits the number of events to about 2 million. It seems like the results are statistics limited and statistics could be increased in three different ways. The naive approach would be to require more computing power. Alternatively, one could try to optimize the code allowing processing more statistics in two days. Lastly one could, instead of using a set time interval, collect tracks until each DOM has 2 million tracks.

13.3 Regularization

The drill is guided by gravity, and we only expect small deviations from vertical. As the DOMs are 17m apart, we do not expect large horizontal deviation between two neighbouring DOMs. By adding a dependency on adjacent DOMs local statistics could be improved. It was not done here as it could hide problems with the method and not help with understanding. This topic will be revisited if and when it is decided to use this method for individual DOM position calibration.

13.4 Dust Layer Effects

We can see two features in the Dust layer. In z we see that the dust layer gives a different effect in data than in simulation, see figure 10.1 and 10.2 compared to 9.5. Data/simulation disagreements are always of interest as they may tell us something we have missed regarding our detector. Secondly, it seems like the localization in x and y is no worse in the dust layer, despite having only a fraction of the events compared to other depths. This hints towards there being a subset of events which is more useful in this analysis. It could also be that we are just better at modelling the dust layer, but this is considered a less likely scenario. One plausible scenario is that the photons in the dust layer do not travel very far before getting absorbed and the longer a photon exists the larger the modelling error becomes.

13.5 Individual DOM calibration

From figure 10.15, it seems likely that string 44 is better modelled by individual DOM positions instead of a single string average. In general, the muon method has been validated by the flasher method, which should give us some confidence in the individual DOM positions.

13.6 Optimizing time knots

Currently, the new spline tables are saved in residual time, defined by 0 being the earliest possible time for light to arrive given the speed of light in the ice. Time knots are densest close to 0 as at short distances the features are very sharp. If a slower speed were used to define the residual time, the light curves at longer ranges would be moved to regions where there are more knots and which would allow a better modelling.

13.7 Integration of new splines

Now that there are new splines for the birefringent ice and an established procedure to update them, the next step is to update the reconstruction code to interface with the new spline tables.

13.8 Study the impact

While both the calibration and updated reconstruction will give better pointing, a study should be done to estimate the impact. There are different kinds of impacts to study. First and most obvious would be to estimate our new sensitivity, but also investigating if our systematic uncertainty has been under- or overestimated and how that has impacted our previously reported sensitivity. A less obvious effect could be an impact on reported spectral indexes. As could be seen in section 7.4, geometry has a larger impact on higher energy tracks. This could cause high energy tracks to contribute less in point source searches, which will overestimate the spectral index. For example, for NGC1068 the fitted spectral index is 3.2 [59], which is above the spectral index measured for the diffuse flux single power law fit of 2.5 [96].

13.9 Beyond Splines

While splines currently provide the best photon arrival time PDFs we have for muon track likelihood reconstructions, neural networks may be used in the

future for estimating these PDFs. This has been done for cascades [97] and is one of the improvements that led to the evidence of neutrino emissions in the galactic plane [56].

A. More plots on comparison
between geometry calibration
methods

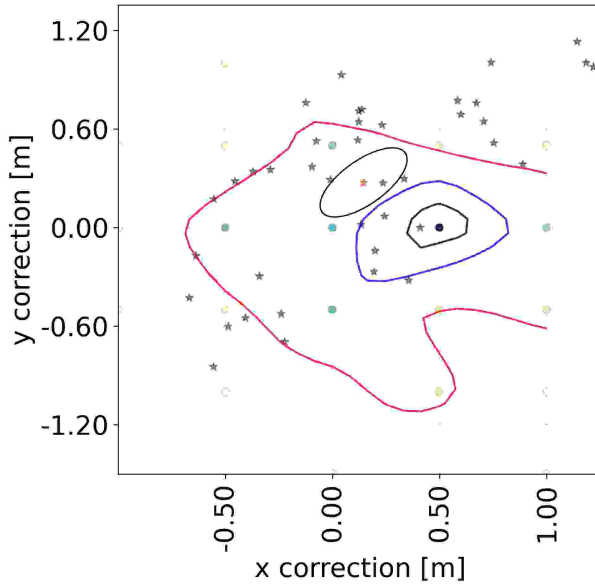


Figure A.1: Flasher and muon method results on string 25. See figure 10.11 for a detailed description.

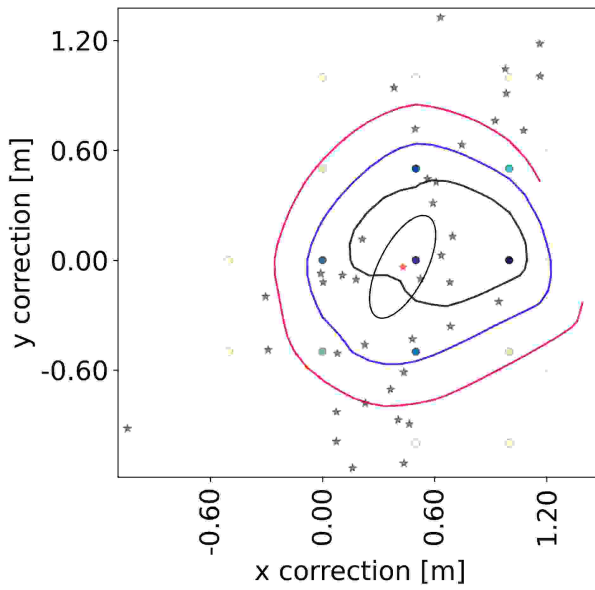


Figure A.2: Flasher and muon method results on string 26. See figure 10.11 for a detailed description.

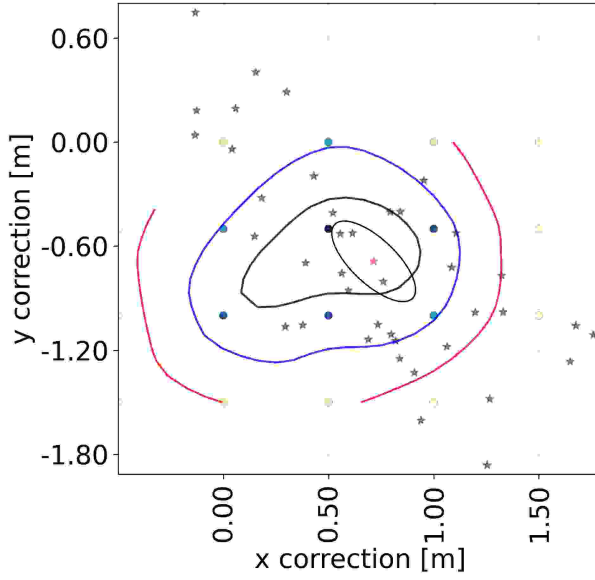


Figure A.3: Flasher and muon method results on string 27. See figure 10.11 for a detailed description.

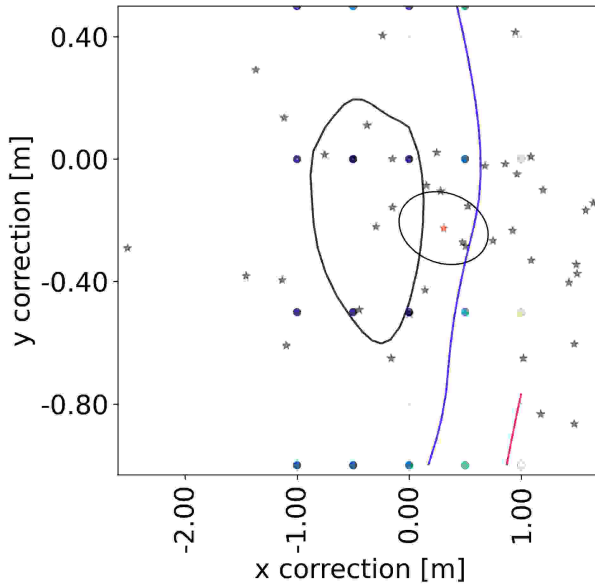


Figure A.4: Flasher and muon method results on string 37. See figure 10.11 for a detailed description.

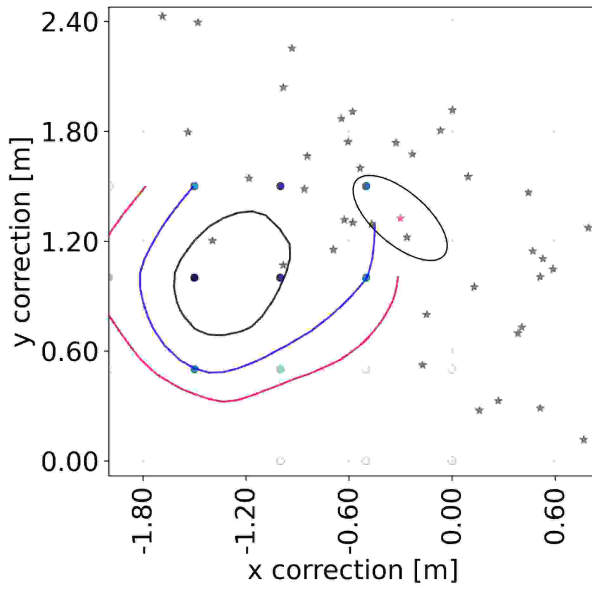


Figure A.5: Flasher and muon method results on string 45. See figure 10.11 for a detailed description.

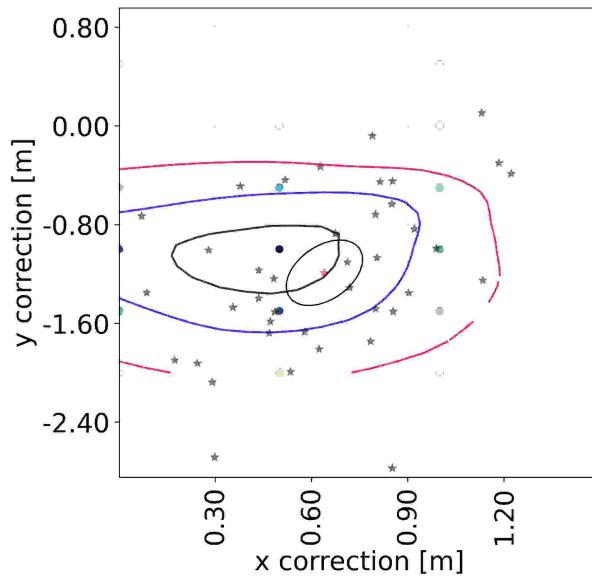


Figure A.6: Flasher and muon method results on string 46. See figure 10.11 for a detailed description.

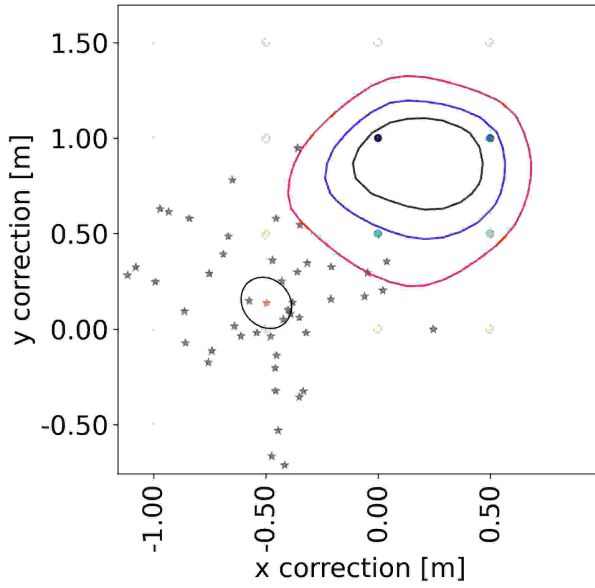


Figure A.7: Flasher and muon method results on string 79. See figure 10.11 for a detailed description.

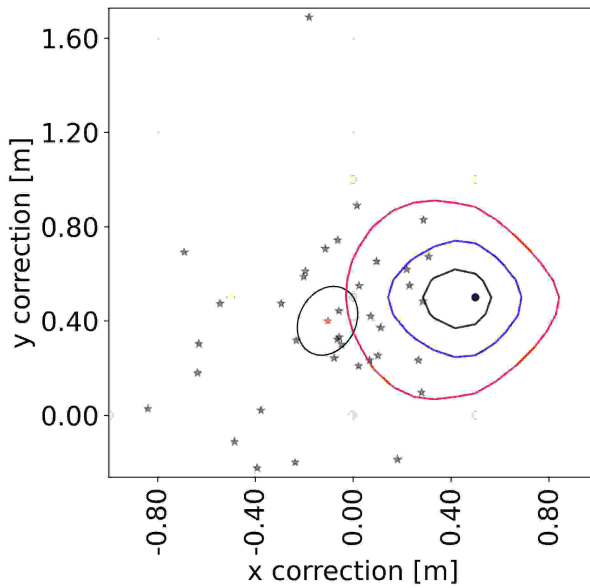


Figure A.8: Flasher and muon method results on string 80. See figure 10.11 for a detailed description.

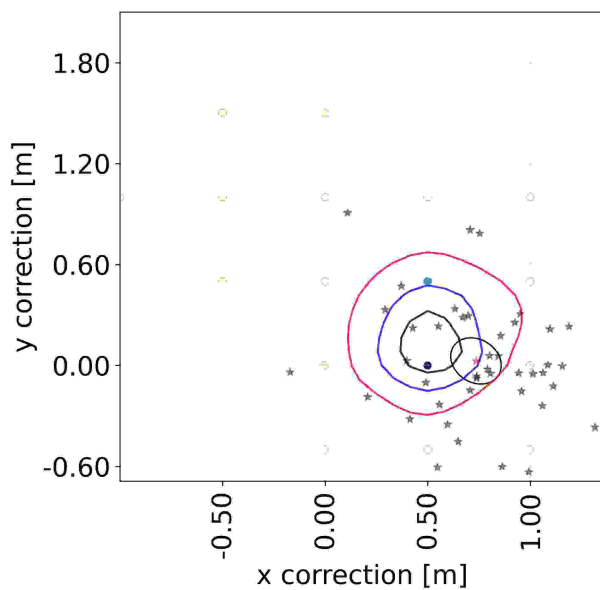


Figure A.9: Flasher and muon method results on string 81. See figure 10.11 for a detailed description.

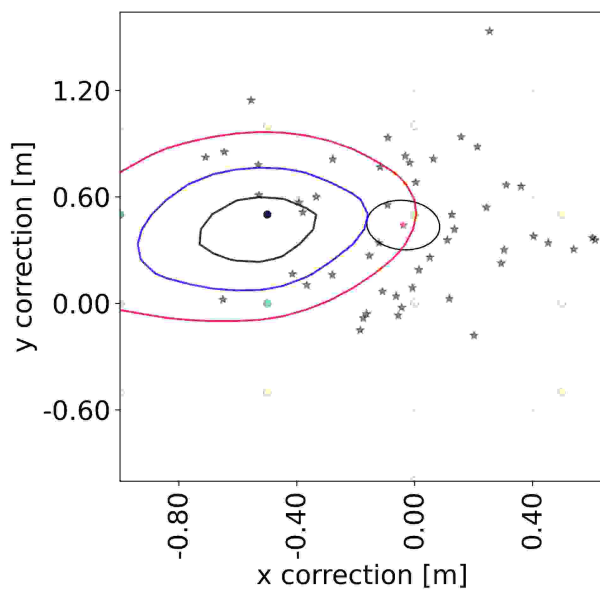


Figure A.10: Flasher and muon method results on string 82. See figure 10.11 for a detailed description.

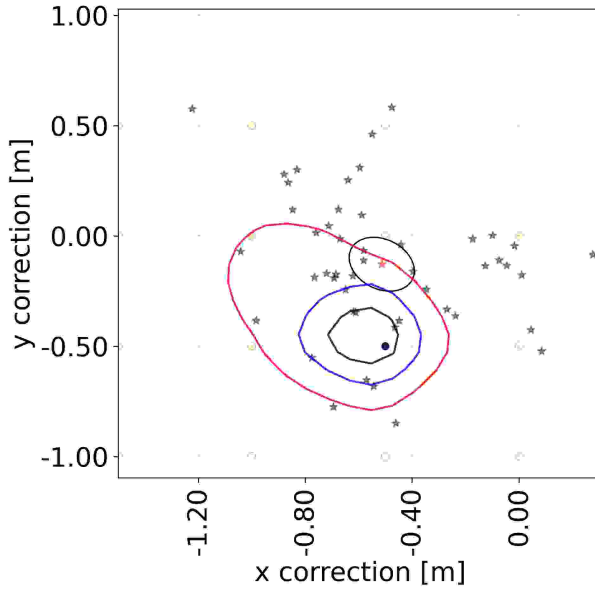


Figure A.11: Flasher and muon method results on string 83. See figure 10.11 for a detailed description.

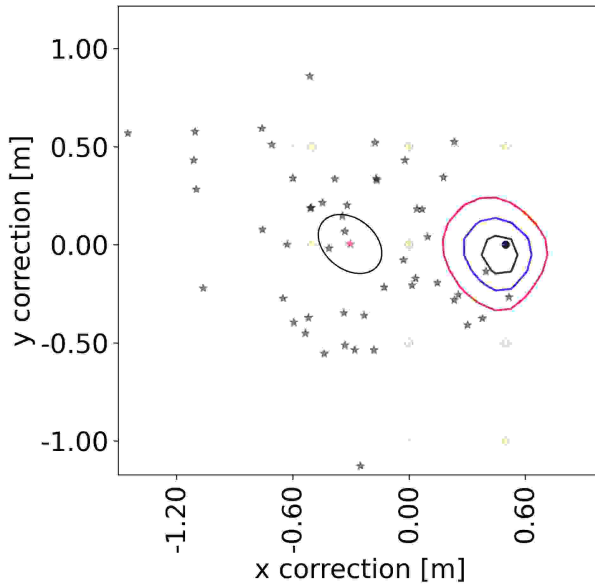


Figure A.12: Flasher and muon method results on string 84. See figure 10.11 for a detailed description.

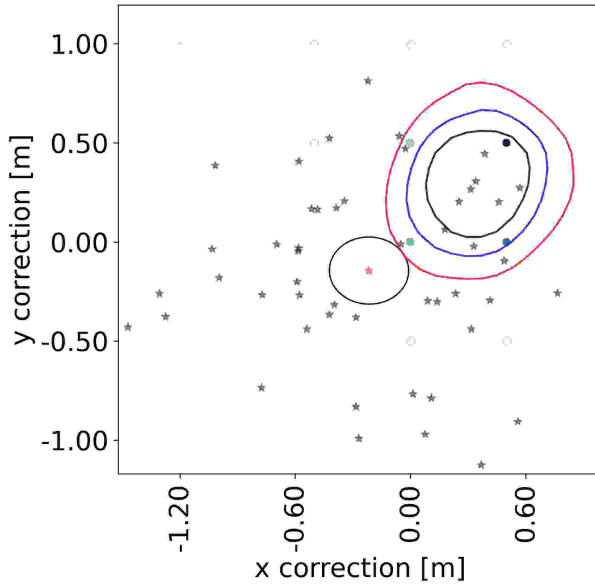


Figure A.13: Flasher and muon method results on string 85. See figure 10.11 for a detailed description.

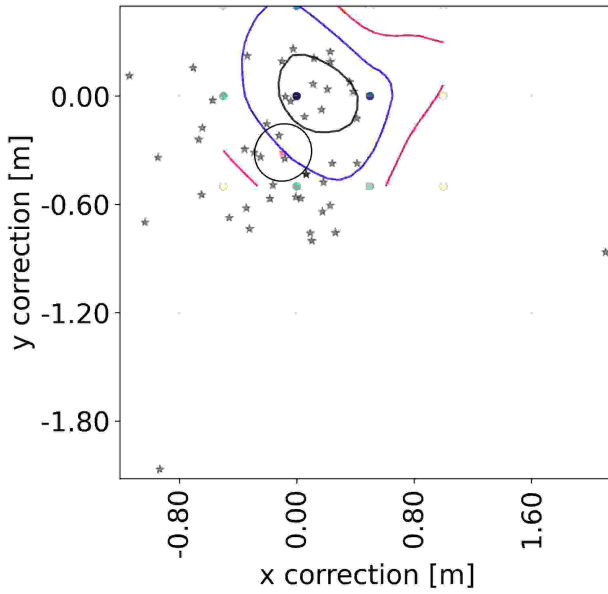


Figure A.14: Flasher and muon method results on string 86. See figure 10.11 for a detailed description.

References

- [1] ICECUBE COLLABORATION, MATTI JANSSON, MARTIN RONGEN, AND SASKIA PHILIPPEN. Refining the IceCube detector geometry using muon and LED calibration data. *PoS, ICRC2023*:988, 2023. v, 88
- [2] JÖRG P. RACHEN. Origin of ultra-high energy cosmic rays: The cosmological manifesto. 2019. 15
- [3] FRANCIS HALZEN AND DAN HOOPER. High-energy neutrino astronomy: the cosmic ray connection. *Reports on Progress in Physics*, **65**(7):1025–1078, jun 2002. 15
- [4] M. G. AARTSEN ET AL. The IceCube Neutrino Observatory: Instrumentation and Online Systems. *JINST*, **12**(03):P03012, 2017. 15, 25, 26, 31, 32, 33, 34, 35, 37, 38, 39, 40, 41, 42, 54
- [5] MARTIN RONGEN. *Calibration of the IceCube Neutrino Observatory*. Other thesis, 11 2019. 15
- [6] MATT NEWCOMB. Drill geometry data. https://user-web.icecube.wisc.edu/~mrongen/drill_geom/geom_browser.html. 2011. 15
- [7] LILLY PETERS. How uncertainties of the geometry calibration affect the directional reconstruction. https://drive.google.com/file/d/1nonDSKILR0Rq_y0-Hiuc_muE5KVZTS0/view. 2019. 15, 53
- [8] DAVID BOERSMA. Filter Proposal for Moon & Sun Shadow Analysis IC86-2013. 2012. 15, 35
- [9] VICTOR F. HESS. Über Beobachtungen der durchdringenden Strahlung bei sieben Freiballonfahrten. *Phys. Z.*, **13**:1084–1091, 1912. 19
- [10] STEFAN WESTERHOFF. Ultra-high-energy cosmic rays. *Int. J. Mod. Phys. A*, **21**:1950–1961, 2006. 19
- [11] E. LORENZ, ROBERT WAGNER, AND R. WAGNER. Very-high energy gamma-ray astronomy: A 23-year success story in high-energy astroparticle physics. *Eur. Phys. J. H*, **37**:459–513, 2012. 19
- [12] LUIS A. ANCHORDOQUI ET AL. Roadmap for Ultra-High Energy Cosmic Ray Physics and Astronomy (whitepaper for Snowmass 2013). In *Community Summer Study 2013: Snowmass on the Mississippi*, 7 2013. 19
- [13] D. BOSE, V. R. CHITNIS, P. MAJUMDAR, AND B. S. ACHARYA. Ground-based gamma-ray astronomy: history and development of techniques. *Eur. Phys. J. ST*, **231**(1):3–26, 2022. 19
- [14] KLAUS PINKAU. History of gamma-ray telescopes and astronomy. *Experimental Astronomy*, **25**, 2009. 19
- [15] P. PICOZZA AND A. MORSELLI. The science of PAMELA space mission. In *12th Lomonosov Conference on Elementary Particle Physics*, pages 96–103, 4 2006. 19
- [16] H. O. KLAGES ET AL. The KASCADE Experiment. *Nuclear Physics B (Prox Suppl.)*, **52B**:92–102, 1997. 19

- [17] K. MITSUDA ET AL. The X-Ray Observatory Suzaku. *Astronomical Society of Japan*, **59**, 2007. 19
- [18] M. C. WEISSKOPF, H. D. TANANBAUM, L. P. VAN SPEYBROECK, AND S. L. O'DELL. Chandra x-ray observatory (cxo):overview. *Proc. SPIE Int. Soc. Opt. Eng.*, **4012**:2, 2000. 19
- [19] W. B. ATWOOD ET AL. The Large Area Telescope on the Fermi Gamma-ray Space Telescope Mission. *Astrophys. J.*, **697**:1071–1102, 2009. 19
- [20] VLADIMIR VASSILIEV, P. F. BROUSSEAU, AND S. J. FEGAN. Wide field Ritchey-Chretien telescope for ground-based gamma-ray astronomy. *Astropart. Phys.*, **28**:10–27, 2007. 19
- [21] H. BLOOD, J. LEARNED, F. REINES, AND A. ROBERTS. DUMAND: The Ocean as a Neutrino Detector. In *International Neutrino Conference 1976*, pages 688–702, 6 1976. 19
- [22] CHRISTIAN SPIERING. Towards High-Energy Neutrino Astronomy. A Historical Review. *Eur. Phys. J. H*, **37**:515–565, 2012. 19
- [23] PARTICLE DATA GROUP ET AL. Review of Particle Physics. *Progress of Theoretical and Experimental Physics*, **2020**(8), 08 2020. 083C01. 20, 23, 24
- [24] ATHANASIOS PAPAIOANNOU. Cosmic rays – messengers from space. <https://blogs.egu.eu/divisions/st/2018/03/19/cosmic-rays-messengers-from-space/>. 2018. 21
- [25] MARIUS POTGIETER. Solar modulation of cosmic rays. *Living Reviews in Solar Physics*, **10**, 2013. 19
- [26] A. M. BYKOV, D. C. ELLISON, A. MARCOWITH, AND S. M. OSIPOV. Cosmic ray production in supernovae. *Space Science Reviews*, **214**(1), jan 2018. 19
- [27] M. KACHELRIESS AND D.V. SEMIKOZ. Cosmic ray models. *Progress in Particle and Nuclear Physics*, **109**:103710, 2019. 19
- [28] KENNETH GREISEN. End to the cosmic ray spectrum? *Phys. Rev. Lett.*, **16**:748–750, 1966. 19
- [29] G. T. ZATSEPIN AND V. A. KUZMIN. Upper limit of the spectrum of cosmic rays. *JETP Lett.*, **4**:78–80, 1966. 19
- [30] M. G. AARTSEN ET AL. Astrophysical neutrinos and cosmic rays observed by IceCube. *Adv. Space Res.*, **62**:2902–2930, 2018. 22
- [31] ENRICO FERMI. On the Origin of the Cosmic Radiation. *Phys. Rev.*, **75**:1169–1174, 1949. 19
- [32] G. GUILLIAN ET AL. Observation of the anisotropy of 10-TeV primary cosmic ray nuclei flux with the super-kamiokande-I detector. *Phys. Rev. D*, **75**:062003, 2007. 20
- [33] R. U. ABBASI ET AL. Search for Large-scale Anisotropy on Arrival Directions of Ultra-high-energy Cosmic Rays Observed with the Telescope Array Experiment. *Astrophys. J. Lett.*, **898**(2):L28, 2020. 20
- [34] M. G. AARTSEN ET AL. Time-integrated neutrino source searches with 10 years of IceCube data. *Physical Review Letters*, **124**(5), feb 2020. 23, 27
- [35] P. A. CERENKOV. Visible radiation produced by electrons moving in a medium with velocities exceeding that of light. *Phys. Rev.*, **52**:378–379, 1937. 23
- [36] MARY K. GAILLARD, PAUL D. GRANNIS, AND FRANK J. SCIULLI. The standard model of particle physics. *Reviews of Modern Physics*, **71**(2):S96–S111, mar 1999. 23
- [37] PETER W. HIGGS. Broken symmetries and the masses of gauge bosons. *Phys. Rev. Lett.*, **13**:508–509, Oct 1964. 23

- [38] F. ENGLERT AND R. BROUT. Broken symmetry and the mass of gauge vector mesons. *Phys. Rev. Lett.*, **13**:321–323, Aug 1964. 23
- [39] GEORGES AAD ET AL. Observation of a new particle in the search for the Standard Model Higgs boson with the ATLAS detector at the LHC. *Phys. Lett. B*, **716**:1–29, 2012. 23
- [40] S. CHATRCHYAN ET AL. Observation of a new boson at a mass of 125 GeV with the CMS experiment at the LHC. *Physics Letters B*, **716**(1):30–61, sep 2012. 23
- [41] FRANCIS HALZEN. Lectures on neutrino astronomy: Theory and experiment. In *Theoretical Advanced Study Institute in Elementary Particle Physics (TASI 98): Neutrinos in Physics and Astrophysics: From 10^{-33} to 10^{28} cm*, 10 1998. 24
- [42] FABRIZIO NICASTRO, SMITA MATHUR, AND MARTIN ELVIS. Missing baryons and the warm-hot intergalactic medium. *Science*, **319**(5859):55–57, jan 2008. 24
- [43] M. G. AARTSEN ET AL. First observation of PeV-energy neutrinos with IceCube. *Phys. Rev. Lett.*, **111**:021103, 2013. 24
- [44] M. A. MARKOV. On high energy neutrino physics. In *10th International Conference on High Energy Physics*, 1960. 24
- [45] M. G. AARTSEN ET AL. Evidence for High-Energy Extraterrestrial Neutrinos at the IceCube Detector. *Science*, **342**:1242856, 2013. 24
- [46] M. G. AARTSEN ET AL. Observation of high-energy astrophysical neutrinos in three years of icecube data. *Phys. Rev. Lett.*, **113**:101101, Sep 2014. 24
- [47] EVANGELIA DRAKOPOULOU. Km3net: Status and physics results. *Nuclear Instruments and Methods in Physics Research Section A: Accelerators, Spectrometers, Detectors and Associated Equipment*, **1056**:168592, 2023. 25
- [48] RASTISLAV DVORNICKY. Large neutrino telescope baikal-gvd: recent status. In *Proceedings of 38th International Cosmic Ray Conference — PoS(ICRC2023)*, ICRC2023. Sissa Medialab, August 2023. 25
- [49] MATTEO AGOSTINI ET AL. The Pacific Ocean Neutrino Experiment. *Nature Astron.*, **4**(10):913–915, 2020. 25
- [50] CHRISTIAN SPANNFELLNER. Design of the Pacific Ocean Neutrino Experiment’s First Detector Line. *PoS*, **ICRC2023**:1219, 2023. 25
- [51] M. G. AARTSEN ET AL. Time-Integrated Neutrino Source Searches with 10 Years of IceCube Data. *Phys. Rev. Lett.*, **124**(5):051103, 2020. 25
- [52] THOMAS K. GAISSER. Spectrum of cosmic-ray nucleons, kaon production, and the atmospheric muon charge ratio. *Astropart. Phys.*, **35**:801–806, 2012. 25
- [53] M. G. AARTSEN ET AL. A combined maximum-likelihood analysis of the high-energy astrophysical neutrino flux measured with IceCube. *Astrophys. J.*, **809**(1):98, 2015. 25
- [54] HANS NIEDERHAUSEN. *Measurement of the High Energy Astrophysical Neutrino Flux Using Electron and Tau Neutrinos Observed in Four Years of IceCube Data*. PhD thesis, Stony Brook University, 2018. 26
- [55] R. ABBASI ET AL. IceTop: The surface component of IceCube. *Nucl. Instrum. Meth. A*, **700**:188–220, 2013. 26
- [56] R. ABBASI ET AL. Observation of high-energy neutrinos from the Galactic plane. *Science*, **380**(6652):adc9818, 2023. 27, 118

- [57] MARK AARTSEN ET AL. Multimessenger observations of a flaring blazar coincident with high-energy neutrino icecube-170922a. *Science*, **361**(6398), July 2018. 27
- [58] MARK AARTSEN ET AL. Neutrino emission from the direction of the blazar txs 0506+056 prior to the icecube-170922a alert. *Science*, **361**(6398):147–151, July 2018. 27
- [59] R. ABBASI ET AL. Evidence for neutrino emission from the nearby active galaxy NGC 1068. *Science*, **378**(6619):538–543, 2022. 27, 117
- [60] J. AHRENS ET AL. IceCube Preliminary Design Document. 2008. 31
- [61] KURT WOSCHNAGG. The IceCube coordinate system. https://wiki.icecube.wisc.edu/index.php/Coordinate_system. 32
- [62] KURT WOSCHNAGG. Proposal for an IceCube Coordinate System. <http://docushare.icecube.wisc.edu/docushare/dsweb/Get/Document-8945/IceCubeCoordinateSystem.doc>. 32
- [63] J. MOUGINOT, E. RIGNOT, AND B. SCHEUCHL. Continent-wide, interferometric sar phase, mapping of antarctic ice velocity. *Geophysical Research Letters*, **46**(16):9710–9718, 2019. 32
- [64] R. ABBASI ET AL. The IceCube Data Acquisition System: Signal Capture, Digitization, and Time-stamping. *Nucl. Instrum. Meth. A*, **601**:294–316, 2009. 32, 38, 41
- [65] DAVID FREIHERR HEEREMAN VON ZUYDTWYCK. *HitSpooling: An Improvement for the Supernova Neutrino Detection System in IceCube*. PhD thesis, U. Brussels (main), 2015. 34
- [66] SASKIA PHILIPPEN, THORSTEN GLÜSENKAMP, AND SEBASTIAN SCHINDLER. Testing the Pointing of IceCube using the Moon Shadow in Cosmic-Ray Induced Muons. In *37th International Cosmic Ray Conference*, 8 2021. 35
- [67] M. G. AARTSEN ET AL. Measurements of the time-dependent cosmic-ray Sun shadow with seven years of IceCube data: Comparison with the Solar cycle and magnetic field models. *Phys. Rev. D*, **103**(4):042005, 2021. 35
- [68] MARTIN RONGEN. BFR anisotropy update. <https://drive.google.com/open?id=106wAXna7fcZykKI8d6Y0PRGdgnyhAv0g>. 37, 65
- [69] M. ACKERMANN ET AL. Optical properties of deep glacial ice at the south pole. *Journal of Geophysical Research: Atmospheres*, **111**(D13), 2006. 37, 38
- [70] R. ABBASI ET AL. Calibration and characterization of the icecube photomultiplier tube. *Nuclear Instruments and Methods in Physics Research Section A: Accelerators, Spectrometers, Detectors and Associated Equipment*, **618**(1-3):139–152, Jun 2010. 42
- [71] M. G. AARTSEN ET AL. Energy Reconstruction Methods in the IceCube Neutrino Telescope. *JINST*, **9**:P03009, 2014. 42
- [72] C. H. WIEBUSCH. Muon track reconstruction and data selection techniques in AMANDA. In *VLVnT Workshop on Technical Aspects of a Very Large Volume Neutrino Telescope in the Mediterranean Sea*, pages 129–133, 10 2003. 43, 44
- [73] M. G. AARTSEN ET AL. Improvement in Fast Particle Track Reconstruction with Robust Statistics. *Nucl. Instrum. Meth. A*, **736**:143–149, 2014. 43
- [74] PETER J. HUBER. Robust Estimation of a Location Parameter. *The Annals of Mathematical Statistics*, **35**(1):73 – 101, 1964. 43
- [75] MARTIN RONGEN. Private communication. 52

- [76] R. ABBASI ET AL. Constraints on Populations of Neutrino Sources from Searches in the Directions of IceCube Neutrino Alerts. *Astrophys. J.*, **951**(1):45, 2023. 53
- [77] Icecube wiki. https://wiki.icecube.wisc.edu/index.php/Stage_2_geometry. 2011. 55
- [78] CHRIS SHEREMATA AND DARREN GRANT. DeepCore DOM Profiles with the Trilateration Algorithm. https://docushare.icecube.wisc.edu/dsweb/Get/Document-63992/Presentation_CSheremata_trilateration.pptx. 2013. 54, 56
- [79] DMITRY CHIRKIN. Locating OM positions with muons. <https://user-web.icecube.wisc.edu/~dima/work/BKP/DCS/WUPPERTAL04/mucal/mucal.ppt>. 54
- [80] DMITRY CHIRKIN. Private communication. 55
- [81] S. S. WILKS. The Large-Sample Distribution of the Likelihood Ratio for Testing Composite Hypotheses. *The Annals of Mathematical Statistics*, **9**(1):60 – 62, 1938. 57
- [82] B. EFRON. Bootstrap Methods: Another Look at the Jackknife. *The Annals of Statistics*, **7**(1):1 – 26, 1979. 58
- [83] D. HECK, J. KNAPP, J. N. CAPDEVIELLE, G. SCHATZ, AND T. THOUW. CORSIKA: A Monte Carlo code to simulate extensive air showers. 2 1998. 65
- [84] DMITRY CHIRKIN. Likelihood description for comparing data with simulation of limited statistics, 2013. 85
- [85] MARTIN RONGEN. Private conversation, 2022-2023. IceCube Slack, September. 87, 89, 90, 91, 92
- [86] R. ABBASI ET AL. In-situ estimation of ice crystal properties at the south pole using led calibration data from the icecube neutrino observatory. *The Cryosphere Discussions*, **2022**:1–48, 2022. 97, 98, 101
- [87] VICTOR F. PETRENKO AND ROBERT W. WHITWORTH. Optical and electronic properties. In *Physics of Ice*, chapter 9. Oxford University Press, 01 2002. 97
- [88] DMITRY CHIRKIN. Evidence of optical anisotropy of the South Pole ice. In *33rd International Cosmic Ray Conference*, page 0580, 2013. 98
- [89] D. E. VOIGT. c-axis fabric of the south pole ice core, spc14. Technical report, U.S. Antarctic Program (USAP) Data Center, 2017. <https://doi.org/10.15784/601057>. 98, 99, 100
- [90] DANIEL H.M. RICHARDS, SAMUEL S. PEGLER, SANDRA PIAZOLO, AND OLIVER G. HARLEN. The evolution of ice fabrics: A continuum modelling approach validated against laboratory experiments. *Earth and Planetary Science Letters*, **556**:116718, 2021. 98
- [91] MCCONNEL JAMES C. On the plasticity of an ice crystal. *Proc. R. Soc. Lond.*, 1891. 98
- [92] SÉRGIO H. FARIA, ILKA WEIKUSAT, AND NOBUHIKO AZUMA. The microstructure of polar ice. part ii: State of the art. *Journal of Structural Geology*, **61**:21–49, 2014. Microdynamics of Ice. 98
- [93] N. H. WOODCOCK. Specification of fabric shapes using an eigenvalue method. *Geological Society of America Bulletin*, **88**(9):1231, January 1977. 98, 100
- [94] JUAN CAO AND JIANMIN ZHENG. Bivariate splines over triangular meshes for freeform surface modeling with sharp features. *Computer-Aided Design and Applications*, **14**:1–9, 11 2016. 105
- [95] K. M. GORSKI, E. HIVON, A. J. BANDAY, B. D. WANDELT, F. K. HANSEN, M. REINECKE, AND M. BARTELMANN. Healpix: A framework for high-resolution discretization and fast analysis of data distributed on the sphere. *The Astrophysical Journal*, **622**(2):759–771, April 2005. 111

- [96] RICHARD NAAB, ERIK GANSTER, AND ZELONG ZHANG. Measurement of the astrophysical diffuse neutrino flux in a combined fit of IceCube's high energy neutrino data. In *38th International Cosmic Ray Conference*, 7 2023. 117
- [97] MIRCO HUENNEFELD ET AL. Combining Maximum-Likelihood with Deep Learning for Event Reconstruction in IceCube. *PoS*, **ICRC2021**:1065, 2021. 118

The IceCube Neutrino Observatory at the South Pole began full operation in 2011. It consists of 5160 digital optical modules (DOMs) installed up to 2.4 km deep in the glacial ice. IceCube discovered the high-energy astrophysical neutrino flux in 2013, and since then has found evidence for several extragalactic neutrino sources as well as neutrino emission from the galactic plane of the Milky Way.

This PhD thesis contributes to improving neutrino source searches by improving on fundamental aspects of calibration and event reconstruction in IceCube. Firstly, it presents an in-situ geometry calibration of detector module positions that is precise enough to measure < 1 m displacements from the assumed nominal positions. Secondly, it presents an advanced implementation of "spline tables" for modelling photon propagation in the ice, which incorporates the latest understanding of the birefringent optical properties of the glacial ice. Both of these are expected to improve the reconstruction of muon tracks, which are the main event class used for neutrino source searches in the northern sky.



Matti Jansson
was born in Österbybruk, Sweden.
He studied engineering physics with
a specialization in quantum
mechanics and mathematics at
Umeå University. Between 2019 and
2024 Matti pursued a PhD at
Stockholm University with the
IceCube Collaboration.



ISBN 978-91-8014-673-9

Department of Physics

